A Study of the Sensitivity of the H Dibaryon Search Experiment E813 at BNL through $(\Sigma^-, p)_{atom} \rightarrow \Lambda + n$

By

Liping Gan

A THESIS

SUBMITTED TO THE FACULTY OF GRADUATE STUDIES IN PARTIAL

FULFILLMENT OF THE REQUIREMENTS

FOR THE DEGREE OF

DOCTOR OF PHILOSOPHY

IN

PARTICLE/NUCLEAR PHYSICS

DEPARTMENT OF PHYSICS

THE UNIVERSITY OF MANITOBA

WINNIPEG, MANITOBA

CANADA

April 7, 1998

THE UNIVERSITY OF MANITOBA

FACULTY OF GRADUATE STUDIES

*****

COPYRIGHT PERMISSION PAGE

A Study of the Sensitivity of the H Dibaryon Search Experiment E813 at BNL through $(\Sigma^-, p)_{atom} \rightarrow \Lambda + n$

By

Liping Gan

A Thesis/Practicum submitted to the Faculty of Graduate Studies of The University of Manitoba in partial fulfillment of the requirements of the degree of

DOCTOR OF PHILOSOPHY

Abstract

This thesis is a study of the sensitivity of BNL experiment E813. Experiment E813 was a search for the H-Dibaryon (a six-quark $uuddss$ state) at Brookhaven National Laboratory's 2–GeV/c beam line. It was insensitive to H decay modes and lifetime, and looked directly for H formation through a three step reaction mechanism. A liquid hydrogen target was used to produce Ξ^- hyperons via the reaction $K^- + p \rightarrow K^+ + \Xi^-$. These Ξ^-'s were then slowed down in tungsten degraders so that a small fraction of them would stop in a liquid deuterium target located above the liquid hydrogen target to form a $(\Xi^-, d)_{atom}$. The signature for H formation via $(\Xi^-, d)_{atom} \rightarrow H + n$ would be a monoenergetic neutron in coincidence with the formation of a $(\Xi^-, d)_{atom}$. The most critical property of the experimental apparatus is the product of the hyperon stopping efficiency and the neutron detection efficiency, which is needed to quantitatively estimate the upper limit on the H formation branching ratio and to interpret the experimental results for the H particle search. This combined efficiency was calibrated with a similar three step reaction mechanism through a study of Σ^- capture on hydrogen followed by $(\Sigma^-, p)_{atom} \rightarrow \Lambda + n$. The details of the calibration are discussed in this thesis.

Acknowledgements

I would like to express my deepest felt thanks to my parents. Without their endless love, unconditional support and encouragement, it would have been impossible for me to pursue my doctoral degree.

I thank my thesis advisor, Dr. Charles Davis, for his guidance, patience and tireless commitment.

I would like to give my special thanks to Prof. W.T.H. van Oers and Prof. Shelley Page. They have given me so many valuable comments and suggestions during my thesis writing, and made every effort to set up my oral examination on time.

I sincerely thank Dr. Alain Berdoz. He spent many hours with me trying to understand the hyperon stopping efficiency by using Monte Carlo simulation. His experience and knowledge has benefited me greatly.

Thanks to Prof. Gregg Franklin and Prof. Bernd Bassaleck. Their knowledge and deep understanding about a lot of details of this experiment always amazed me. They have been the persons I went to first whenever I encountered problems during my analysis.

Thanks to Phil Koran for his cooperation during the data collection and analysis. His humor made the time at BNL enjoyable. I have learned a lot through our many discussions.

I am very grateful to Dr. Adam Rusek. I have always remembered all the

PAW lessons he gave me.

Thanks to Dr. Markus Burger and Dr. Frank Merrill. They have shared their experience with me on running the experiment and the data analysis. Dr. Burger was so kind to let me use some of his plots in my thesis.

Thanks to the other members in the Manitoba group, Dr. Des Ramsay, Dr. Larry Lee and Mike Landry. They gave me many good suggestions at Manitoba H particle meetings. Mike did such a good job managing "Carl" that my data analysis was carried out smoothly.

I also thank each individual on the H particle collaboration. Prof. Brian Quinn, Dr. Bob Chrien, Dr. Reyad Sawafta, Dr. David Gill, Prof. Reinhard Schumacher, Dr. Reinhard Stotzer, and many others. It is everyone's commitment and efforts that made this experiment a success.

Contents

List of Figures

List of Tables

Chapter 1

Introduction

The sensitivity of experiment E813 at Brookhaven National Laboratory (BNL) plays an extremely important role in interpreting the experimental results for the H particle (a six quark system) search. This thesis is a study of the sensitivity of this experiment through Σ^- capture on hydrogen. In the first chapter, the motivation for the H particle search is described, and the E813 experiment and how to calibrate its sensitivity through the $(\Sigma^-, p)_{atom} \rightarrow \Lambda + n$ reaction are discussed.

1.1 Physics Motivations

1.1.1 The QCD Prediction of Exotic Hadron Configurations

Discovering and understanding the fundamental interactions in the universe is a principal task for physicists. Four interactions in nature have been discovered: the strong, weak, electromagnetic and gravitational interactions. The strong interaction is the dominant force acting between nucleons, and both electromagnetic and weak interactions also play an important role in determining the properties of nuclei. It is widely believed that the Glashow-Salam-Weinberg theory successfully

describes the electroweak interaction; however, the strong interaction remained an awkward problem until the late sixties. The big breakthrough was the foundation of the quark model after Bjorken discovered the scaling property of structure functions [1] in lepton-nucleon deep inelastic scattering in 1969. The essential concepts of the quark model are: that the hadrons are made of quarks (e.g., the baryons are three quark states and the mesons are quark-antiquark states), and that quarks interact with each other through the exchange of gluons. Since then, a new nonabelian [2] gauge field theory, which describes the strong interaction, has been established. It is quantum chromodynamics (QCD).

In 1951 Fermi discovered the $\Delta^{++} = uuu$ baryon. Its spin is $\frac{3}{2}$, obtained by combining three identical $J = \frac{1}{2}$ u quarks in their ground state. Because $J = \frac{3}{2}$ is a symmetric spin state and the ground state is a symmetric space state, this configuration corresponded to three identical fermions (u quarks) in a completely symmetric ground state, which is not allowed by the Pauli exclusion principle. This problem was solved by introducing a new quantum number, called "color". If each u quark carries a different color, then the Δ^{++} is in an antisymmetric color state, so that the Pauli exclusion principle is maintained.

QCD is the $SU(3)$ nonabelian gauge theory of color charge. The fermions which carry color charge are the quarks. The color charge of a quark has three possible values (red, blue, and green). Antiquarks carry anticolor. The gauge bosons mediating the quark–quark interaction, which are massless and also carry color (color-anticolor state), are the gluons. The color charge of a gluon has eight possible values. The interquark interactions are invariant under color interchange.

---

[1] Bjorken scaling hypothesis: If the structure functions in lepton-nucleon deep inelastic scattering do not depend on the 4-momentum transfer squared, Q^2, but are pure functions of a dimensionless variable, $x = \frac{Q^2}{2M\nu}$, where M is the mass of nucleon and ν is the energy transfer, then the lepton is scattered on a pointlike particle.

[2] Nonabelian group: A nonabelian group is a group whose elements do not necessarily commute with each other. For example, if A and B are the elements of a nonabelian group, then $[A, B] = 0$ is not always true.

described by the symmetry group $SU(3)$.

There are many reasons to hope and expect that QCD is a precise and complete theory of quarks and gluons. QCD purports to be the ultimate theory explaining all strong interaction effects at all energies. For example, QCD predicts quark confinement, i.e., the quarks should be permanently "confined" inside their bound states. This gives an explanation as to why no single quark has ever been found. In addition, like quantum electrodynamics (QED), QCD has local gauge symmetry. However, the mathematical complexity of QCD has prevented quantitatively testing its correctness. The most outstanding property of the strong interaction is its asymptotic freedom. This can be seen from the evolution of the effective coupling constant of QCD. The leading order behavior of the coupling constant in QCD [1] is

$$\alpha_c(Q^2) \equiv \alpha_{eff}(Q^2) = \frac{1}{B \ln(Q^2/\Lambda^2)} \tag{1.1}$$

where

$$\Lambda^2 = Q_0^2 \exp(\frac{1}{B\alpha_c(Q_0^2)}). \tag{1.2}$$

and

$$B = (33 - 2n_f)/12\pi. \tag{1.3}$$

Here, Q^2 is the 4-momentum transfer squared, n_f is the number of quark flavors, and Q_0^2 is the renormalization point. As seen from eq. (1.1), when $n_f \leq 16$, the QCD coupling constant approaches zero as $Q^2 \to \infty$; however, α_{eff} can not be ignored when Q^2 is small. Fig. 1.1 shows the different behaviors of the QCD and QED coupling constants. Therefore, for QCD, traditional perturbation theory should work well at high Q^2 (short distances) but break down at small Q^2 (large distances) where α_{eff} becomes large and presumably confines quarks within hadrons. In fact, only the short-distance phenomena and predictions of

QCD theory have been tested in a variety of experiments. On the other hand, unfortunately, too little about the low energy, large distance, and non-perturbative region of QCD has been understood. Despite many years of effort, direct attempts to verify QCD have had very limited success.

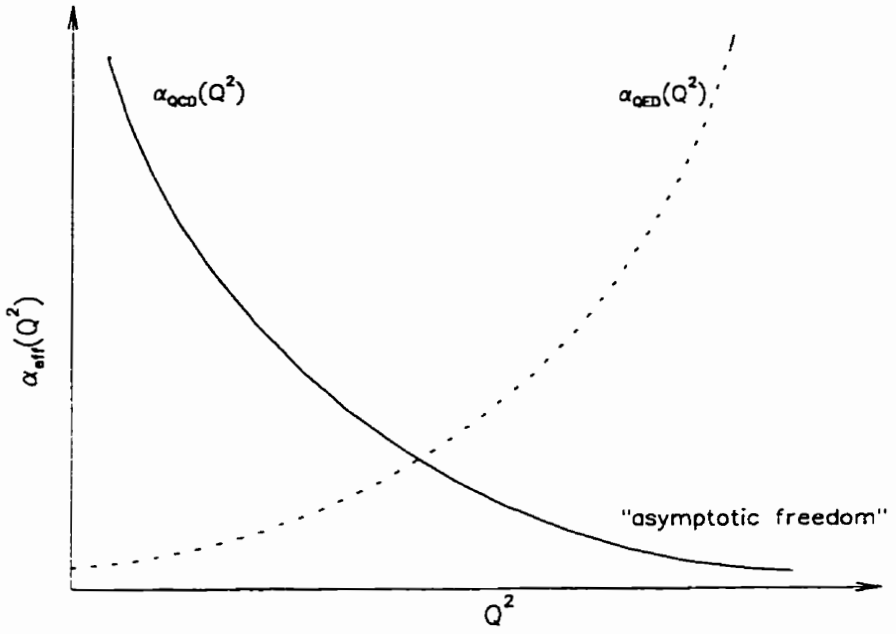

Figure 1.1: Comparison between the QCD and QED coupling constants. The solid curve represents the leading order of the coupling constant of QCD versus 4-momentum transfer squared Q^2, and the dashed curve represents the leading order of the coupling constant of QED versus Q^2.

As a consequence, one has to seek an alternative way to understand the non-perturbative (low energy and large distance) behavior of QCD. One way is to build phenomenological models which combine the basic ingredients of QCD with input from experiment. In the past three decades, a number of models have been suggested. They can be mainly divided into three categories: bag models where quarks are considered as free relativistic particles moving in a bag with appropriate boundary conditions; Skyrmion models where the relevant degrees of freedom are

those of mesons and for which the baryon notion is recovered as a topological concept; and nonrelativistic potential models where the quark motion must satisfy a Schrödinger equation based on a quark-quark potential. Each of these approaches has attractive features but suffers from a number of drawbacks. They agree more or less on the mass spectrum of simple systems, such as regular hadrons (qqq) and mesons ($q\overline{q}$), but sometimes present drastic differences on other observables. It is thus particularly interesting to compare these models with experiments.

According to QCD, the observable systems can only be in color-singlet states. Therefore any observable system is of the form $q^m\overline{q}^n$ with $m - n = 3B$, where B is the baryon number, as the quark has three possible colors. This indicates that exotic hadron configurations, which are combinations other than the usual qqq and $q\overline{q}$, are allowed by QCD as long as they are color-singlet states. As examples, there are possible $q^2\overline{q}^2$ "baryonium" configurations [2][3], the "Z^* resonance" [4] $q^4\overline{q}$ system of strangeness $s = +1$, and q^6 dibaryons. The existence of these exotic hadron configurations, especially the q^6 dibaryons, has been an open question for more than two decades. It has drawn extensive attention from both theoretical and experimental physicists, because this may provide a new approach to test QCD.

1.1.2 The *H* Particle

Among the 6 quark states, the $s = -2$ sector plays a special role. If one ignores the differences in the quark masses between strange and nonstrange quarks, the one-gluon-exchange interaction, called the color-magnetic interaction, between quarks has the form [5]:

$$V_{CM} = \frac{\alpha_c}{m^2}[N(N-10) + \frac{4}{3}S(S+1) + 2C_C^2 + 4C_F^2] \tag{1.4}$$

where α_c is the coupling constant of QCD and m is the mass of the quarks. N is the number of quarks in the system, and S is the total spin of the system. C_C^2

and C_F^2 are the eigenvalues of the quadratic Casimir operator [3] for the $SU(3)_C$ and $SU(3)_F$ groups. As seen from eq. (1.4), for a 6 quark state ($N = 6$), which has $C_C = 0$ (color singlet), $C_F = 0$ (flavor singlet), and $S = 0$ (spin singlet), its color-magnetic interaction has the minimum value, $V_{CM} = -\frac{24\alpha_s}{m^2}$. The 6-quark system consisting of two u quarks, two d quarks and two s quarks can exist in such a flavor, color, and spin singlet state, which takes maximum advantage of the color-magnetic attraction.

In 1977, Jaffe [6] first suggested, based on the MIT bag model, that the $uuddss$ state with spin-parity 0^+ and isospin 0, which he called the H particle, would be a stable state against strong decay. His calculation indicated that the mass of the H is $m_H = 2150$ MeV, some 80 MeV below the 2Λ threshold. Unlike the deuteron, which is a weakly bound "quasimolecule" in which two separated three-quark bags retain much of their identity, the H was predicted to be a real single particle with all six quarks within one bag. Since then, many other calculations using different models have been devoted to this subject.

Aerts et al. studied the 6-quark spectrum for all possible configurations with the MIT bag model [7]. They found that only the $uuddss$ configuration might be a candidate for a stable dibaryon. This can be simply understood as follows: Because quarks are fermions they must obey the Pauli exclusion principle, that two or more identical fermions may not exist in the same quantum state. The 6-quark state with $uuddss$ configuration, which has an equal number of all possible flavors (below the c quark threshold) with 2 quarks in each flavor, may occupy the lowest energy level in the 6-quark spectrum. Any other configuration, having more than 2 quarks of the same flavor, will occupy a higher energy level. If the mass of such a 6-quark ($uuddss$) system is below the threshold of twice the Λ mass, it would be stable against strong decay in all the baryon-baryon channels.

[3] Casimir operator: the Casimir operators of a group are those operators that commute with all generators of the group.

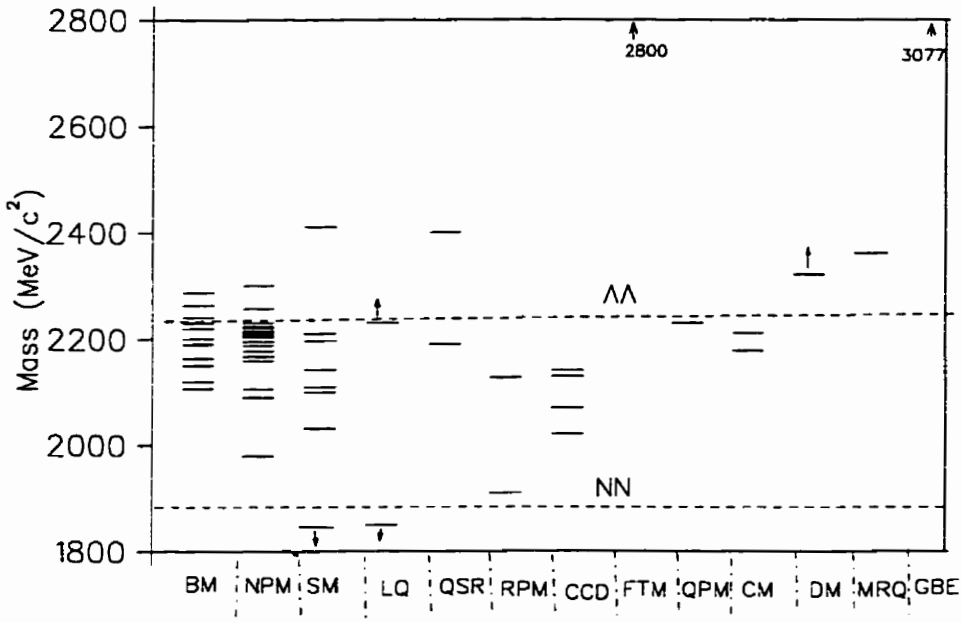

Figure 1.2: Mass of the H particle calculated by various models. Each column represents a model, and each line per column represents a different calculation of m_H within that model. BM is the bag model; NPM is the non-relativistic potential model; SM is the Skyrme model; LQ is the lattice QCD; QSR is the QCD sum rule; RPM is the relativistic potential model [46]-[47]; CCD is the chiral colour dielectric model [48]-[50]; FTM is the flux tube model [51]-[52]; QPM is a quark pairing mechanism [53]; CM is the chromomagnetic model [54]-[55]; DM is the diquark model [56]; MRQ is the multi-configuration relativistic quark model [57]; GBE is the Goldstone boson exchange model [58]. The dashed lines show the $\Lambda\Lambda$ and neutron-neutron masses.

The current theoretical situation regarding the H particle remains unclear; the predictions of the H mass are model dependent. A variety of calculations for the H mass by different models are presented in Fig 1.2; the details of each model are not discussed in this thesis. As seen from Fig 1.2, most of the calculations were performed with bag models [7]-[16], Skyrme models [17]-[29], non-relativistic models [5] [30]-[41], lattice QCD [42]-[43] and QCD Sum Rules [44]-[45]. Some results confirm Jaffe's prediction that the H is stable against strong decay, while others give contradictory conclusions. A recent result calculated in the framework of the Goldstone boson exchange interaction by Glozman et al. [58] showed that the mass of the H was 847 MeV above the $\Lambda\Lambda$ threshold, which indicated that a deeply bound H particle should not exist. A month later, however, Ghosh and Phatak pointed out that the mass of the H was smaller than the $\Lambda\Lambda$ threshold by more than 100 MeV [50], according to their calculations based on a chiral colour dielectric model. Independent of the calculation details, however, most calculations of the H mass fall in the range from 2100 MeV/c^2 to 2300 MeV/c^2. This corresponds with a range of H binding energy from 130 MeV bound to 70 MeV unbound with respect to the mass of two Λ's.

Since the H decay channels and phase space available for the decays depend on the mass of the H, the uncertainty in m_H also results in a wide range for the lifetime of the H to be considered. The lifetime of the H, τ_H, is around $\sim 10^{-10}$s if m_H is near the mass of 2Λ, while τ_H would be $> 10^7$s if m_H is near the $N\Lambda$ threshold [59]. As a result, the experimental observation of the H particle would be a very crucial test for QCD or at least for models derived from QCD. In addition, quark matter calculations indicate that a stable state of condensed matter may not be ordinary nuclear matter but "strange matter" [60][61] whose number of strange quarks approximately equals its baryon number. Such matter may be found in a neutron star. The H particle might be simply the lightest of a family of $-s = B$ ($B \geq 2$) particles. Furthermore, compared to a star containing just nucleons and leptons, the presence of strange matter in a neutron star would

qualitatively change the way in which the structure of the star depends upon neutrino trapping [62], and this could lead to the delayed formation of a black hole. Therefore, H research also plays an important role in astrophysics. In summary, the study of the H particle can greatly deepen the fundamental understanding about the strong interaction, and further expand our knowledge of nature.

1.2 Experimental H Particle Research

In the late 1960's and the early 1970's, there were several experiments [63]-[67] done with the intention of searching for double strangeness hypernuclei and new resonances in reactions and mass ranges which turn out to be relevant to the H particle search. Since Jaffe first predicted [6] the H particle in 1977, many experimental efforts have been devoted to this field. The reviews of previous experiments can be found in ref. [68][69]. Nonetheless, no measurement performed to date has had enough sensitivity to either prove or disprove the existence of the H particle. It should be noted that most of the previous experiments searched for the subsequent decay of the H [70]-[84]. Their sensitivities depended on the H decay modes and lifetime, which are currently unknown because of the uncertainty in the H mass.

The first direct attempt was made at Brookhaven National Laboratory (BNL) by Caroll et al. [85] who searched for the H in the missing mass spectrum of the reaction $p + p \rightarrow K^- + K^- + X$. No evidence for the H was found but an upper limit on the H production cross section of about 40 nb was suggested. A later theoretical calculation [86], however, gave a production cross section of 0.2–2.0 nb which was more than 20 times lower than Carrol's estimation. Later on, Kawai et al. [87] at KEK (experiment E248) used a new version of the experimental arrangement to rerun the BNL experiment with improved sensitivity. There have been no results released yet in the scientific literature for E248.

Ejiri et al. [88] searched for the H through double weak decay of two nucleons in nuclei:

$$p + p \rightarrow H + 2e^- + 2\nu, \qquad p + n \rightarrow H + e^- + \nu, \qquad n + n \rightarrow H.$$

This resulted in a lower limit on the H mass of $m_H \geq 1875.1$ MeV/c^2.

A series of experiments have been carried out at the D6 beam line of the Alternating Gradient Synchrotron (AGS) at Brookhaven National Laboratory. Experiment E886 [89]-[90] searched for H dibaryon-nucleus bound states (H-^3He and H-d) in relativistic Au+Pt heavy ion collisions; a null result was given for lifetimes of the H-nucleus system being less than $\sim$ 20 ns. Experiment E836 [91] was a search for a moderate or deeply bound H through $K^- + {}^3He \rightarrow H + K^+ + n$. No H was found in the mass range from 1.85 GeV/c^2 to 2.18 GeV/c^2. Upper limits on the H production cross section were given in the range of 0.058 to 0.021 μb/sr. The E813 experiment was a search for a weakly bound H through the $(\Xi^-, d)_{atom} \rightarrow H + n$ reaction. The details of E813 will be discussed in this thesis. The E885 experiment [93] was to detect the H in $K^- + {}^{12}C \rightarrow K^+ + H + X$ or to detect $\Lambda\Lambda$ hypernuclei in $K^- + {}^{12}C \rightarrow {}^{12}_{\Lambda\Lambda}Be + K^+$; data analysis is currently in progress.

There were several experiments [95]-[98] conducted at KEK, to directly search for the deeply bound H via the (K^-, K^+) reaction on nuclei in emulsions:

$$K^- + (pp) \rightarrow H + K^+.$$

where (pp) is a proton pair in a nucleus. They found no H signal in the H mass range from 1900 to 2160 MeV.

More work, with higher sensitivity, on the direct search for the H particle is strongly needed. A number of H production reactions have been proposed in the literature [99] such as:

(a) $p + p \rightarrow H + K^- + K^+$.

(b) $\Lambda + p \rightarrow H + K^+$.

(c) $\Sigma^- + p \rightarrow H + K^0$.

(d) $\Xi^- + p \rightarrow H + \gamma, H + \pi^0$.

(e) $\Xi^- + d \rightarrow H + n$.

(f) $\Xi^- + {}^4He \rightarrow H + t$.

(g) $K^- + d \rightarrow H + K^0$.

(h) $K^- + {}^3He \rightarrow H + K^+ + n$.

Among the above reactions, Aerts and Dover pointed out that reaction (e) would present the most favorable case [100] for a weakly bound H, whereas reaction (h) would be favored for a deeply bound H particle [101].

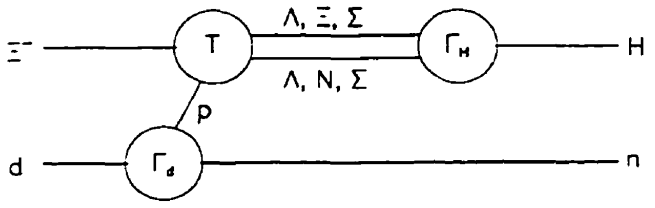

Figure 1.3: Schematic drawing of H production mechanism used by Aerts and Dover to calculate the rate for the $\Xi^- + p \rightarrow H + n$ reaction. The Γ and T vertices are explained in the text.

Aerts and Dover further calculated [100] the branching ratio, R, of H production in the process $\Xi^- + d \rightarrow H + n$. The branching ratio R was defined by

$$R = \Gamma_{(\Xi^- - d \rightarrow H - n)} / \Gamma_{(\Xi^- - d \rightarrow anything)}. \tag{1.5}$$

The mechanism used in their calculation is shown in Fig 1.3, where $\Lambda\Lambda$, ΞN, and $\Sigma\Sigma$ are the the baryon-baryon virtual intermediate states. Aerts and Dover described those intermediate states by plane waves. The vertex $\Gamma(\vec{k_1}, \vec{k_2})$ with momenta $\vec{k_1}$ and $\vec{k_2}$ was obtained from the overlap of quark wave functions, where oscillator wave functions were used. For the transition matrix T in the baryon-baryon interaction $\Xi^- + p \rightarrow B_1 + B_2$, they roughly estimated it by replacing T with one-meson-exchange static potentials, obtained from the work of Nagels, Rijken, and de Swart [102]. When the $(\Xi^- d)_{atom}$ is in an S state, Aerts and Dover's final result for the branching ratio R is:

$$R = \Gamma_0^2 [\frac{6\pi\xi}{R_H^2}]^{3/2} [\frac{Q + E_B}{Q}]^{1/2} |\phi_d(k_0)|^2 \tag{1.6}$$

where

$$\xi = 2m_n m_H / m_\Lambda (m_n + m_H)$$
$$Q = m_\Xi + m_p - 2m_\Lambda \approx 28.5 MeV$$
$$E_B = 2m_\Lambda - m_H$$
$$k_0 = [2m_n m_H (Q + E_H)/(m_n + m_H)]^{1/2}$$

and Γ_0 is the color-spin-flavor recoupling coefficient. R_H is the oscillator radius for the H particle. $\phi_d(k)$ is a Hulthén wave function for the deuteron:

$$\phi_d(k) = C[1/(\beta^2 + k^2) - 1/(\gamma^2 + k^2)] \tag{1.7}$$

with $\beta^2 = 2.096 \times 10^{-3}$ GeV^2 and $\gamma^2 = 0.10269$ GeV^2.

The branching ratio R is a function of the H particle mass. This is shown in Fig 1.4, where the curves labeled D and F refer to the use of models D or F of Nagels [102] to describe the two baryon interaction potentials. The reason for model D and model F is the ambiguity in the sign of the scalar-meson-nonet coupling, which can not be determined by nucleon-nucleon scattering analysis. Model D gives a better explanation of hyperon-nucleon scattering experiment data than model F, while model F gives better values of coupling constants and a better fit to the nucleon-nucleon scattering measurements. Model F, however, is excluded by a latter calculation [103]. As seen from the curve labeled D in Fig. 1.4, for the $(\Xi^-, d)_{atom} \rightarrow H + n$ channel, the branching ratio R swiftly decreases with decreasing m_H. It is close to 100% if m_H is around 2300 MeV, while it drops down to 10% if m_H is near 2130 MeV. Since the value of R is expected to be reasonably large, this process provides an excellent means to search for the H in the weakly bound mass range with respect to the 2Λ threshold.

An experimental search for the H particle within the weakly bound range is more interesting because most theoretical calculations indicate that the H mass is within this region. An H particle in this kinematical region would be stable against strong decay. In this case, kinematic reconstructions could be used to obtain the H mass, and the width of which should be quite narrow due to its long lifetime. Exploiting these features of the kinematics, the E813 experiment was conducted at the BNL D6 beam line. It was designed to search for the H through the reaction $(\Xi^-, d)_{atom} \rightarrow H + n$, which has maximum sensitivity in the mass region near the mass of two Λ hyperons. This experiment combined with another experiment E836 [91], searching for a moderate or deeply bound H through the reaction $K^- + {}^3He \rightarrow H + K^- + n$, were expected to cover the entire mass region of interest below the 2Λ mass.

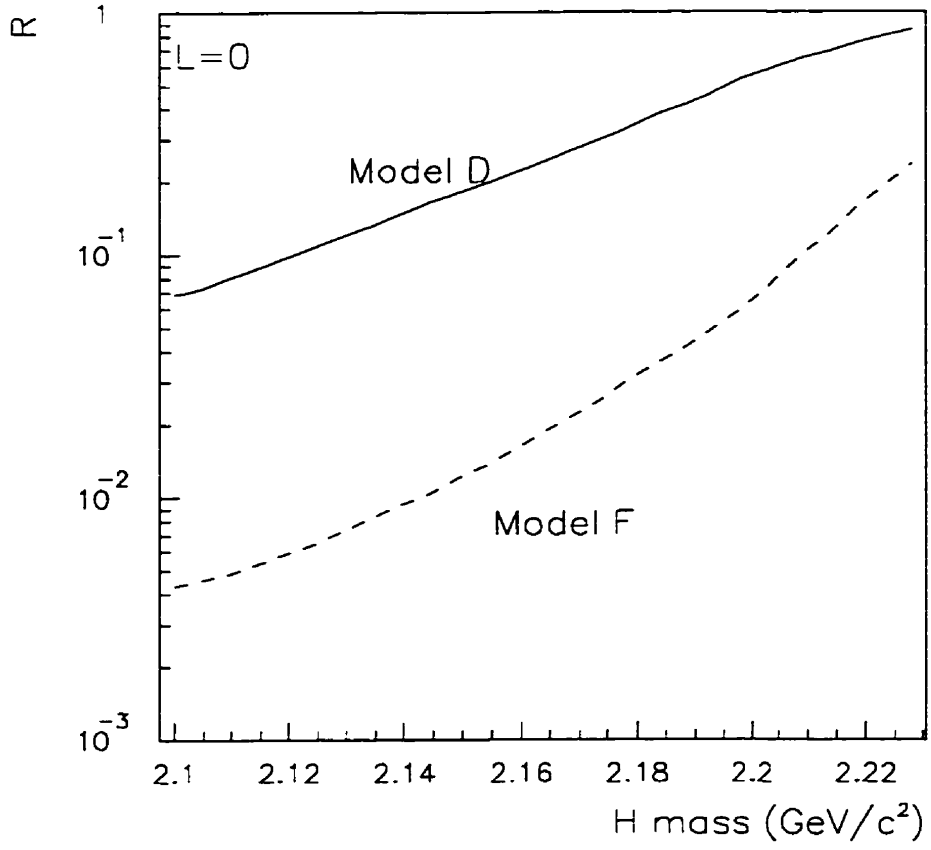

Figure 1.4: Branching ratio R as a function of the mass of H (m_H) for capture of the Ξ from an S atomic orbital. The curves labeled D and F refer to the use of models D or F of Nagels [102] to describe the baryon-baryon interaction potentials.

1.3 Experiment E813 at BNL

1.3.1 The *H* Particle Search

Experiment E813 was carried out at the 2-GeV/c beam line of the Alternating Gradient Synchrotron at Brookhaven National Laboratory, searching for the H particle by using a three step reaction mechanism. As Fig 1.5 shows, a 1.8 GeV/c K^- beam was delivered to a liquid hydrogen target to produce Ξ^-'s through the double strangeness exchange reaction $K^- + p \rightarrow K^+ + \Xi^-$. The Ξ^-'s were then slowed down in tungsten degraders so that a fraction of them would stop in a liquid deuterium target located above the liquid hydrogen target to form $(\Xi^-, d)_{atom}$'s. If the H exists, calculations [104] indicate that some of the $(\Xi^-, d)_{atom}$'s could then collapse into H particles through the reaction $(\Xi^-, d)_{atom} \rightarrow H + n$. The Ξ^-'s, which were slow enough to stop in deuterium, would deposit about 1.0 MeV–2.2 MeV energy in silicon detectors installed behind the tungsten to form a tag. The signature for H formation via $(\Xi^-, d)_{atom} \rightarrow H + n$ would be a monoenergetic neutron in coincidence with a tagged Ξ^-. Two arrays of scintillator logs on both the left and right side of the target, with another scintillating detector (IT) in front of the hydrogen target, measured the time-of-flight (TOF) of the neutron. Monoenergetic neutrons from $(\Xi^-, d)_{atom} \rightarrow H + n$ would appear as a clear peak in the neutron time-of-flight spectrum. With two-body kinematics, the energy of the neutrons in the peak could be used to calculate the mass of the H, and the yield would indicate the H formation branching ratio.

According to Aerts and Dover's estimation [104], the branching ratio, R, for H formation through the reaction $(\Xi^-, d)_{atom} \rightarrow H + n$ is a function of H particle binding energy, and it swiftly decreases with increasing binding energy. As Fig 1.4 shows, the value of R decreases to 0.1 as the binding energy increases to 100 MeV. On the other hand, as the mass of the $(\Xi^-, d)_{atom}$ is 30 MeV above the 2Λ mass, the H can not be produced through this process if its mass is above the

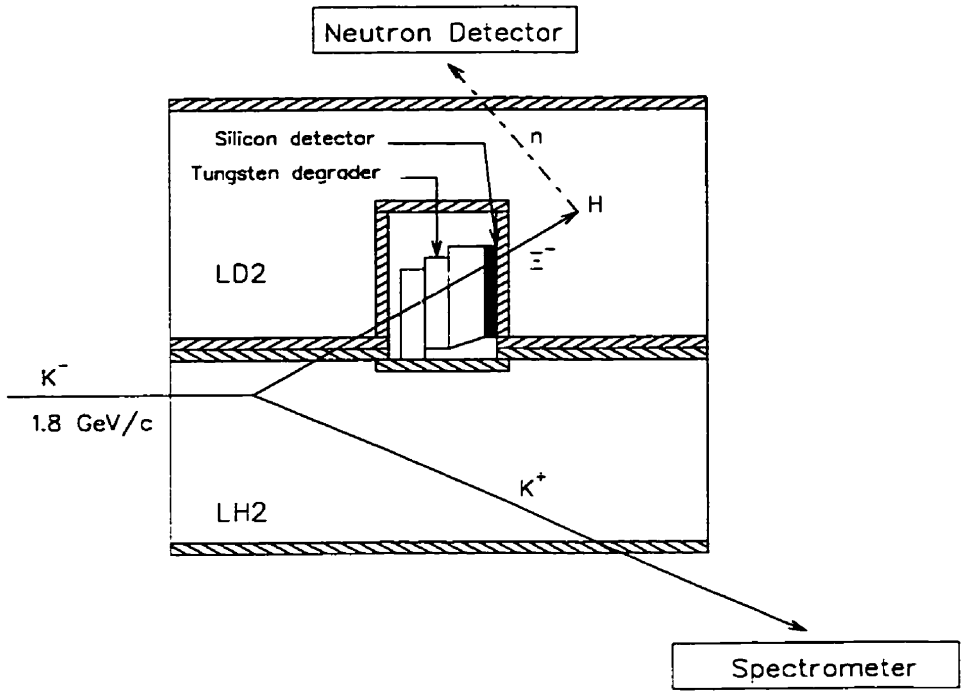

Figure 1.5: Schematic plot of the reaction mechanism and target arrangement for the H particle search in experiment E813.

2Λ mass by more than 30 MeV. In fact, if it is unbound by more than 15 MeV, the energy of the spectator neutron will be too low to be easily detected above the background. As a result, this experiment is expected to be sensitive over the binding energy region $-15 < B_H < 100$ MeV [105]. This region is considered to be the most promising H mass region; it covers most of the H particle mass predictions.

1.3.2 The (π^-, K^+) Calibration

As discussed above, the signature for H formation in E813 is a monoenergetic neutron in coincidence with the formation of a $(\Xi^-, d)_{atom}$. As a result, the most important issues for the experimental sensitivity are the tag efficiency of Ξ^- stopping and the neutron detection efficiency. The experimental technique and measurement ability have to be proved in order to properly interpret the H particle search result. One of the main tasks of this experiment is to estimate the H formation branching ratio. The number of monoenergetic neutrons observed in E813 is given by:

$$N_n = N_{tag} \cdot \varepsilon_{stop} \cdot \nu \cdot R \cdot \eta_{ND} \tag{1.8}$$

where:

N_n is the number of monoenergetic neutrons;

N_{tag} is the number of tagged Ξ^-'s;

ε_{stop} is the Ξ^- stopping efficiency;

ν is the efficiency for stopped Ξ^-'s to form $(\Xi^-, d)_{atom}$'s;

R is the branching ratio for the $(\Xi^-, d)_{atom} \rightarrow H + n$ reaction;

η_{ND} is the neutron detection efficiency.

Therefore, the branching ratio is experimentally determined as:

$$R = \frac{N_n}{N_{tag} \cdot \varepsilon_{stop} \cdot \nu \cdot \eta_{ND}} \tag{1.9}$$

As seen from above eq. (1.9), one must know the combined Ξ^- stopping efficiency and the neutron detection efficiency, $\varepsilon_{stop} \cdot \eta_{ND}$, in order to calculate the H formation branching ratio R. As a result, the calibration of this combined efficiency is very crucial for experiment E813.

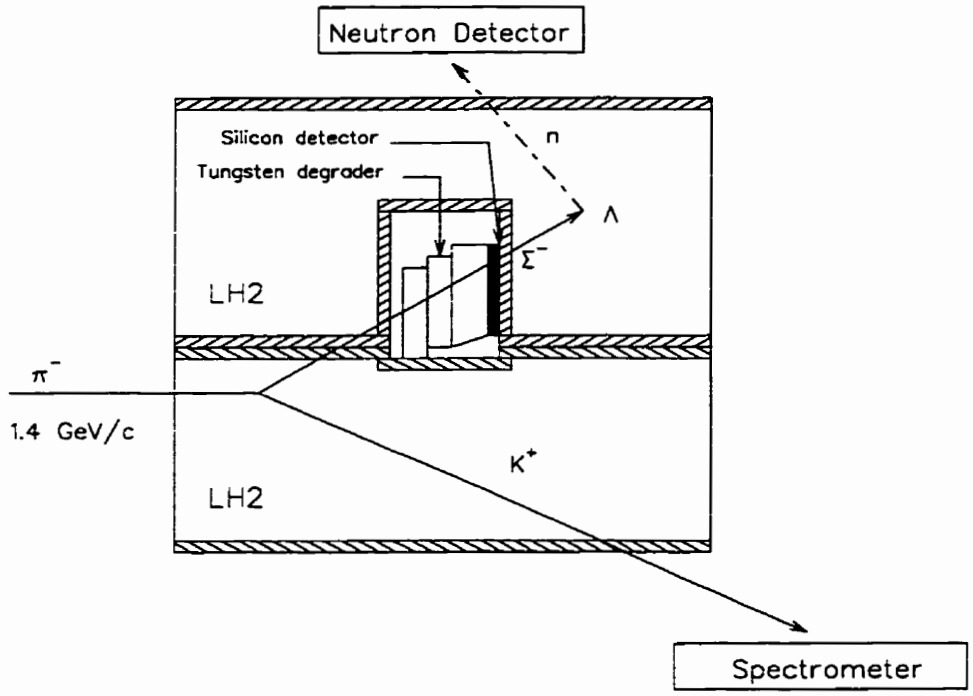

Figure 1.6: Schematic plot of the reaction mechanism for the (π^-, K^+) calibration run.

The (π^-, K^+) calibration experiment used a similar three step reaction mechanism through Σ^- capture on hydrogen. Table 1.1 shows the comparison between the H production and the (π^-, K^+) calibration experiments. The same target system as in the H production was used in the calibration, but both the lower

	H production	(π^-, K^-) calibration
beam	1.8 GeV/c K^-	1.4 GeV/c π^-
target system	LH2/LD2	LH2/LH2
hyperon production	$K^- + p \rightarrow \Xi^- + K^-$	$\pi^- + p \rightarrow \Sigma^- + K^-$
$d\sigma/d\Omega$ at 0° for hyperon production	30 μb/sr	90 μb/sr
favored K^- scattering angle	$\theta_{K^-} \sim 5° - 10°$	$\theta_{K^-} \sim 5° - 10°$
tags for hyperon	$1.00 \leq E_{si} \leq 2.25$ MeV	$1.00 \leq E_{si} \leq 2.25$ MeV
hyperon stopped	$\Xi^- + d \rightarrow (\Xi^-, d)_{atom}$	$\Sigma^- + p \rightarrow (\Sigma^-, p)_{atom}$
hyper-atom decay	$(\Xi^-, d)_{atom} \rightarrow H + n$	$(\Sigma^-, p)_{atom} \rightarrow \Lambda + n$
branching ratio of hyper-atom decay	depending on m_H	$(53.2 \pm 1.0)\%$
E_K of monoenergetic neutron	depending on m_H	43.5 MeV

Table 1.1: Comparison between the H production and the (π^-, K^-) calibration experiments.

and upper target vessels were filled with liquid hydrogen, as shown in Fig. 1.6. The π^- beam was delivered to the lower hydrogen target to produce Σ^-'s through $\pi^- + p \rightarrow K^- + \Sigma^-$. The momentum of the incident π^- beam was chosen to be 1.4 GeV/c so that the kinematics of the Σ^- would match that of the Ξ^- in the H particle search with an incident K^- beam of 1.8 GeV/c, and so that the Σ^-'s stopping probability would be nearly identical to the Ξ^-'s using the same target configuration to slow the hyperons. The Σ^-'s were slowed down by the tungsten degraders; a fraction of Σ^-'s would leave about the same amount of energy in the silicon detector as the Ξ^-'s in the H production search, then stop in the upper

hydrogen target to form the $(\Sigma^-, p)_{atom}$'s. The $(\Sigma^-, p)_{atom}$'s then decayed into a Λ and a 43.5 MeV monoenergetic neutron with 53.2% probability [106]-[107]. The measurement of monoenergetic neutrons in coincidence with tagged Σ^-'s would be used to calibrate the combined stopping efficiency and neutron detection efficiency.

Formation of $(\Sigma^-, p)_{atom}$

In the (π^-, K^+) calibration, the $(\Sigma^-, p)_{atom}$ was formed when the Σ^- was stopped in the upper liquid hydrogen target and captured into a high-n Bohr orbit around the nucleus by replacing an electron. According to Borie and Leon [108], the $(\Sigma^-, p)_{atom}$ will be initially formed in a state with a principal quantum number

$$n \approx \sqrt{\frac{m_p m_\Sigma}{m_p + m_\Sigma}/m_e} \approx 32, \tag{1.10}$$

then cascades down to lower atomic levels, through its own series of bound atomic states by the processes of chemical and Auger deexcitation, radiative transitions, and Stark mixing [4]. In the low principal quantum number (n) state, where the Σ^- is very close to the nucleus, the strong Σ^--nucleus interaction causes a shift in energy of the low atomic levels from its purely electromagnetic value so that those low levels are broadened. Batty [109] used an optical model to calculate the hadronic shift and width of the lower atomic levels. The optical potential was defined as:

$$2\mu V_{opt}(r) = -4\pi(1 + \frac{\mu}{m}) \cdot b_0 \rho(r) \tag{1.11}$$

where μ is the Σ^--nucleus reduced mass, m is the mass of the nucleon, $\rho(r)$ is the proton density distributions normalized to the number of nucleons, and the

[4]Stark mixing: the transitions between the n^2 degenerate states of a given principal quantum number n in the hadronic atom. This process is induced when the hadronic atom passes near or through a hydrogen atom and "feels" its electric field.

complex coefficients b_0 is determined by a least-squares fit to the Σ^--atom data.

Because of its short lifetime, the Σ^- may decay during the atomic cascade before it reaches a low atomic state (small n), being absorbed by the nucleus through the strong interaction. Using the width of the $1s$ state $\sim$ 1 keV calculated from the above optical model and the width of the $2p$ state $\sim$ 0.03 eV estimated from the $\bar{p}p$ calculation, Batty [110] further calculated the probability of hyperon decay during the cascade by using the Borie-Leon model [108]. He found the fraction of Σ^-'s which decay during the cascade depend on the Stark mixing normalization factor K (an arbitrary factor to multiply all Stark mixing rates). Assuming the factor K to be 1.0–2.0, the average Σ^- decay rate was found to be $(15 \pm 5)\%$. In other words, about $(85 \pm 5)\%$ of the $(\Sigma^-, p)_{atom}$'s would still survive after cascading down to $1s$ or $2p$ states. Batty calculated the average survival probability for the $(\Xi^-, d)_{atom}$ to be $\sim 80\%$ [109].

Rate of $(\Sigma^-, p)_{atom} \rightarrow \Lambda + n$

There are two decay channels for the $(\Sigma^-, p)_{atom}$: $(\Sigma^-, p)_{atom} \rightarrow \Lambda + n$ and $(\Sigma^-, p)_{atom} \rightarrow \Sigma^0 + n$. Traditionally, studies have been made of the branching ratio to $\Sigma^0 n$, defined as:

$$r_R = \frac{\sigma_R(\Sigma^- p \rightarrow \Sigma^0 n)}{\sigma_R(\Sigma^- p \rightarrow \Lambda n) + \sigma_R(\Sigma^- p \rightarrow \Sigma^0 n)}. \tag{1.12}$$

where σ_R denotes the total cross section for the respective Σ^- capture reaction at rest. The branching ratio of interest to this experiment is for the reaction $(\Sigma^-, p)_{atom} \rightarrow \Lambda + n$ and can be calculated from

$$R_\Lambda = 1 - r_R \tag{1.13}$$

The Nagels group [102] calculated the ratio of Σ^- capture at rest, in a one-boson-exchange potential model. They constructed the baryon-baryon interaction

potential by taking into account complete nonets of pseudoscalar, vector mesons, and the scalar-meson unitary singlet at long distances, while employing hard cores at short distances. Five free parameters were determined in their model by a least-squares fit to the low energy hyperon-nucleon scattering total cross section data and the capture ratio at rest for the $\Sigma^- p$ channel. This model gives good explanations simultaneously to both hyperon-nucleon and nucleon-nucleon data in the low energy region. Table 1.2 shows the comparison of the ratio for Σ^- capture at rest between Nagels' calculation and the measurements. As seen from the Table, the agreement is very good. The average of the two measurements for the ratio of Σ^- capture at rest is $r_R = 0.468 \pm 0.010$, corresponding to the branching ratio of $(\Sigma^-, p)_{atom} \rightarrow \Lambda + n$, $R_\Lambda = (53.2 \pm 1.0)\%$.

	Theoretical result	**Measurement**	
		exp1 [106]	exp2 [107]
r_R	0.4775	0.474 ± 0.016	0.465 ± 0.011

Table 1.2: Ratio of Σ^- capture at rest.

Experiment E813 started in 1991, and real production runs were conducted in 1992, 1993 and 1995. During the time, the (π^-, K^-) calibration data were collected. About 10% of the (π^-, K^-) calibration data were taken in 1993 while 90% of the data were taken in 1995. In this thesis, the analysis of the 1995 (π^-, K^-) calibration data is discussed. **Chapter 2** describes the experimental arrangement and procedures. The data analysis is presented in **chapter 3**, while the final result and a discussion are presented in **chapter 4**.

Chapter 2

Experimental Setup

2.1 Overview

The main objective of the (π^-, K^+) calibration was to measure the 43.5 MeV energy neutrons produced through the $(\Sigma^-, p)_{atom} \rightarrow n + \Lambda$ reaction, in order to calibrate the combined hyperon stopping efficiency and the neutron detection efficiency, $\varepsilon_{stop} \cdot \eta_{ND}$, for the H particle search. To do this, one needed to detect the monoenergetic neutrons in coincidence with tagged Σ^-'s which had the highest probability of stopping in the upper liquid hydrogen target to form $(\Sigma^-, p)_{atom}$'s. This goal was carried out in three steps: Σ^- production and identification, tagging the stopping Σ^-'s, and finally the monoenergetic neutron detection.

As shown in Fig. 2.1, the experimental area was divided into four main sectors according to their locations and functions. The first sector was the beamline, which was used to deliver a 1.4 GeV/c π^- beam to the lower hydrogen target (see Fig. 1.6) to produce Σ^-'s through the $\pi^- + p \rightarrow \Sigma^- + K^+$ reaction. The second sector was the 48D48 spectrometer, which was used to measure the momentum and the time-of-flight of the scattered particles. The outgoing K^+'s were subsequently identified through a secondary mass calculation. As a result, Σ^-'s, produced through $\pi^- + p \rightarrow \Sigma^- + K^+$, were identified by a missing mass calculation through

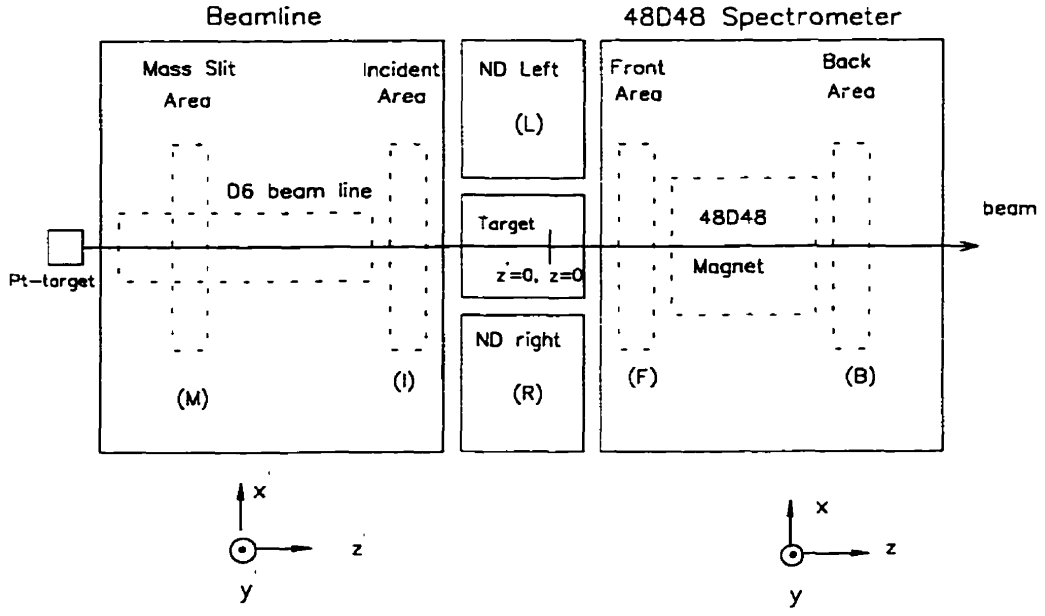

Figure 2.1: Schematic diagram of the experimental setup. The solid boxes divide the experimental area into sectors, and the dashed boxes further divide the sector into a few sub-areas. (x', y', z') is the beam line coordinate system, and (x, y, z) is the H particle coordinate system. The two coordinate systems overlap in the target sector, and their intersection point defines the origin for both systems.

two-body kinematics by combining the momentum information of the π^-'s and the K^+'s. The third sector was the target. Σ^-'s were produced in the lower target and the ones which had the highest probability of stopping in the upper target were tagged by the silicon detectors (shown in Fig. 1.6). The fourth sector was the ND (the neutron detectors) sector, which was used for neutron energy measurement by measuring the time-of-flight and the path length. Furthermore, the beamline sector and the 48D48 spectrometer sector were divided into a few sub-areas. The detectors in the mass slit area and in the incident area (immediately upstream of the target) combined with the last dipole in the beam line were used as a focusing spectrometer for beam particle identification, while the detectors in the front area and in the back area combined with the 48D48 magnet were used as an open

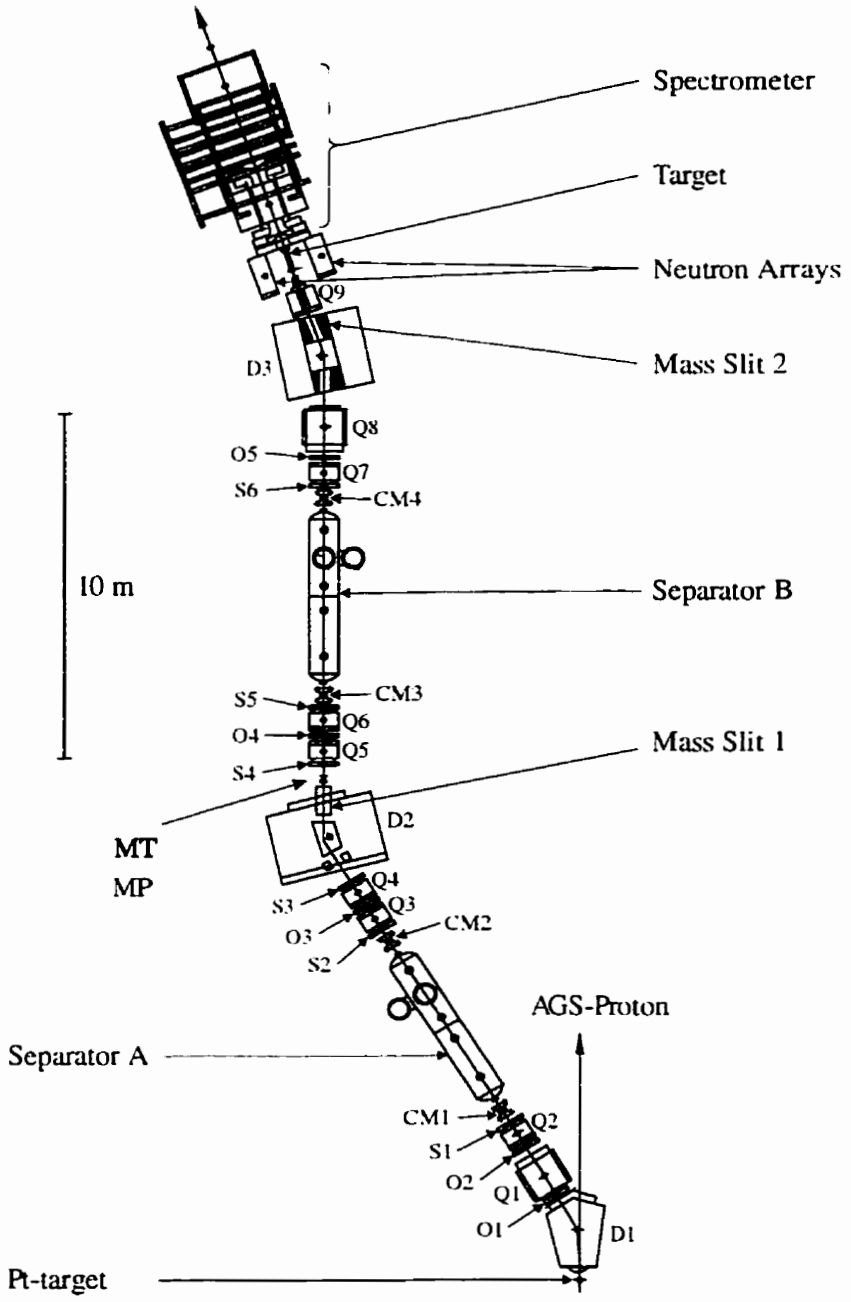

Figure 2.2: Plan view of the E813 experiment layout. The beamline sector begins right after the Pt-target, and ends at the front end of the experimental target; the various beamline elements are described in Fig. 2.4. The other sectors are shown in the figure as labeled.

spectrometer for scattered particle identification (the detectors in the beamline spectrometer and in the 48D48 spectrometer are highlighted in later Fig. 2.5). Fig. 2.2 shows the complete experimental setup. In the following sections, the details of each part of the apparatus are discussed.

2.2 Conventions

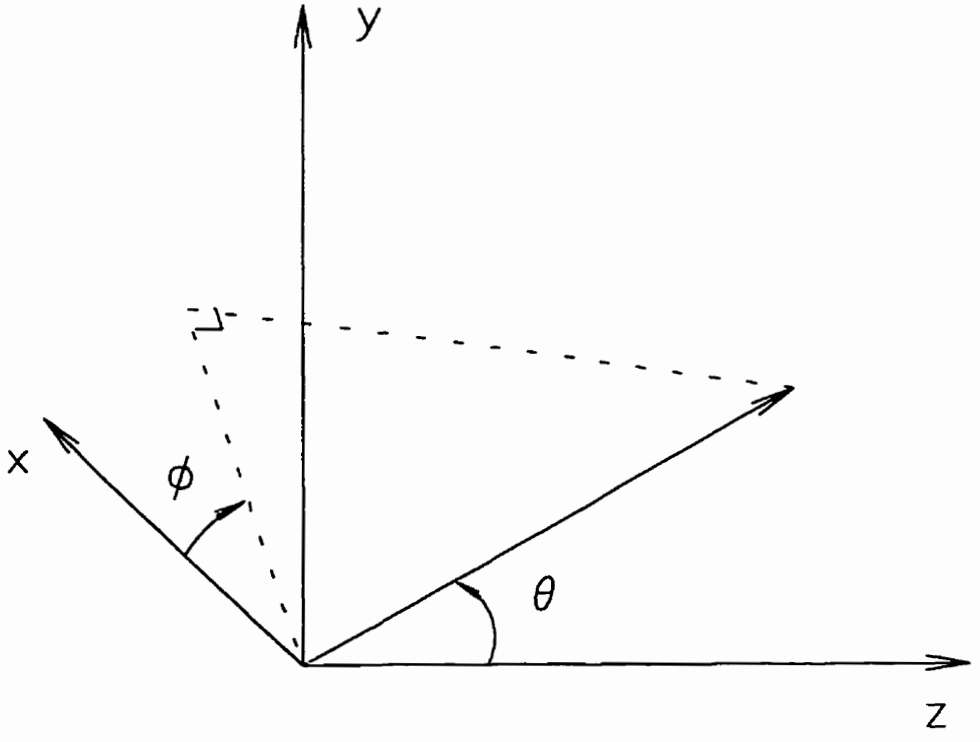

Figure 2.3: Definitions of the directional angles θ and ϕ.

As shown in Fig. 2.1, two separate coordinate systems were used to describe this experiment. The first was the beamline coordinate system (x', y', z'), which was defined between the production target and the experimental target. The z'

axis was along the central ray of the beam line[1]; its positive direction pointed downstream with regard to the beam. The y' axis was vertical and with positive direction up, and the x' axis was defined by a right-handed coordinate system. The second coordinate system was the H coordinate system (x,y,z). It was defined between the front end of the incident area (right after the last quadrupole Q9 in the beam line. Shown in Fig. 2.2) and the back end of the 48D48 spectrometer sector. The z axis direction of the H coordinate system was fixed along the beam direction immediately after the quadrupole Q9, and the x and y axes had the same definitions as in the beamline coordinate system. The two coordinate systems overlapped at a nominal point in the experimental target area, and this point was set to be the origin for both coordinate systems. The directional angles θ and ϕ were defined as shown in Fig. 2.3.

The detector names conventionally had two letters and an optional digit. The first letter stood for the location of the detectors. M, I, F and B represent the Mass slit area, the Incident area, the Forward area and the Back area respectively. The second letter stood for the detector type or function, such as D for drift chamber, C for Čerenkov detector, P for position information, and T for timing information. The optional digit was used if there were multiple similar detectors in the same area.

2.3 Beamline Sector

The beamline sector started right after the platinum production target, and ended at the front end of the experimental target; Fig. 2.4 gives a plan view of this sector. As shown in Fig. 2.1, the beamline sector consisted of three parts: the D6 beam line, mass slit area detectors and incident area detectors.

[1]The central ray of the beam line: is the optimum trajectory of the beam particle with a specific momentum passing through the centers of the three dipoles in the beam line.

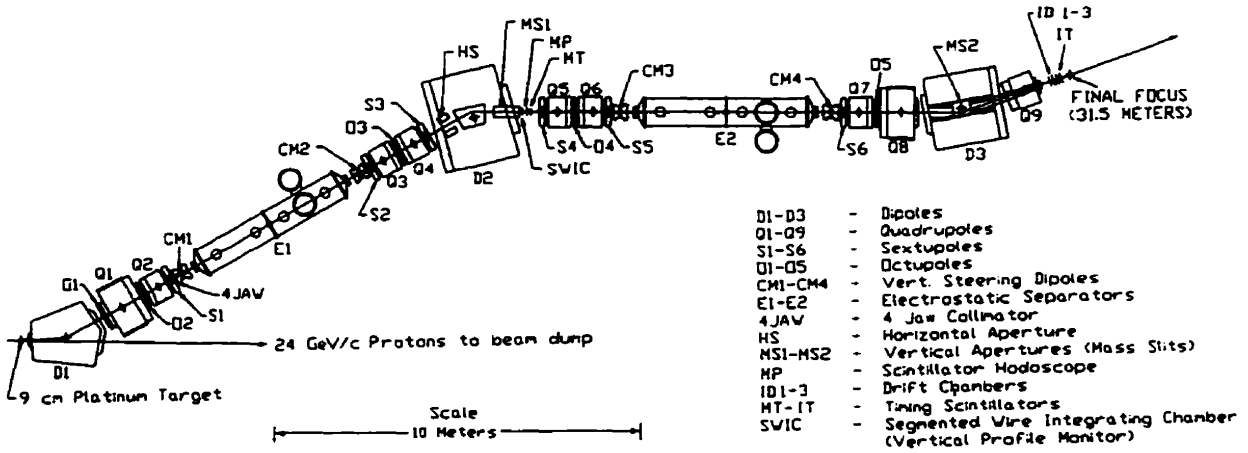

Figure 2.4: Plan view of the D6 beam line at BNL.

2.3.1 The D6 Beam line

The experiment was carried out on the D6 beamline of the Alternating Gradient Synchrotron (AGS) at Brookhaven National Laboratory (BNL). The beam line was originally designed to deliver 1.9×10^6, 1.8 GeV/c K^-/spill per 6.5×10^{12} protons, with the beam purity approaching $K^-/\pi^- \geq 2:1$ for the H particle search experiments E813 and E836. In the present (π^-, K^-) calibration experiment, it was used to deliver a 1.4 GeV/c π^- beam, with 6.3×10^6 pions/spill per 3.6×10^{12} protons and a $\pi^-/K^- \geq 500:1$ requirement easily satisfied. The details of the beam line are described in Ref. [112]. As shown in Fig. 2.4, a 9.0 cm long, 0.7 cm wide and 1.0 cm high platinum production target was placed in the entrance to the first dipole (D1), being able to withstand $\leq 1.5 \times 10^{13}$ 24 GeV/c protons per 1.2 second AGS spill every 2.5 second. The secondary beam was transported with an extraction angle of 5° to the primary beam, then deflected 25° by dipole D1 into the D6 beam line. Two electrostatic velocity separators (E1 and E2) and two

Momentum range	1-2 GeV/c
Momentum acceptance (FWHM)	±3%
Horizontal acceptance (FWHM)	+55, -35 mrad
Vertical acceptance (FWHM)	+7, -6 mrad
Final focus (Horizontal waist at $z = -20$ cm)	Horizontal image size (rms)=1.5 cm Horizontal divergence (rms)=7.0 mrad Vertical image size (rms)=0.1 cm Vertical divergence (rms)=4.7 mrad
K^- flux, 1.8 GeV/c, $K^-/6.5 \times 10^{12}$ protons	1.9×10^6/spill
Direct K^-/π^- ratio, 1.8 GeV/c K^- beam with two separators working at full voltages	1:2 (without four-jaw cut) $\geq$ 2:1 (with four-jaw cut)
π^- flux, 1.4 GeV/c, $\pi^-/3.6 \times 10^{12}$ protons	$\sim 6.3 \times 10^6$/spill
Direct π^-/K^- ratio, 1.4 GeV/c π^- beam with one separator working at 80% full voltage	$\geq$ 500:1 (with four-jaw cut)
Momentum spread (rms)	0.3%

Table 2.1: Important features of the D6 beamline at BNL.

vertical mass slit apertures (MS1 and MS2) were used for particle separation, with the mass slits being located at different vertical foci. The three dipoles (D1, D2 and D3) in the beam line were set to allow particles with a specific momentum to follow an optimum trajectory through their centers, known as the central ray. The secondary beam was transported in vacuum to the first mass slit (MS1) entrance and then through a 0.0076 cm thick aluminum window into air to the entrance of sextupole S4. The space between MS1 and S4 was for inserting experimental detectors, a scintillator hodoscope (MP) and a timing scintillator array (MT), so that the detectors were near a horizontal and vertical focus to minimize the effects of multiple scattering. The beam was then transported in vacuum through the second mass slit (MS2) to the exit of the last quadrupole magnet, Q9. The beam line incorporated 9 quadrupoles, 6 sextupoles, 5 octupoles and specialized collimators (a four-jaw collimator and a horizontal aperture). In order to minimize the vertical beam width at the mass slits, the beam optics were partially corrected to third order. The last dipole, D3, combined with the scintillating detector (MP)

in the mass slit area and the drift chamber detectors (ID1–3) in the incident area formed a beam spectrometer. The beam momentum was calculated from particle tracking by using TRANSPORT program [113], and the beam momentum spread was measured at $\leq 0.3\%$. The main features of the D6 beam line are described in Table 2.1 [112].

2.3.2 Mass Slit Area Detectors

The mass slit area detectors consisted of scintillating detectors MP and MT, which were located in the first mass slit area of the beam line after dipole D2, as shown in Fig. 2.4. The descriptions of the detectors MP and MT are given below, and their relative locations are shown in Fig. 2.5.

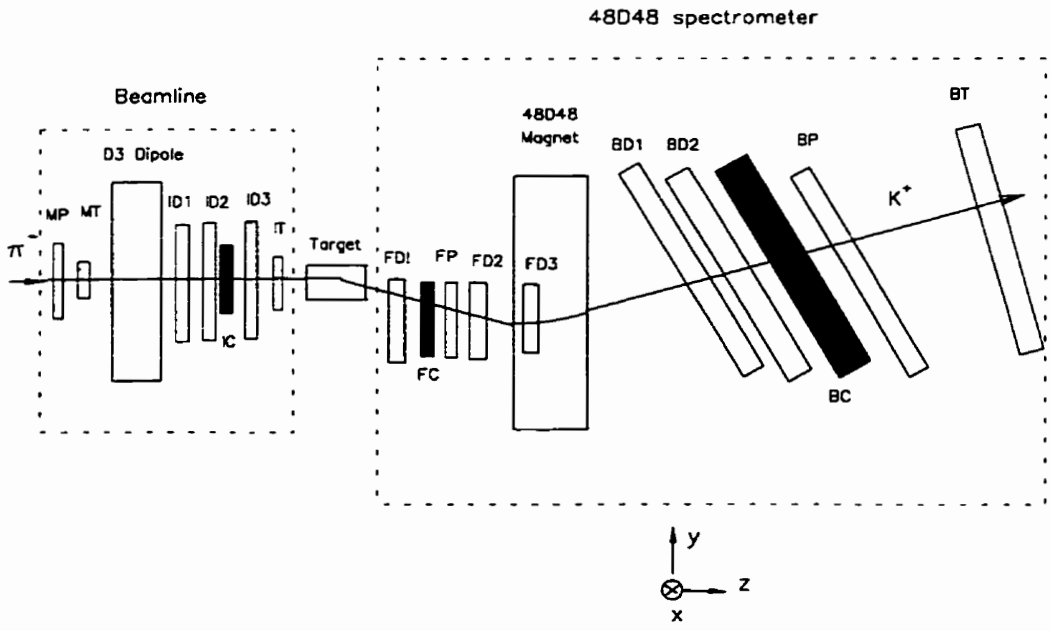

Figure 2.5: Schematic plot of the detectors in the beam spectrometer and the 48D48 spectrometer.

MP

MP was a 72 element detector, with its center located at $x' = 0.0$ cm, $y' = 0.0$ cm, and $z' = -440.0$ cm in the beamline coordinate system. Each element was a rectangular BC408 scintillator with dimensions 0.7 cm × 1.5 cm × 0.3 cm ($x' \times y' \times z'$). They were arranged vertically in two overlapping layers to get the better x' position measurement of the beam particles. The active width of MP along the x' direction was 33.3 cm. Only one R647-01 Photo Multiplier Tube (PMT) was installed for every element. By identifying which element of the detector fired, MP was used to measure the x' position of beam particles in the mass slit area, in order to calculate the momentum of the beam particles by combining the x position and directional angle θ information from three drift chambers in the incident area. Both ADC (analog-to-digital converter) and TDC (time-to-digital converter) information from MP were recorded.

MT

Another detector in the mass slit area was the Mass slit Timing (MT) detector, used to measure the time-of-flight of the beam particles. It had 9 elements segmented horizontally. Each element was made of a BC408 rectangular scintillator, with dimensions of 3.7 cm × 1.5 cm × 0.635 cm ($x' \times y' \times z'$). The center to center distance between adjacent elements was 3.7 cm; this made the active width of MT 33.3 cm along the x' direction, which matched the width of MP. Both ends of each MT element had RCA8575 PMT's. The center of MT was located at $x' = 0.0$ cm, $y' = 0.0$ cm, and $z' = -430.0$ cm in the mass slit area. Constant Faction Discriminators (CFD) were used for optimum time resolution. For fixed beam momentum, the difference of the time-of-flight from MT to the downstream beamline detector IT was used to select the beam particles.

2.3.3 Incident Area

In the incident area, there were three drift chambers (ID1–3), one Čerenkov detector (IC), and one scintillating detector (IT). Their relative locations are shown in Fig. 2.5.

Drift Chambers ID1–3

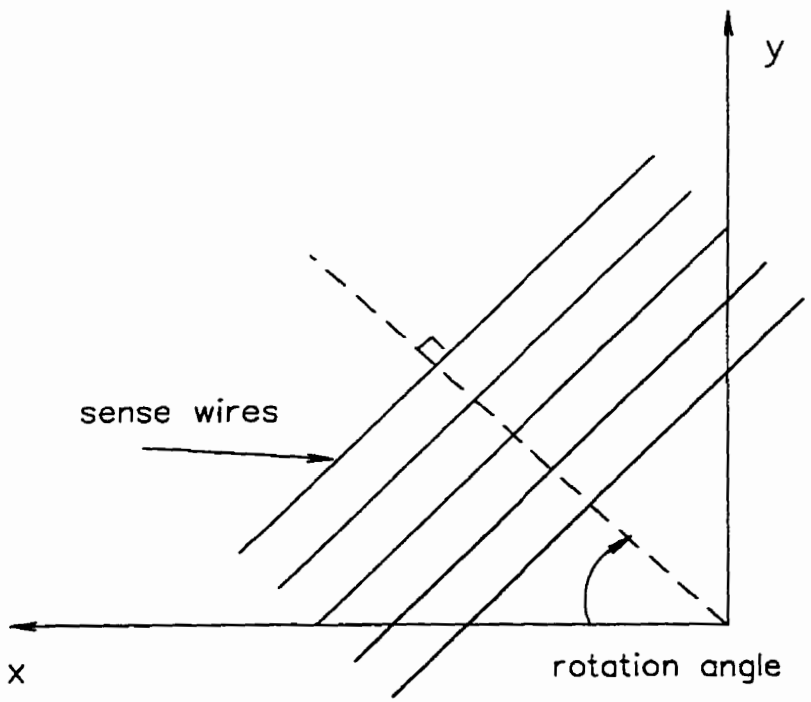

Figure 2.6: Definition of the rotation angle for the sense wires in the drift chambers. For example, the sense wires are parallel to the x axis if the rotation angle is 90°.

Three identical drift chamber detectors (ID1, ID2, ID3) were installed in succession in front of the experimental target to measure the track direction and the x position of the beam particles. This information, in combination with the x' position information from MP in the mass slit area, was used to calculate the

Chamber	Planes	Rotation angle	Spacing (cm)	Location(cm)			Resolution (cm)	Channels
				x	y	z		
ID1	u-u'	120°	0.508	0.00	-0.07	-135.19	0.015	24×2
	v-v'	60°	0.508				0.015	24×2
	x-x'	0°	0.508				0.015	24×2
ID2	u-u'	120°	0.508	0.12	0.10	-118.49	0.015	24×2
	v-v'	60°	0.508				0.015	24×2
	x-x'	0°	0.508				0.015	24×2
ID3	u-u'	120°	0.508	0.15	-0.05	-87.95	0.015	24×2
	v-v'	60°	0.508				0.015	24×2
	x-x'	0°	0.508				0.015	24×2

Table 2.2: Specifications of the ID chambers. The definition of the rotation angles is shown in Fig. 2.6. Spacing: the chamber sense wire spacing; Location: the center of the chamber position; Resolution: position measurement resolution.

momentum of the beam particles by using a TRANSPORT program [113]. Because the ID chambers were in-beam detectors, they were designed for high rate operation; each ID chamber could tolerate up to 6.3×10^6 particles per second. There were a pair of $x - x'$ planes, a pair of $u - u'$ planes and a pair of $v - v'$ planes (the definition of the planes given in Table 2.2) in a chamber. This configuration gave the best resolution for the x position measurement. Table 2.2 gives detailed information about the ID chambers. The active area for each chamber was hexagonal, 12.2 cm across in the x direction and 10.6 cm high in the y direction. The gas mixture used for the operation of the ID chambers was 76% argon, 20% isobutane, and 4% methylal.

Čerenkov Detector IC

In order to separate the beam particle π^-'s from K^-'s for the online trigger, a Čerenkov detector was installed at $z = -96$ cm, in between ID2 and ID3. IC was made of an aerogel radiator with index of refraction $n = 1.03$. When a charged particle traverses a dielectric medium, with its velocity exceeding the velocity of

light in this material, a small number of photons will be emitted at a fixed angle. This is called the Čerenkov effect. The threshold velocity for Čerenkov emission is defined by the index of refraction n:

$$\beta_{th} = \frac{1}{n} \tag{2.1}$$

where $\beta = \frac{v}{c}$, and v and c are the speed of light in the dielectric medium and vacuum respectively. Therefore, with $n = 1.03$ aerogel radiator, the threshold momentum for K^- ($m_{K^-} = 0.49368$ GeV/c^2) is

$$P_{K^-} = \frac{m_{K^-} \cdot c \cdot \beta_{th}}{\sqrt{1-\beta_{th}^2}} = \frac{m_{K^-} \cdot c \cdot \frac{1}{n}}{\sqrt{1-(\frac{1}{n})^2}} = 2.0 \quad \text{(GeV/c)} \tag{2.2}$$

The threshold momentum for π^- ($m_{\pi^-} = 0.13957$ GeV/c^2) is

$$P_{\pi^-} = \frac{m_{\pi^-} \cdot c \cdot \beta_{th}}{\sqrt{1-\beta_{th}^2}} = \frac{m_{\pi^-} \cdot c \cdot \frac{1}{n}}{\sqrt{1-(\frac{1}{n})^2}} = 0.567 \quad \text{(GeV/c)} \tag{2.3}$$

Thus, only K^-'s with momentum greater than 2.0 GeV/c and π^-'s with momentum greater than 0.567 GeV/c would cause emission of Čerenkov radiation from IC. In the case of the (π^-, K^-) calibration run, a 1.4 GeV/c π^- beam was used. As a result, IC would have output signals only when π^-'s passed through it.

The IC consisted of two aerogel blocks with dimensions of 10.0 cm × 5.0 cm × 3.0 cm ($x \times y \times z$). The Čerenkov light was received by a mirror of aluminized mylar downstream of the aerogel blocks and was reflected to a Hamamatsu R1250 photo multiplier tube (PMT) through a Lucite light guide. Fig. 2.7 gives a side view of IC. The efficiency of IC was 99.7% as determined in a 1.8 GeV/c π^- beam test [114].

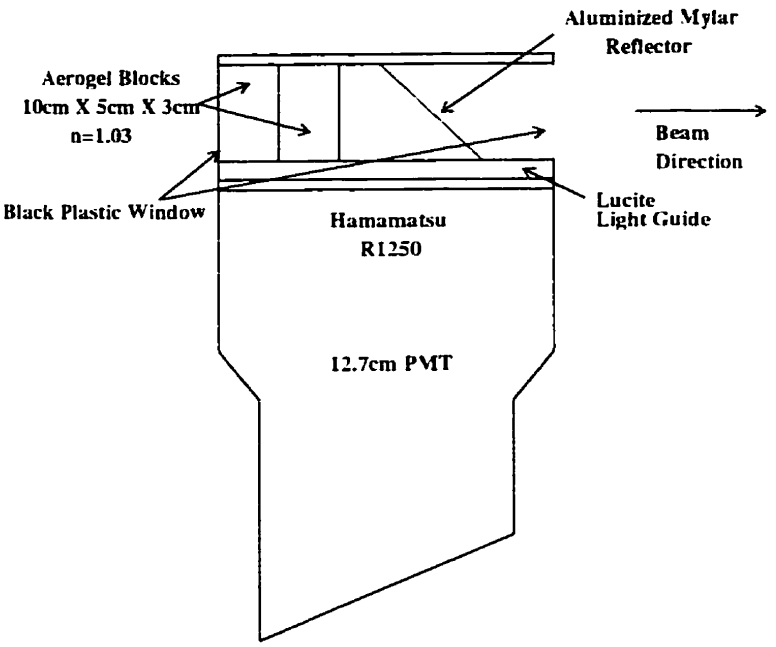

Figure 2.7: Side view of IC.

IT

One of the key detectors in the experiment was IT, which provided the time reference for all the other detectors and time-of-flight measurements. IT consisted of four scintillating elements arranged vertically, with adjacent elements staggered from each other side by side. Each element was a 2.5 cm wide, 3.0 cm high, and 1.27 cm thick BC408 scintillator. The total width of IT was 10.0 cm. The center of IT was located at $x = 0.0$ cm, $y = 0.0$ cm, and $z = -71.8$ cm in the H coordinate system. Because IT timing information was crucial for the whole experiment, RCA8575 PMT's were mounted on both ends of each element, and

constant fraction discriminators (CFD) were used for better time resolution. The intrinsic time resolution of IT varied from bar to bar with an average value of $\sigma = 130$ psec.

2.4 The 48D48 Spectrometer Sector

The main function of detectors in the 48D48 spectrometer sector was to identify the scattered K^-'s by measuring their momentum and time-of-flight. The 48D48 spectrometer sector can be further divided into three sub-areas (see Fig. 2.1): (1) the front area detectors, which measured the tracks of scattered particles in front of the magnet; (2) the 48D48 magnet, which bent the particles in the vertical direction; (3) the back area detectors, which measured the tracks of scattered particles behind the magnet, and also measured the time-of-flight of scattered particles. Fig. 2.5 shows the layout of the detectors in the 48D48 spectrometer sector.

2.4.1 Front Area

In the front area, there were three drift chambers (FD1, FD2 and FD3), a scintillating detector, FP, and a Čerenkov detector, FC. These detectors are described in detail below.

Drift Chambers FD1-3

There were three drift chamber detectors (FD1 and FD2 in front of the magnet and FD3 inside the magnet) to measure the tracks of the scattered particles before traversing the magnet. Because the particles were bent vertically by the magnet, the vertical positions of the particles gave information about their momentum. The FD chambers were designed with a y-u-v (see Table 2.3) configuration in order to obtain better y resolution. FD3 was placed inside the 48D48 magnet

Chamber	Planes	Rotation Angle	Spacing (cm)	location(cm)			Resolution (cm)	channels
				x	y	z		
FD1	u-u'	210°	0.508	0.07	-6.83	31.12	0.015	48× 2
	v-v'	150°	0.508				0.015	48×2
	y-y'	90°	0.508				0.015	48×2
FD2	u-u'	210°	0.508	-0.02	-6.90	66.92	0.015	48×2
	v-v'	150°	0.508				0.015	48×2
	y-y'	90°	0.508				0.015	48×2
FD3	u	150°	1.27	0.18	-0.69	149.04	0.030	64
	y-y'	90°	1.27				0.030	64×2
	v	30°	1.27				0.030	64

Table 2.3: Specifications of the FD chambers. The rotation angles are defined in Fig. 2.6. Spacing: the chamber sense wire spacing; Location: the center position of the chamber; Resolution: position measurement resolution.

aperture for better determination of positions. The discriminated signals of y hits from FD3 were also used as input for the second level trigger, described later. The maximum drift times for FD1 and FD2 were about 50 nsec, and for FD3 was about 125 nsec. The specifications of all FD chambers are shown in Table 2.3. The gas mixture used for the operation of the FD chambers was 76% argon, 20% isobutane, and 4% methylal.

Čerenkov Detector FC

The aerogel Čerenkov detector FC was used to separate the K^-'s from π^-'s among the scattered particles. The index of refraction of the radiator blocks of FC was $n = 1.04$; therefore, as calculated by using eq. (2.1), (2.2) and (2.3), the Čerenkov radiation thresholds of FC were at 1.729 GeV/c for K^-'s and 0.49 GeV/c for π^-'s. For the $\pi^- + p \rightarrow \Sigma^- + K^-$ reaction with 1.4 GeV/c beam momentum, the momentum of outgoing K^-'s was in the range $0.74 - 0.96$ GeV/c. As a result, with momentum around $0.74 - 0.96$ GeV/c, π^-'s were able to fire FC while K^-'s were not. This property of FC was used in a hardware trigger to veto π^-'s. The

efficiency of FC was measured to be 98.6% in a 1.8 GeV/c π^- beam test [114].

The center of FC was located at (0.0cm.-6.8cm.44.0cm). in between FD1 and FP. and upstream of the 48D48 dipole magnet shown in Fig. 2.5. The dimensions of the aerogel blocks were 25 cm wide. 25 cm high. and 9 cm thick. Both top and bottom ends of the aerogel blocks had two Hamamatsu R1250 PMTs to collect the Čerenkov light. A schematic drawing of FC is shown in Fig 2.8.

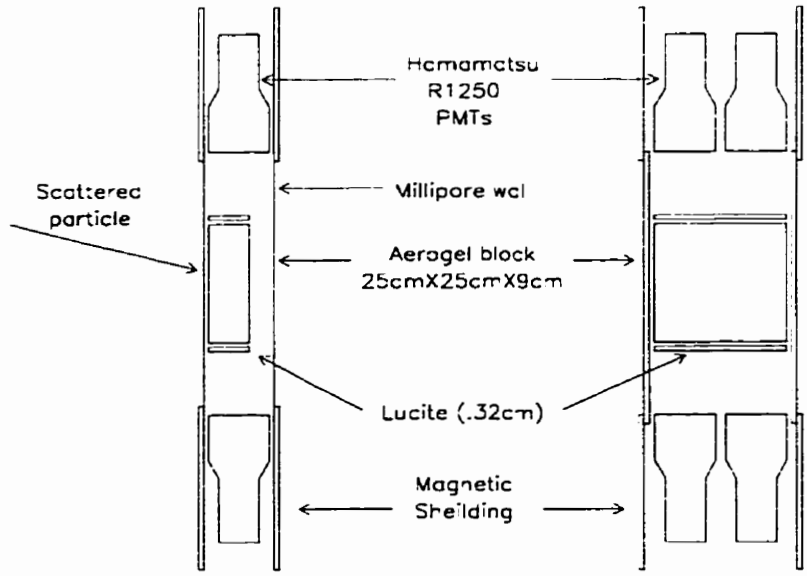

Figure 2.8: Schematic drawing of Čerenkov detector FC. The left hand side is the side view and the right hand side is looking downstream along the beam direction.

Scintillator Hodoscope FP

FP was a 16 element scintillator detector, segmented along the y axis to provide a fast measurement of the y position for the scattered particles, and to veto the beam particles for the online trigger definitions. Modules #1–#12 were traversed by scattered particles only, while modules #13–#16 were traversed by beam particles also. FP was used to define the vertical acceptance of the spectrometer at about $-13.2° \leq \theta_Y \leq 0.6°$, and the size of FP was designed to match the size of FC so that all the events recorded by FP would be identified by the Čerenkov detector FC. Each element of hodoscope FP was made of BC408 scintillator with dimensions 24.0 cm wide, 1.5 cm high, and 0.4 cm thick. The adjacent elements had flush alignment. The center of FP was located at $x = 0.0$ cm, $y = -6.8$ cm, and $z = 60.0$ cm in the H particle coordinate system.

2.4.2 The 48D48 Magnet

The 48D48 magnet was a dipole magnet. Its pole face was 48″ × 48″ with a gap of 31.5″. The bend plane of the 48D48 was in the $y - z$ plane, therefore, the field direction was horizontal and particles were bent vertically. As Fig. 2.9 shows, the scattered particles were bent up to the back area of the spectrometer, while the beam particles were bent down to the ground. In the H particle production run, the central magnetic field was set to be 1.4 Tesla in order to bend a typical 1.2 GeV/c K^- by 30° through the spectrometer. In the (π^-, K^-) calibration run, the magnetic field was reduced to 0.94 Tesla in order to bend a typical 0.85 GeV/c K^- from the $\pi^- + p \rightarrow \Sigma^- + K^+$ reaction by the same angle. The center of the 48D48 magnet was at $z = 200$ cm in the H coordinate system. For a typical K^- from the (π^-, K^-) calibration run scattered from (0, 0, 0) in the H particle coordinate system, the angular acceptance of the spectrometer was about 51.7 msr (for $0° \leq \theta_{K^-} \leq 22°$ and $180° \leq \phi_{K^-} \leq 360°$).

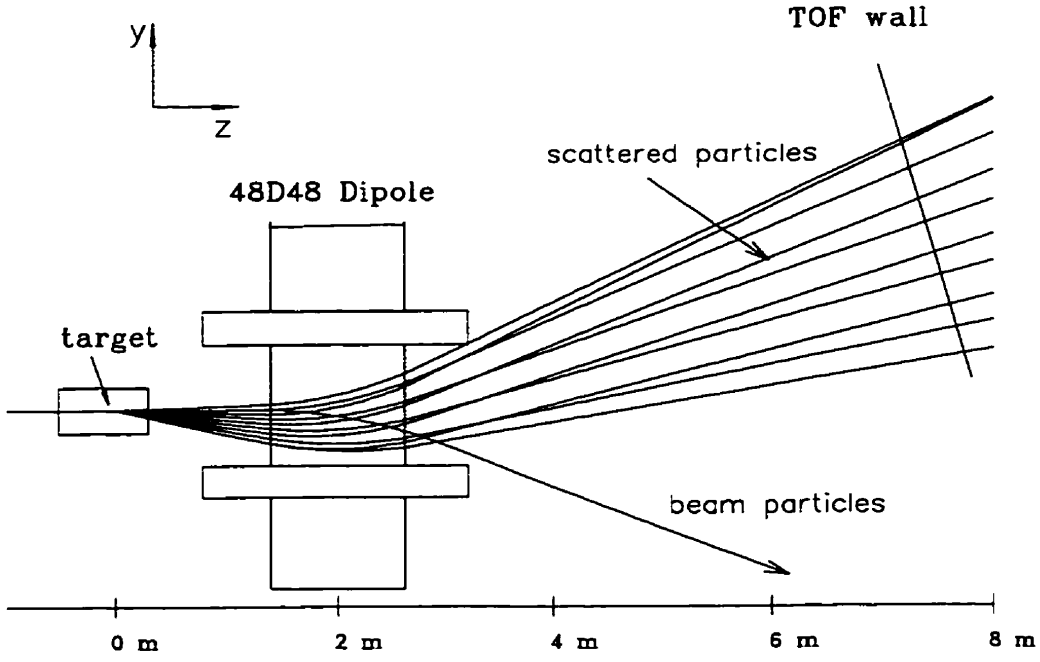

Figure 2.9: Schematic diagram of spectrometer magnet. The scattered particles were bent up, and the beam particles bent down to the ground.

2.4.3 Back Area

In the back area of the spectrometer, there were two large drift chambers (BD1 and BD2), a Čerenkov detector BC, a scintillator detector, BP, and a time-of-flight wall detector BT. Their relative locations are shown in Fig. 2.5, and the details of each detector are described below.

Drift Chambers BD1-2

Chamber	Planes	Rotation Angle	Spacing (cm)	location(cm)			Resolution (cm)	channels
				X	Y	Z		
BD1	u	120°	2.0	-0.41	68.60	373.17	0.030	128
	v	60°	2.0				0.030	128
	y-y'	90°	2.0				0.030	112×2
BD2	u	120°	2.0	-0.04	69.39	455.89	0.030	128
	v-v'	60°	2.0				0.030	128×2
	y-y'	90°	2.0				0.030	112×2

Table 2.4: Specifications of the BD chambers. The rotation angle is defined in Fig. 2.6. Spacing: the chamber sense wire spacing; Location: the center position of the chamber: Resolution: position measurement resolution.

Two drift chamber detectors (BD1 and BD2) were used to measure the tracks of the scattered particles behind the magnet. Thus the trajectories of the scattered particles throughout the spectrometer area were reconstructed by combining the track information from the FD chambers and BD chambers. As a result, the momentum of the scattered particles was then determined.

As the direction of each scattered particle was rotated by the spectrometer magnet by approximately a 30° angle from the z axis, the back chambers were inclined at 30° from the y axis, as shown in Fig. 2.5, so that the particles could pass through the BD wire planes perpendicularly. The active areas of BD1 and BD2 were 114.0 × 214.0 cm^2. Table 2.4 lists more detailed information about the

BD chambers. The gas mixture used for the operation of the BD chambers was 79% argon, 17% isobutane, and 4% methylal.

Čerenkov Detector BC

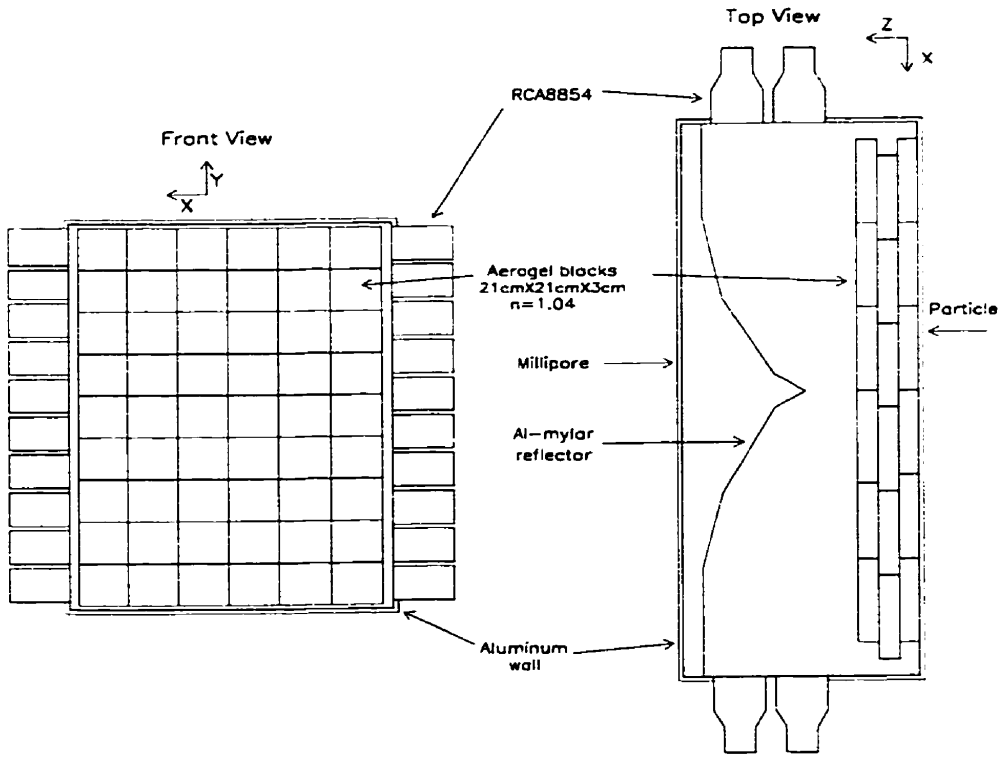

Figure 2.10: Schematic drawing of Čerenkov detector BC.

As K^-'s might decay into π^-'s or other lighter particles during their flight through the spectrometer, there was also an aerogel Čerenkov detector BC in the back area to separate the scattered K^-'s from their decay particles. The refractive index of aerogel blocks used in BC was the same as in FC with $n = 1.04$. As a result, BC could only be fired by π^-'s or other lighter particles but not by K^-'s, under the experimental conditions. The signals of BC were also used in the online trigger

definitions to veto pions or other lighter particles. As shown in Fig. 2.10, BC consisted of three layers, and each layer had 54 aerogel blocks, adding up to a total 162 blocks. Each block was 21 cm wide, 21 cm high, and 3 cm thick. Therefore, the particles would pass through a total of 9 cm thickness of aerogel radiator. The Čerenkov light was reflected by an aluminized mylar reflector, and collected by 20 RCA8854 PMTs on each side of the detector. The efficiency of BC was measured to be 98.5% in a 1.8 GeV/c π^- beam test [114]. BC was inclined at 30° relative to the y axis, and its center was located at (0.0cm,69.0cm,481.0cm) in the H particle coordinate system.

Scintillator Detector BP

A 6 element scintillator detector BP, segmented along the x axis, defined the horizontal acceptance of the spectrometer with angular coverage of $|\theta_x| \leq 6.4°$. The combination of information from BP and upstream FP was used to define the online trigger, signaling that a charged particle had passed through the spectrometer. The active area of BP was matched to BC to ensure the particles recorded had passed through BC. Each BP element was made of 21.0 cm wide, 180.0 cm high, and 1.0 cm thick BC408 scintillator, adding up to a total active area of 126 × 180 cm^2. An XP2262 PMT was mounted on both ends of each element. The center of BP was located at (1.3 cm, 106.4 cm, 524.4 cm) in the H coordinate system, and inclined at 30° relative to the y axis so that particles were incident on the detector approximately perpendicular.

Time-of-flight Wall Detector BT

At the back of the spectrometer area, there was a time-of-flight wall detector BT to measure the time-of-flight of the scattered particles. A detailed description of BT was given in [115]. Unlike other detectors in the back area, BT was inclined at 15° instead of 30° to the y axis. According to a Monte Carlo simulation, when BT

is inclined at 15°, the same kind of particles emitted from a point source at the target area with the same momentum at small differing angles have the smallest separation in their path lengths, and consequently in their time-of-flight, so that the spread in the time-of-flight peak for the same kind of particle within a single BT element is minimized. Therefore, the time-of-flight separation between K^+'s and background particles (like protons) in a single BT bar is maximal, which is of benefit for the second level trigger to be discussed later.

BT consisted of 40 bars. Each bar was made of BC408 scintillator, 200 cm wide, 8.5 cm high, and 5.0 cm thick. Each bar was viewed by two 2.3 nsec rise-time, 2 inch diameter Hamamatsu H1949 photomultiplier tubes (PMTs), one at each end. Individual bars were rotated to 30° from the y axis so that the particles would pass through them perpendicularly. Fig. 2.11 shows the schematic layout of BT. The center of BT was at (-1.1 cm, 207.8 cm, 739.6 cm) in the H coordinate system, and its active area was 200×320 cm^2. The intrinsic time-of-flight resolution varied from bar to bar with an average σ of 110 psec. The effective light velocity in the bars was 15.0 ± 0.4 cm/nsec. Both ADC and TDC were recorded for each PMT.

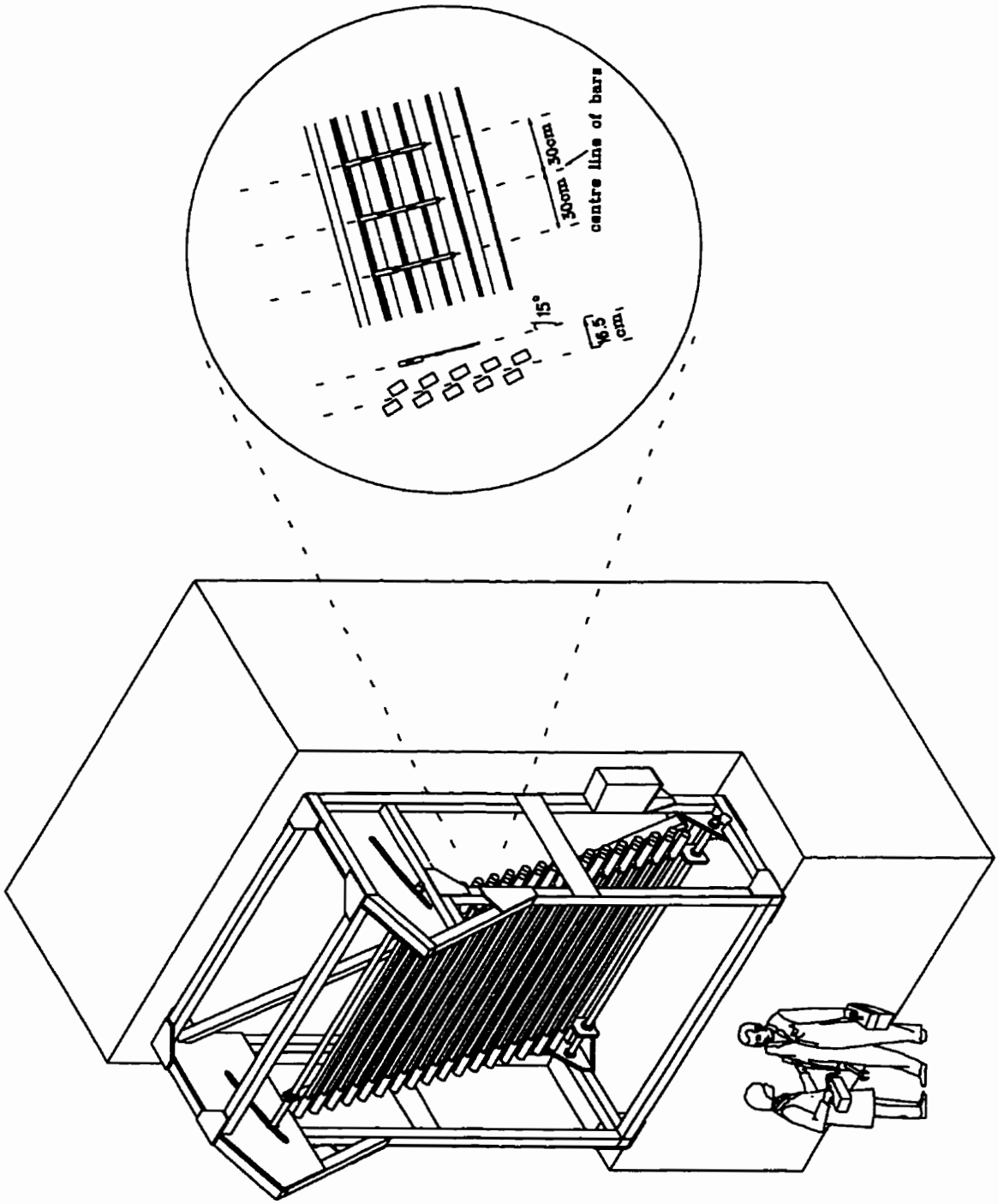

Figure 2.11: Schematic diagram of BT.

2.4.4 Target Sector

The heart of the experiment was the target. In the target area, Σ^-'s were produced, and then were slowed down by tungsten degrader and captured on hydrogen to form $(\Sigma^-, p)_{atom}$'s. Σ^-'s which had the highest probability to stop in the upper hydrogen target to form $(\Sigma^-, p)_{atom}$'s were tagged. These were carried out by a double vessel target system, tungsten degrader, and silicon detectors. The whole target system used in the (π^-, K^-) calibration was the same as used in the H particle production, except that the upper target vessel was filled with liquid hydrogen in the (π^-, K^-) calibration experiment instead of liquid deuterium as in the H particle production experiment, so that the hyperon stopping efficiency was calibrated under the same conditions (see below for details).

Target Vessels

As Fig. 2.12 shows, the target was a double vessel target system. The lower vessel was designated the LH2 vessel, and the upper vessel was designated the LD2 vessel. In the H particle production run, the LH2 vessel was filled with liquid hydrogen and the LD2 vessel was filled with liquid deuterium. However, in the (π^-, K^-) calibration run, both vessels were filled with liquid hydrogen. The Σ^-'s were produced in the lower LH2 vessel through $\pi^- + p \rightarrow \Sigma^- + K^-$, and the $(\Sigma^-, p)_{atom}$'s were formed in the upper LD2 vessel through Σ^-'s captured on hydrogen; then the neutrons were produced through the reaction $(\Sigma^-, p)_{atom} \rightarrow n + \Lambda$. Both target vessels were made of aluminum and installed inside a vacuum tight aluminum container. Because of the short lifetime of the Σ^- ($\tau = (1.479 \pm 0.011) \times 10^{-10}$ s), the thickness of the aluminum walls between the two target vessels was minimized, and the beam height was set as close as possible to the top of the LH2 vessel, in order to optimize the fraction of Σ^-'s captured on hydrogen before they decayed during flight or stopped in other materials. There were 20 rows of detectors (the tungsten degraders and the silicon detectors) installed in the vacuum at the

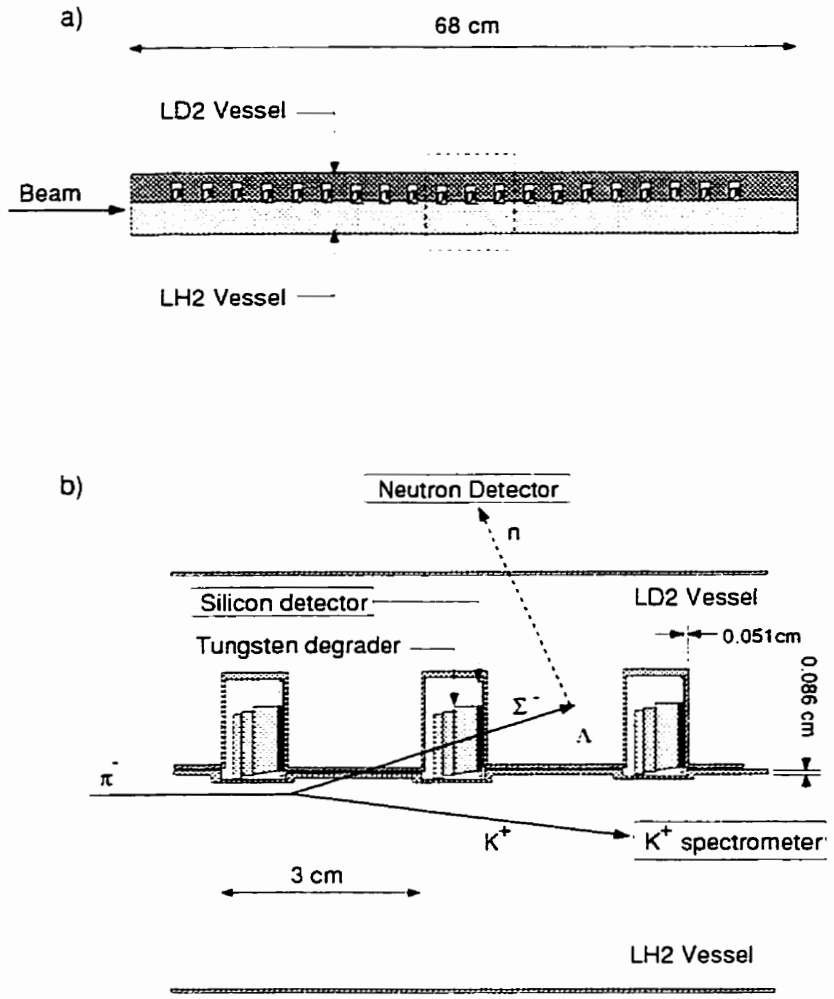

Figure 2.12: a) Target system of E813. b) Close-up view of target cells.

boundary between the upper target vessel and the lower target vessel, extending over the width of the target. As shown in Fig. 2.12, the detector rows divided the target into units. A unit was called a target cell. Each cell was 3 cm long in the z-direction. The total length of the target vessels was 68.5 cm. The boundary between the two target vessels was machined to the shape as shown in Fig. 2.13, so that it could match with the projected beam waist at around $z = -20$ cm in the H coordinate system. Fig. 2.14 gives a 3-dimensional view of the E813 target.

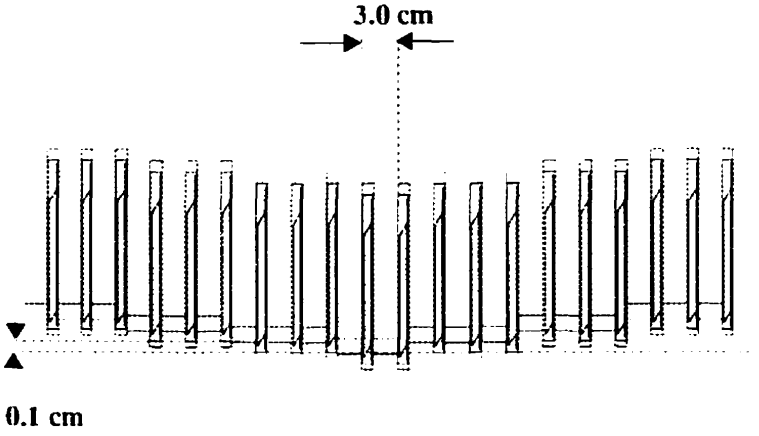

Figure 2.13: Boundary between the lower target and the upper target, arranged to match with the projected beam waist. Note the difference in horizontal and vertical scales in this figure.

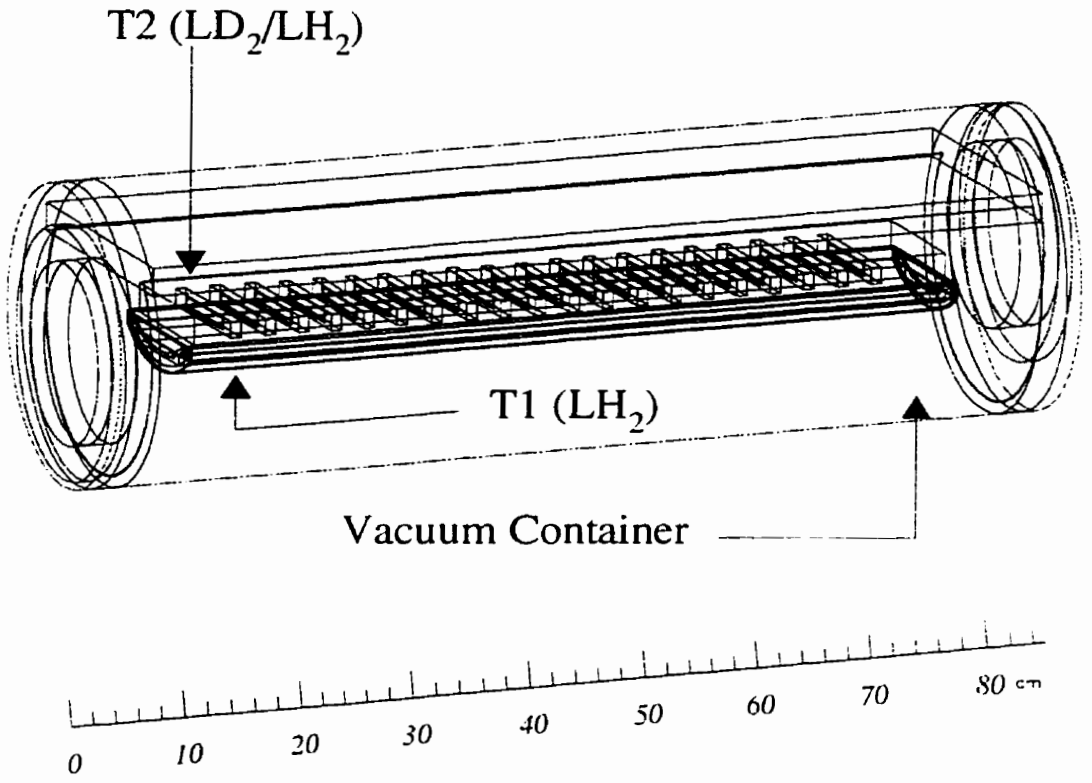

Figure 2.14: The E813 target. The upper target (T2) was filled with liquid deuterium (LD2) in the H particle production experiment, while filled with liquid hydrogen (LH2) in the present (π^-, K^-) calibration experiment.

Tungsten Degrader

A tungsten wedge was installed in every target cell between the two target vessels to slow the Ξ^-'s travelling from the lower vessel to the upper vessel in the H particle production experiment, so that a maximum fraction of Ξ^-'s would stop in the upper deuterium target to form $(\Xi^-, d)_{atom}$'s. In the present calibration experiment, Σ^-'s passed through the same tungsten wedge, and a fraction of them stopped in the upper target vessel and were captured by hydrogen to form $(\Sigma^-, p)_{atom}$'s. The eleven slabs with a total thickness of 0.29 cm were machined from pure tungsten (density of 19.3 g/cm^3), while the angled degrader with thickness of 0.30 cm was machined from hevimet, a tungsten alloy (90% W, 7.5% Ni, 2.5% Cu) with a density of 18.0 g/cm^3. These added up to a total of 0.59 cm thick tungsten degrader (see Fig. 2.12 for geometrical details).

Silicon Detectors

One of the main objectives of the (π, K^-) calibration experiment was to study the hyperon stopping efficiency; therefore, those Σ^-'s which had the highest probability to stop in the upper liquid hydrogen target to form the $(\Sigma^-, p)_{atom}$'s were tagged. This was done by the silicon detectors which were attached to the downstream face of each tungsten degrader, seen in Fig. 2.12. The 0.02 cm thick diffused-junction silicon detectors were mounted on conductive cryogenic epoxy ceramic frames, and placed in vacuum at $\sim 20°K$. As Fig. 2.15 shows, each silicon detector had two wafers, and each wafer contained four 1×1 cm^2 active area pads. As there were 20 silicon detectors along the target in the z-direction, and each silicon detector had two silicon wafers and each wafer had four silicon pads, there were a total of 160 silicon pads. Fig. 2.16 shows a Monte Carlo simulation [111] of the efficiencies for Σ^- stopping in the different materials. As seen from the diagram, the Σ^- which deposited about $1.25 - 2.25$ MeV energy in the silicon detector should have the highest probability to stop in the upper hydrogen target.

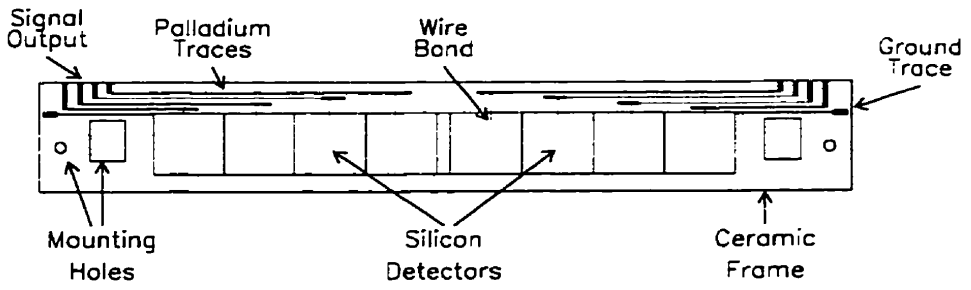

Figure 2.15: Silicon detector and ceramic frame viewed from the downstream end of the target region.

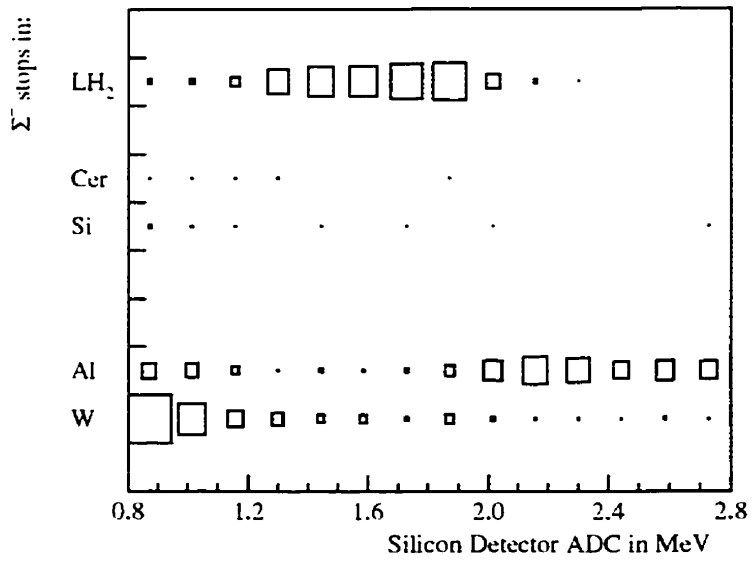

Figure 2.16: A 2-dimensional plot of the Monte Carlo simulation for Σ^- stopping efficiency. The x axis is the energy deposited in the silicon detectors, and the y axis is material in which the Σ^- stops. "Cer" represents ceramic.

2.5 ND Sector

A neutron detector array was located on both the left and the right sides of the target to measure the time-of-flight of neutrons produced from the reaction $(\Sigma^-, p)_{atom} \rightarrow \Lambda + n$. As Fig. 2.17 shows, there were a total of 6 layers of scintillator on each side of the target.

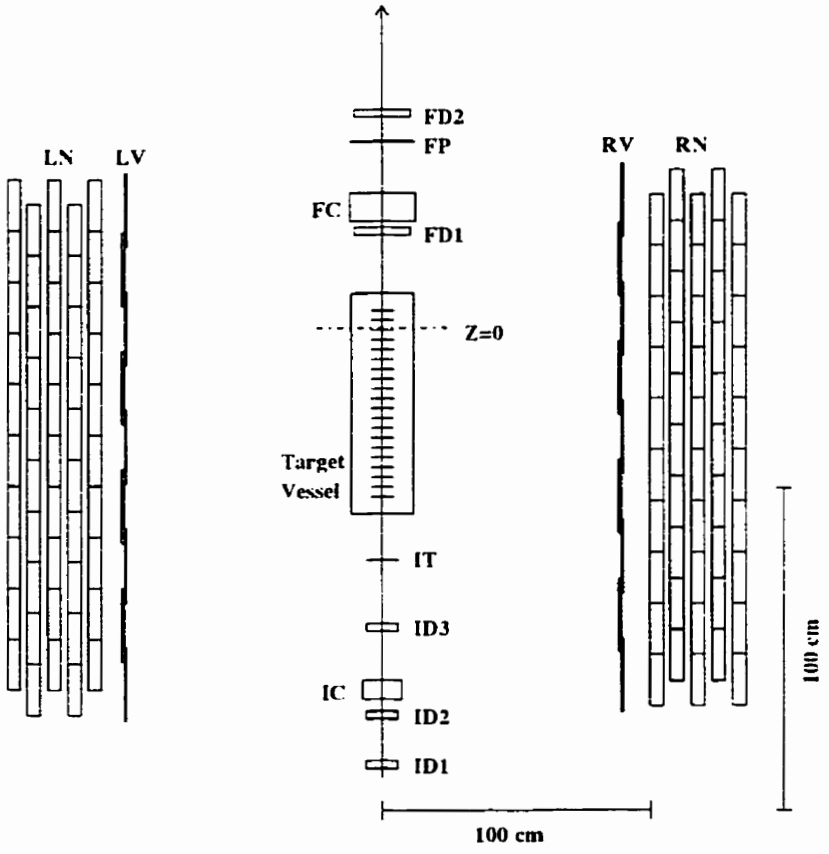

Figure 2.17: Top view of the neutron detectors. LV and RV are charged particle vetoes; LN and RN are the neutron detector arrays.

The first layers indicated as LV and RV were layers of thin scintillator, working as charged particle vetoes. Each veto layer consisted of 9 pieces of BC408 scintillator with dimensions of 20.3 cm wide, 0.95 cm thick, and 182.9 cm high. They were staggered with 0.94 cm overlap. Each element of LV and RV was coupled to two RCA 8575 PMTs at both ends via adiabatic light guides.

Layer	layer Center(cm)			bar dimensions (cm)			Z spacing	light speed
	X	Y	Z	DX	DY	DZ	(cm)	(cm/ns)
RV	-90.32	0.0	-35.09	0.95	182.88	20.3	18.42	15.62
RN1	-100.52	0.0	-38.97	5.08	182.88	15.24	15.88	14.90
RN2	-108.12	0.0	-31.35	5.08	182.88	15.24	15.88	14.90
RN3	-115.92	0.0	-38.97	5.08	182.88	15.24	15.88	15.50
RN4	-123.82	0.0	-31.35	5.08	182.88	15.24	15.88	15.50
RN5	-131.52	0.0	-38.97	5.08	182.88	15.24	15.88	15.31
LV	90.34	0.0	-38.32	0.95	182.88	20.3	18.42	15.63
LN1	100.44	0.0	-34.50	5.08	182.88	15.24	15.88	14.90
LN2	108.14	0.0	-42.12	5.08	182.88	15.24	15.88	14.90
LN3	115.84	0.0	-34.50	5.08	182.88	15.24	15.88	15.50
LN4	123.84	0.0	-42.12	5.08	182.88	15.24	15.88	15.50
LN5	131.44	0.0	-34.50	5.08	182.88	15.24	15.88	15.67

Table 2.5: Description of the geometrical structure of the neutron detectors. X, Y, and Z are the center positions for each layer. DX, DY, and DZ are the dimensions of each log. The Z spacing is the separation between the centers of the logs within a layer.

The rest of the layers indicated as LN's and RN's consisted of a total of 100 BC408 scintillator neutron bars with 10 bars in each layer. The dimensions of each neutron bar were 15.24 cm wide, 5.08 cm thick, and 182.88 cm high. Each neutron bar was mounted with an Amperex 2262 PMT via trapezoidal light guides, one at each end. The pulses from each PMT were discriminated by a CFD (Phillips 715) and read into a Fastbus Kinetics F432 TDC to give the timing information. The threshold of the discriminator voltage was 50 mV, which corresponds to 0.25

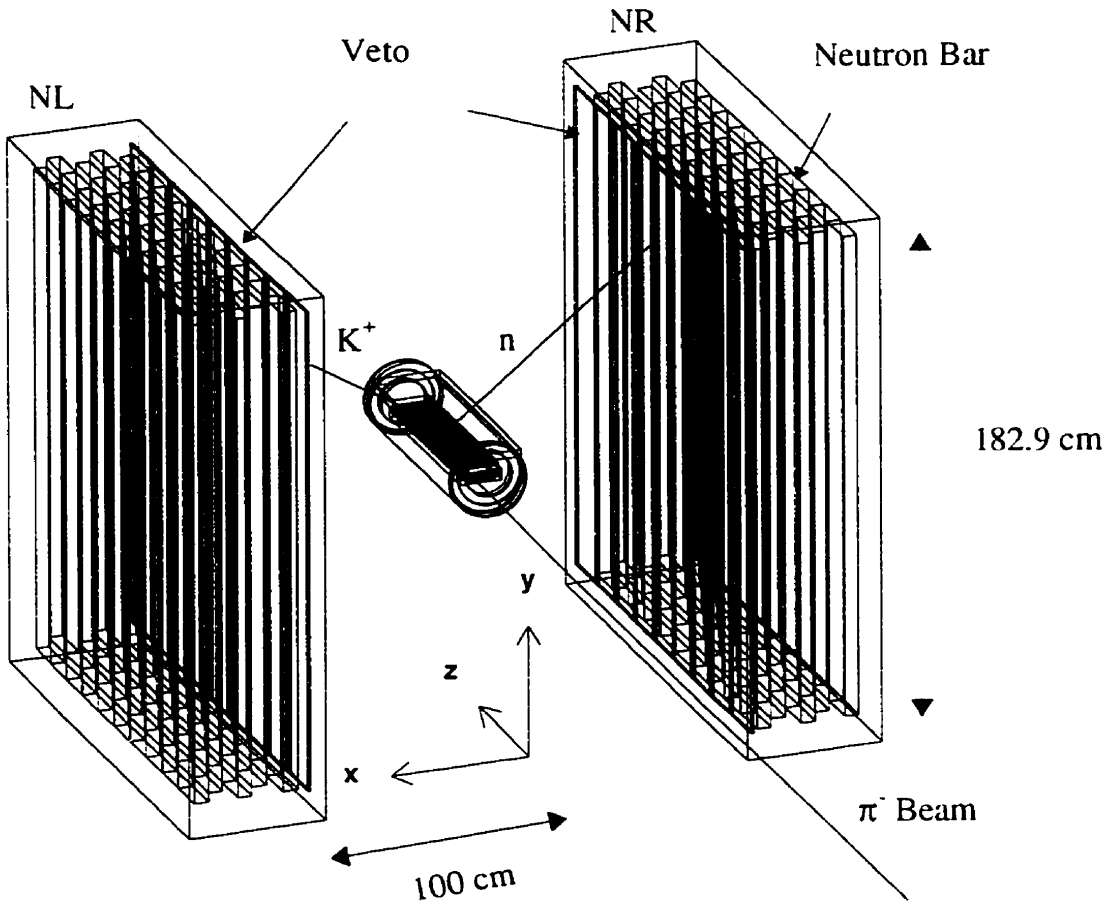

Figure 2.18: A 3-dimensional plot of the neutron detectors.

MeV_{ee} light output (1 MeV_{ee} is the equivalent light output for an electron to deposit 1 MeV of energy). The relative y position on the neutron bar, where a neutron hit, could be calculated from the time difference registered by PMTs on both ends of the neutron bar, while x and z positions of hits were estimated to be the center of the neutron bar which was hit. The mean time of the TDC's from the PMT's at both ends of a neutron bar combined with IT information was used for the neutron time-of-flight measurement. Table 2.5 gives more detailed geometrical information about the neutron detectors. The neutron detectors covered an average solid angle about $0.21 \times 4\pi$ sr in total. Fig. 2.18 gives a 3-dimensional view of the neutron detectors.

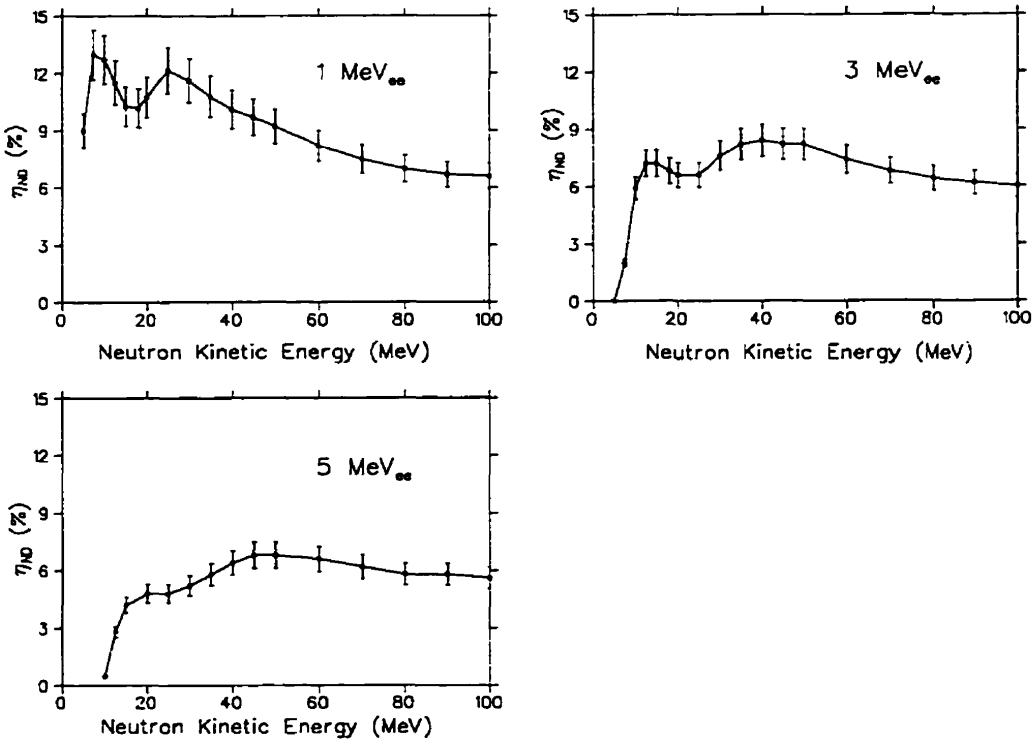

Figure 2.19: Monte Carlo simulation of the neutron detection efficiency. $\eta_{ND} = \Omega \times \varepsilon_{ND}$, where Ω is the total solid angle of the neutron detectors, and ε_{ND} is the neutron detector efficiency. The three plots correspond to the light output thresholds of 1 MeV_{ee}, 3 MeV_{ee}, and 5 MeV_{ee} respectively.

The neutron detection efficiency η_{ND} is defined to be the neutron detector's solid angle Ω multiplied by the neutron detector efficiency ε_{ND}: $\eta_{ND} = \Omega \times \varepsilon_{ND}$. This was simulated by the DEMONS Monte Carlo program[116]. The simulated efficiencies for light output thresholds (electron-equivalent energy thresholds) of 1, 3 and 5 MeV_{ee} are shown in Fig. 2.19. For different light output thresholds, the neutron detection efficiencies versus the neutron energy are different. The electron-equivalent energy is dependent on the light produced mostly by charged particles from neutron-induced inelastic reactions on ^{12}C in the scintillator, such as (n,p), (n,np), (n,α), (n,3α) and so on; it is a function of those neutron-induced charged particle energy distributions which are relative to the inelastic reactions which produced them [117]. The neutron detection efficiency is directly dependent on the cross sections of the neutron-induced reactions. Therefore with different electron-equivalent energy thresholds, the behavior of the neutron detection efficiency is different.

2.6 Data Acquisition

The triggers are predetermined conditions used to select the events of interest while rejecting uninteresting background events. If any of the trigger conditions was met, the data were processed by the data acquisition system and recorded on 8mm magnetic tape for off-line analysis. The trigger logic and data acquisition are described in more detail below.

2.6.1 Triggers

There were two levels of triggers used in the experiment. The first level trigger was developed in hardware, by sending discriminated signals from various detectors to the electronics modules and performing logic combinations with these signals. The second level trigger was formed in software.

First Level Triggers

The first level triggers were constructed with discriminated signals. The discriminated signals, from scintillator hodoscopes (IT, FP, and BP), the Čerenkov detectors (IC, FC and BC), and silicon detectors (SI), were sent to Nuclear Instrument Modules (NIM) where the logic operations were applied. If one or more than one combination of these signals satisfied certain conditions, the corresponding triggers were formed. Table 2.6 describes the conventions used in the trigger definitions in Table 2.7, and Table 2.7 summarizes the trigger logic. In Table 2.7, IC, FC, and BC are defined as the discriminated signals of the analog sum of all PMTs viewing the aerogel radiators; IT, BP, and SI are the ".OR." of their elements. Because of data acquisition system dead time, the trigger rate had to be reduced by a prescale factor before events were recorded on tape. The choice of the prescale factors were dependent on how important a given trigger was, and how busy the data acquisition system was for a typical primary beam spill from

the AGS. For example, in the (π^-, K^-) calibration, the prescale factor of the PIKS trigger was set to be 1 because it was most important, and the prescale factor of the PIBEAM was set to be 1×10^6 as it was less important, i.e. every event satisfying the PIKS trigger was recorded on tape while only one in 10^6 of the events satisfying the PIBEAM trigger was recorded. The trigger prescale factor combinations are listed in Table 2.7. The actual fraction of triggers written to the tape was the data acquisition live-time, which was about 85%–90%, divided by the prescale factor. The PIKS trigger was a subset of the PIK trigger with one of the silicon detector pads being fired. In other words, a fraction of PIK triggers would also become PIKS triggers whenever any of the silicon detector pads had signals which passed a threshold of $\sim$ 50 mV. The PIKS trigger was the most efficient trigger for identifying the creation of Σ^-'s through the reaction $\pi^- + p \rightarrow \Sigma^- + K^-$ with Σ^-'s stopping in the upper target.

Symbols	definitions
"."	.AND.
"+"	.OR.
$\overline{\mathrm{D}}$	.NOT.D
BEAM	FP13+FP14+FP15+FP16
NBEAM	FP1+$\cdots$+FP12
BT_a	BT17+$\cdots$+BT24
BT_b	BT28

Table 2.6: Conventions used in the trigger definitions in Table 2.7. A detector's name with a digital number α represents the α'th element of this detector. For example, FP13 is the 13th element of FP.

trigger	definition	typical value	
		counts/spill	prescale factor
PIBEAM	IT· IC	3.7×10^6	1×10^6
KBEAM	IT · $\overline{\text{IC}}$	6.3×10^3	1×10^3
KSCAT	NBEAM · $\overline{\text{BEAM}}$ · BP · $\overline{(\text{FC} + \text{BC})}$	-	-
PISCAT	NBEAM · $\overline{\text{BEAM}}$ · BP · (FC + BC)	-	-
PIK	PIBEAM · KSCAT	3.4×10^3	2×10^2
PIPI	PIBEAM · PISCAT	3.8×10^3	2×10^3
ITBT	IT · (BT_a + BT_b)	6.6×10^3	4×10^3
PIKS	PIK · SI	160	1

Table 2.7: Definitions of triggers. The counts/spill and prescale factors are the typical values with 1.2×10^{12} primary protons/spill on the production target. The conventions used in the trigger definitions are described in Table 2.6. PIBEAM is a trigger to identify the incoming π^-'s from the beamline; KBEAM is a trigger to identigy the incoming K^-'s from the beamline; KSCAT is a trigger to identify the scattering K^-'s; PISCAT is a trigger to identify the scattering π^-'s; PIK is a trigger to identify the incoming π^- and the scattering K^- events; PIPI is a trigger to identify the incoming π^- and the scattering π^- events; ITBT is a trigger to identify the events which the incoming particles hit IT and the scattering particles hit BT; PIKS is a trigger to identify the Σ^-'s produced from the reaction $\pi^- + p \to \Sigma^- + K^-$ that passed through the silicon detectors.

Second Level Trigger

The second level trigger was an online software trigger. When a π^- beam was delivered to the lower hydrogen target to produce Σ^-'s through the $\pi^- + p \rightarrow \Sigma^- + K^-$ reaction, there was also $\pi^- + p \rightarrow \pi^- + p$ scattering taking place with the knock-on protons traversing the spectrometer. Most of the events which satisfied the PIK trigger were actually (π^-, p) scattering events. In order to further reduce the trigger rate due to this process, we rejected the proton events by using a second level trigger. The second level trigger was formed by an online computer discriminating the kaons from protons by difference in time-of-flight for a certain momentum. The bottom half of the FD3 y-y' planes were segmented to give 16-bit information on vertical hit positions within the magnet, and y positions of the particle after the magnet were roughly estimated by which BT element was fired, as BT elements were arranged horizontally. Certain combinations of vertical position information from both FD3 and BT indicated the momentum of the particle and the path length. For the (π^-, K^-) calibration run, the typical momentum of an outgoing K^- was about 0.85 GeV/c and the path length was approximately 800 cm. Therefore, with a given combination of vertical positions from FD3 and BT (indicating the same momentum and path length), the typical time-of-flight separation between kaons and protons was about 5 nsec. As a result, knock-on protons were discriminated from kaons by applying a cut on the time-of-flight of the particles for a given vertical position combination. The time-of-flight was based on IT and BT timing information by using the LeCroy FERA/FERET TDCs with 0.050 nsec resolution. The FERA/FERET TDC system was chosen because of its fast digitization time. It took about 150 μsec to finish digitization of one event while Fastbus TDC (in which all other detector signals were digitized) needed about 600 μsec. This allowed FERA/FERET to have enough time to make decisions and to pass the information back to the data acquisition system for the event readout or rejection. With the second level trigger, about 78% of

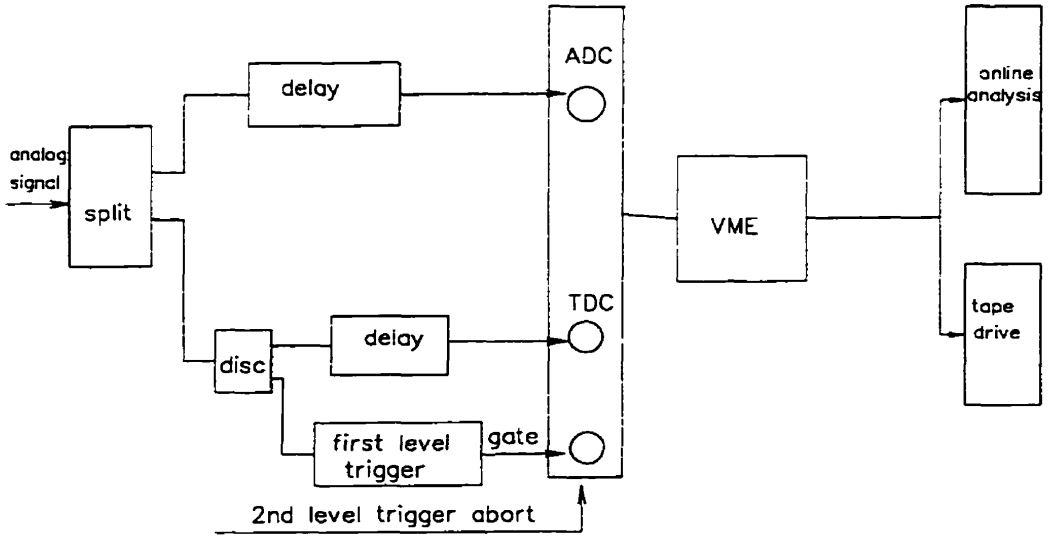

Figure 2.20: Logic diagram of the data acquisition process.

unwanted protons were rejected. The live-time of the data acquisition was about 85%–90% during the whole period of the (π^-, K^-) run.

2.6.2 Data Acquisition Process

Fig. 2.20 shows the data acquisition process for a typical analog signal. The analog signals were split into two. One went to a Fastbus ADC for analog to digital conversion, the other went to a discriminator then to a Fastbus TDC for the time to digital conversion, while the master trigger blocked further events coming through before the ADCs and TDCs completed their digitization and readout. During the time when first level trigger conditions were being tested, all the detector signals were appropriately delayed to allow the first level trigger decision to be made. If not aborted by the second level trigger, the digitization process was completed, and all the ADCs, TDCs and trigger state information were stored in

a VME input/out buffer. One of the VME-based microprocessors, FIC1, would then pass the data from the buffer to another VME-based microprocessor, FIC2, where the information was reformatted. Once the raw event buffers were built, the data was written to an Exabyte 8mm tape drive, and in the meantime a sample of data was passed to a VAX computer through a dual-ported Q-bus/VME memory for on-line analysis. The sample of data would also be transferred from the host computer to other workstations linked through Ethernet. The on-line data were monitored and analyzed by a software package called the Interactive Data Analyzer (IDA). A detailed description of analysis package, IDA, can be found in ref. [118].

In order to monitor and change the high voltages during the data collection, a high voltage control program, called HVOLT was running all the time to control the LeCroy 1440 high voltage mainframes via a terminal line (LTA3:) connected to a serial CAMAC crate controller (KS 3989), which interfaced to a daisy-chain of 1440 mainframes via an interface module (LRS 2132). Each 1440 mainframe contained a memory of "demand" values for its 256 channels. The program could read and write demand values, as well as read the "actual" or "measured" values for each channel. The high voltages could be changed according to the needs, and were monitored on-line.

During the data collection, a floor check was carried out every eight hours to make sure the gas bottles were not empty and all the electronics and other instruments were working properly.

There were several different data sets collected before and after the experiment, in order to calibrate the detectors, such as the timing detectors, the silicon detectors, and the neutron detectors. Some details are discussed in chapter three.

Chapter 3

Data Analysis

In this chapter, the data analysis procedure is outlined. First, calibrations of detectors and time-of-flight measurements are discussed. Second, Σ^-'s produced from the $\pi^- + p \rightarrow \Sigma^- + K^+$ reaction are identified, and a subset of data is created by only selecting useful events from the raw data files, so that the reduced data can be a manageable size to be put on disk for analysis. Third, tags are applied to Σ^-'s which have the highest probability to form $(\Sigma^-, p)_{atom}$'s, and tighter cuts are applied to reject background and to ensure high efficiency of $(\Sigma^-, p)_{atom}$ formation. Finally, the neutron spectrum, expected to contain a 43.5 MeV monoenergetic neutron peak in coincidence with $(\Sigma^-, p)_{atom}$ formation, is discussed.

3.1 Calibration

Certain important detectors and time-of-flight measurements were calibrated, so that the relevant quantities constructed from them could be used for analysis. These processes are discussed in the following sections.

3.1.1 Time-of-flight Calibration

There were four time-of-flight (TOF) measurements in this experiment. The first two were in the beam line sector; one was from MP to MT with 0.1 m straight path length, and the other was from MT to IT with an approximately 14.3 m curved path length, as shown in Fig. 2.4. The third was between IT and BT in the 48D48 spectrometer, with about an 8.7 m curved flight path (shown in Fig. 3.1). The fourth was between the target and the neutron detectors (shown in Fig. 2.17). During the 5 weeks of data collection, the time-of-flight offsets in the 48D48 spectrometer shifted several times due to bad cable connections and grounding or some other as yet unexplained reasons. The time-of-flight calibrations were therefore extremely important and needed to be done on a run by run basis. Beam particle π^-'s were used to normalize the time-of-flight (TOF) information in the beam line (MT-IT and MP-MT); while protons, which were the dominant component of the scattered particles, were used to normalize the TOF information in the 48D48 spectrometer (IT-BT).

Time Reference IT Calibration

The timing information of all detectors was recorded in TDC's as the number of channels between a "start" signal and a "stop" signal. As described in chapter 2, the four element scintillator detector IT served as the timing start. It provided a time reference for all the time-of-flight measurements and other measurements. The four IT elements were calibrated first, so that each of them gave the same start time if they were hit at the same time. Because the IT elements were oriented vertically, and the BT elements behind the spectrometer were oriented horizontally, one of the most favored BT elements, where most of scattered particles passed through, was chosen as a reference for the IT calibration. In this case, the 18^{th} BT element was chosen. By using the $\pi^- + p \rightarrow \pi^- + p$ scattering events with protons passing through the 48D48 spectrometer, as shown in Fig.

3.1, the measured TOF was calibrated against the predicted TOF calculated from the measured path length and momentum, according to:

$$\Delta TOF_{IT^i-BT^{18}} = TOF_{IT^i-BT^{18}}(mea) - TOF_{IT^i-BT^{18}}(pre). \tag{3.1}$$

where $i = 1.....4$. $TOF_{IT^i-BT^{18}}(mea)$ was the measured time-of-flight of the π^- from the i^{th} element of IT to the reaction vertex of $\pi^- + p \rightarrow \pi^- + p$ plus the TOF of the scattered proton from the vertex to the 18^{th} element of BT, and $TOF_{IT^i-BT^{18}}(pre)$ was the calculated time-of-flight from the i^{th} element of IT to the 18^{th} element of BT for the same event by using the measured momentum and path length. Fig. 3.2 shows the difference between the measured and predicted time-of-flight from each IT element to the 18^{th} element of BT before and after IT calibration. An offset was added to each IT element so that each segment of the histogram after calibration was aligned at zero.

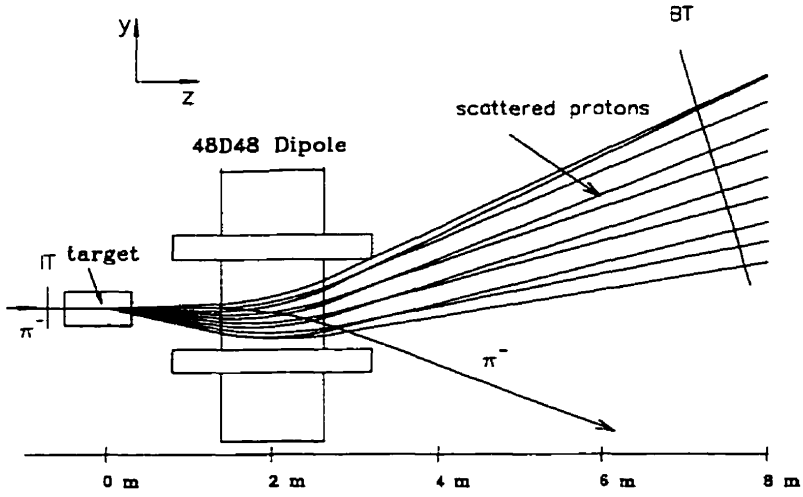

Figure 3.1: Reaction $\pi^- + p \rightarrow \pi^- + p$ used for IT and BT timing calibration.

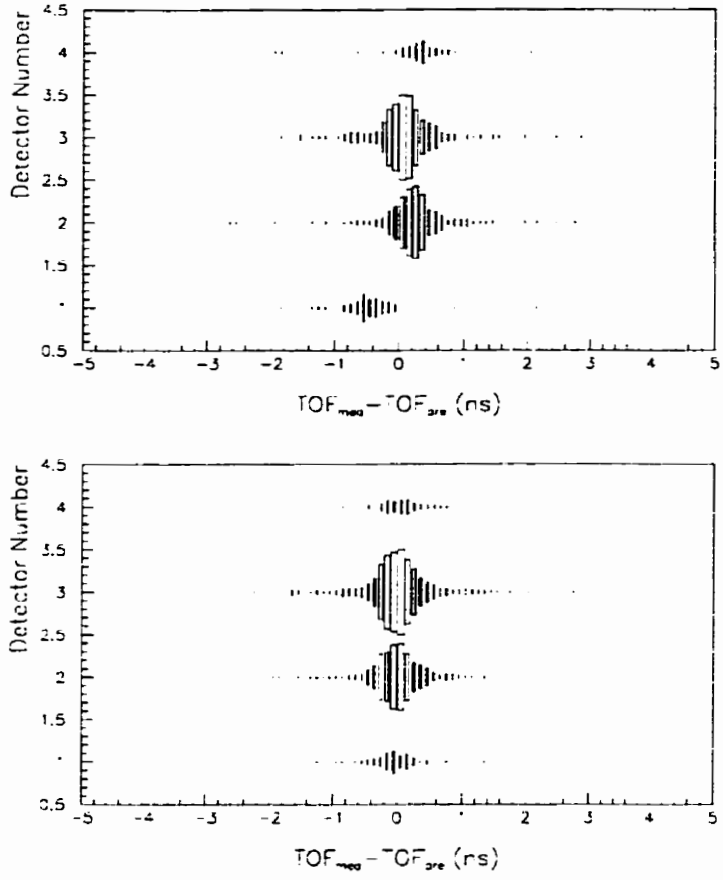

Figure 3.2: Histograms used for IT timing calibration. Shown are the IT detector number versus the differences between measured and predicted TOF for the incident π^-'s and the scattered protons from each IT element to the 18^{th} element of BT. The upper plot is the spectrum before IT calibration, and the lower plot is after IT calibration. Individual timing offsets have been added to the ΔTOF value of each IT element in the calibration to align all four segments of the histogram at $TOF_{mea} - TOF_{pre} = 0$ ns.

Beam Line TOF Calibrations

In the beam line sector, the time-of-flight from MT to IT was used to identify the beam particles by combining it with the beam momentum measurement. After the time of IT was calibrated, a histogram was generated with the time-of-flight from each element of MT to IT. As Fig. 2.4 shows, the distance from MT to IT is approximately 14.3 m. For 1.4 GeV/c π^- beam particles, the timing offsets of each MT element were determined so that π^-'s travelling through approximately 14.3 m distance from each MT element to IT had the same relative time-of-flight. Fig. 3.3 is a histogram used for the MT timing calibration.

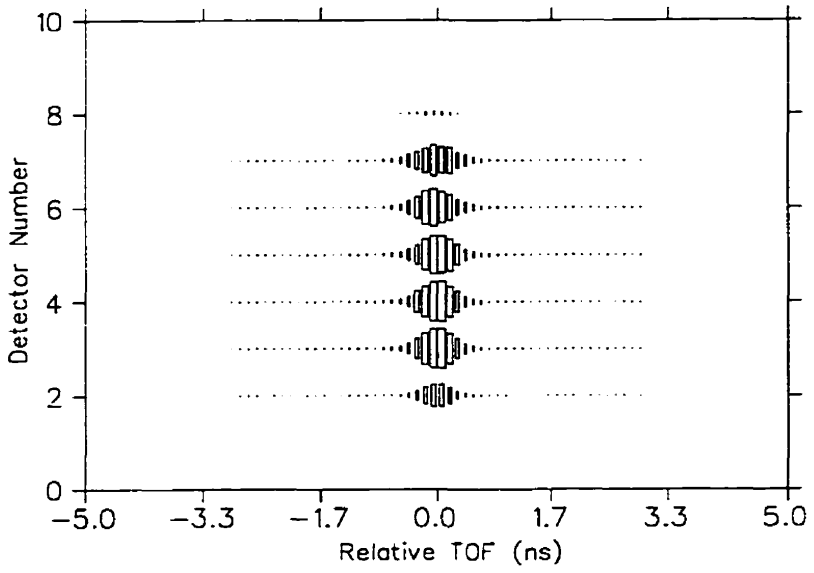

Figure 3.3: Histogram illustrating the MT timing calibration. Shown are the MT detector numbers versus relative time-of-flight of π^-'s from each MT element to IT. Individual timing offsets have been added to each MT element so that 1.4 GeV/c π^- beam particles travelling from each MT element to IT have the same relative time-of-flight. Relatively few particles passed through MT detector elements 1, 8, and 9.

As mentioned earlier, MP was used to measure the beam particle x position

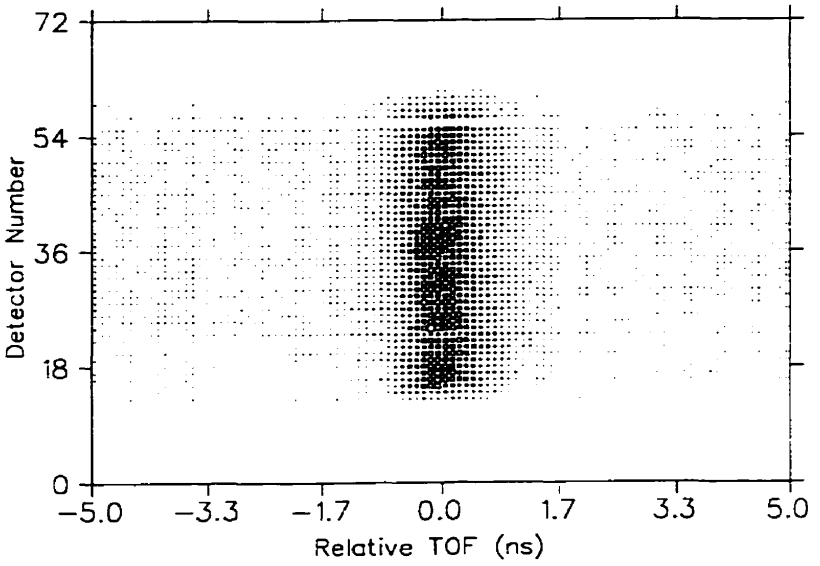

Figure 3.4: Histogram illustrating the MP timing calibration. Shown are the MP detector numbers versus relative TOF of π^-'s from each MP element to MT. Individual timing offsets have been added to each MP element so that 1.4 GeV/c π^- beam particles travelling from each MP element to MT have the same relative time-of-flight. The missing 56th channel is due to a scintillator element having no signal output.

in the mass slit area in order to calculate the beam momentum. When multiple elements of MP were fired, however, the valid MT hits were examined first by requiring the MT to IT time-of-flight to be consistent with a 1.4 GeV/c π^- travelling through a 14.3 m distance. Then the valid MP hits, which were geometrically consistent with the valid MT hits, were determined. If multiple MP hits were valid, the best MP hit was chosen by selecting the smallest MP to MT time-of-flight. Therefore, the time-of-flight from MP to MT also needed to be calibrated. The relative locations of MP and MT are shown in Fig. 2.4 in chapter two. With a calibrated MT, a histogram was generated with time-of-flight from each MP element to MT. Fig. 3.4 is the histogram used for MP timing calibration for a single run. The timing offsets of each MP element was determined by aligning all the segments of the histogram at zero, so that 1.4 GeV/c π^- beam particles flying from each MP element to MT with a 10 cm straight path length would have the same relative time-of-flight.

Spectrometer TOF Calibration

As the time-of-flight of IT-BT in the 48D48 spectrometer was used for the secondary mass calculation in order to identify the scattered particles, the IT-BT time-of-flight calibration was very important. After IT was calibrated, the measured TOF's from IT to each BT element were calibrated against the predicted TOF's, using the same method as the IT calibration (see Fig. 3.1):

$$\Delta TOF_{IT-BT_i} = TOF_{IT-BT_i}(mea) - TOF_{IT-BT_i}(pre), \tag{3.2}$$

where $i = 1, \ldots, 40$. The predicted time-of-flight from IT to the i^{th} BT element, $TOF_{IT-BT_i}(pre)$, was calculated from the measured momentum and the flight path length, assuming the incident particles to be π^-'s and the scattered particles to be protons. Fig. 3.5 shows the time difference between the measured and predicted time-of-flight from IT to each BT element before and after the BT

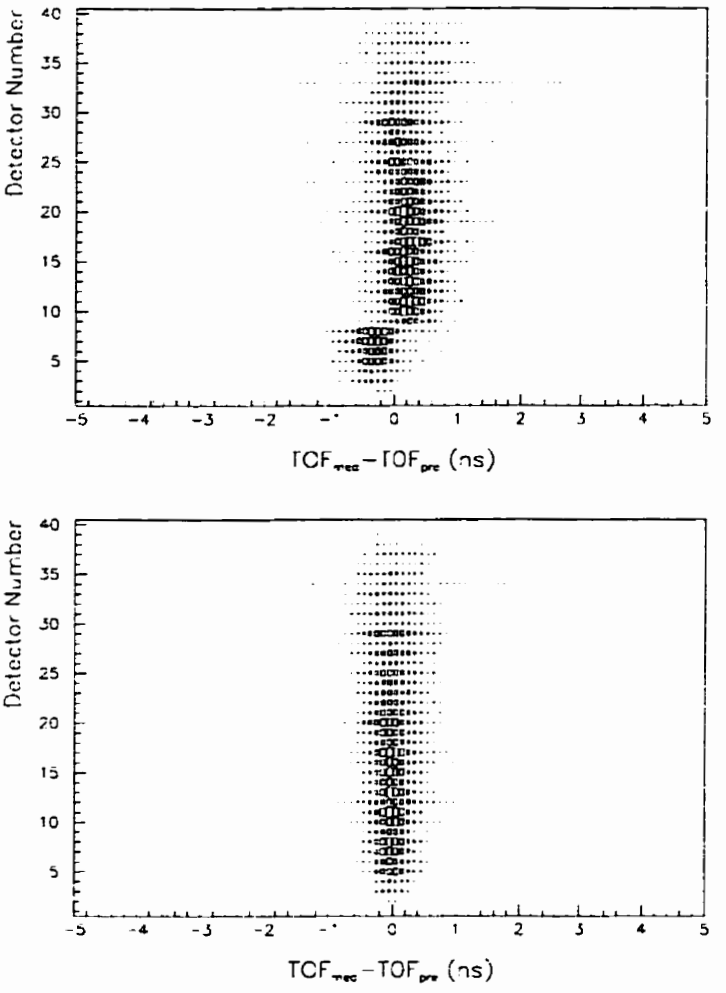

Figure 3.5: Histograms used for BT timing calibration. Shown are the BT detector numbers versus differences between measured and predicted TOF from IT to each element of BT, assuming the incoming particles to be π^-'s and the outgoing particles to be protons. The upper plot is the spectrum before BT calibration, and the lower plot is after BT calibration. An individual timing offset has been added to the ΔTOF value of each BT element in the calibration to align all 40 segments of the histogram at $TOF_{mea} - TOF_{pre} = 0$ ns.

timing calibration. Each BT element has been assigned a timing offset so that the difference between measured and predicted time-of-flight is zero after the calibration.

3.1.2 Time-of-flight Resolution

In the beamline spectrometer, the resolution of the TOF from MT to IT was obtained directly from a Gaussian distribution plus a flat background to fit the relative TOF for π^-'s, shown in Fig. 3.6. The flat curve represented the random background events. The TOF resolution for the beamline was determined by the σ of the Gaussian, found to be 0.258 ns.

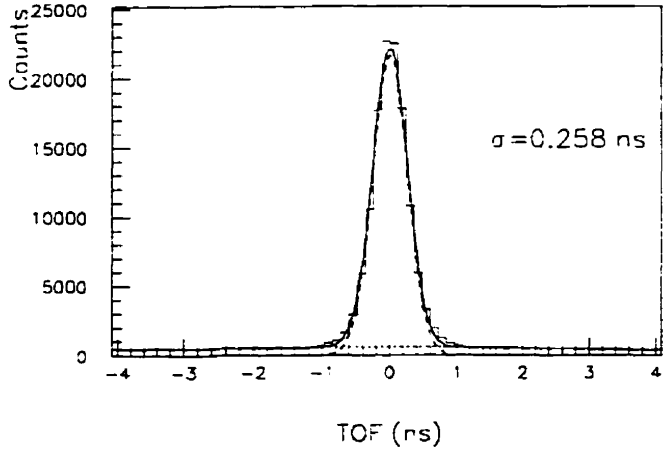

Figure 3.6: Plot of relative TOF of π^-'s from MT to IT. The solid curve is the sum of two curves, a Gaussian (the dashed curve) and a flat background (the dotted curve), that fit the spectrum. The TOF resolution of beamline was determined by the σ of the Gaussian.

In the 48D48 spectrometer, the resolution of the TOF from IT to BT was obtained from a two Gaussian fit to the TOF difference between measured and

calculated values for the $\pi^- + p \rightarrow \pi^- + p$ events, as shown in Fig. 3.7. The reason for the two Gaussian fit was to account for the large angle multiple scattering. This would smear the track reconstruction and momentum measurement, which caused a broad Gaussian background underneath the good (π^-, p) scattering events. The TOF resolution, σ, determined by the narrow Gaussian in the fit, was found to be 0.263 ns for the 48D48 spectrometer.

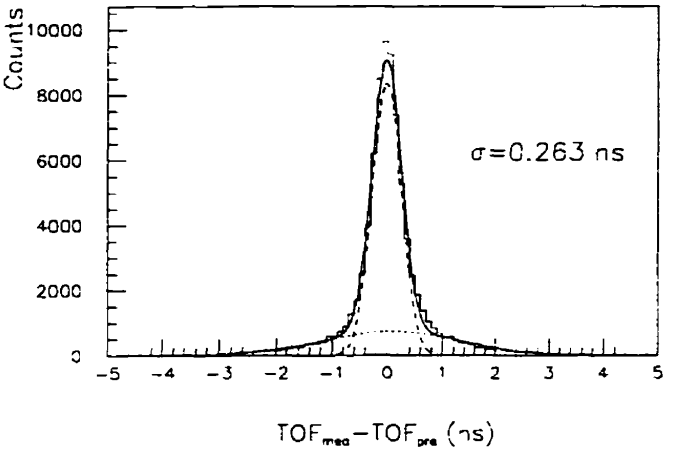

Figure 3.7: Plot of difference between measured and predicted TOF from IT to BT, assuming the incident particle to be a π^- and the scattered particle to be a free proton. The solid curve is the sum of two Gaussians shown as a dashed curve and a dotted curve. The narrow Gaussian peak corresponds to the π^-'s scattering with the free protons, and the broad Gaussian peak corresponds to background. The TOF resolution, σ, was determined by the narrow Gaussian peak.

3.1.3 Silicon Detector Calibration

In this experiment, the signature of the reaction $(\Sigma^-, p)_{atom} \rightarrow n + \Lambda$ was the detection of 43.5 MeV monoenergetic neutrons in coincidence with the formation

of $(\Sigma^-, p)_{atom}$'s. $(\Sigma^-, p)_{atom}$'s were formed by Σ^-'s being stopped and captured on a hydrogen target, and stopping Σ^-'s were tagged by their energy deposited in the silicon detectors. Therefore, the silicon detectors played an important role in the stopping Σ^-'s identification, and calibration of the silicon detector signal pulses was very important.

By measuring the pulse height in an ADC for each silicon pad, the energy deposited in the pad could be calculated from:

$$E^i_{SI} = G_{overall} \times C^j_E \times C^i_{alpha} \times (ADC^i - P^i(\omega)). \tag{3.3}$$

Where $i = 1, 2, \ldots, 160$ is the index of the silicon pads; $j = 1, 2, \ldots, 40$ is the index of the silicon wafers. E^i_{SI} is the energy deposited in the i^{th} silicon pad. $P^i(\omega)$ is the pedestal[1] position of the i^{th} pad, which is 60 Hz phase dependent. ADC^i is ADC information of the i^{th} pad. C^i_{alpha} is the energy gain calibration constant for the i^{th} silicon pad obtained from alpha source measurements made before the silicon detectors were installed in the target. C^j_E is the calibration constant for the j^{th} wafer containing the i^{th} silicon pad, calibrated by (K^-, p) elastic scattering. $G_{overall}$ is the overall gain of the silicon detectors. The calibration of the silicon detectors is to determine $P^i(\omega)$, C^j_E and $G_{overall}$.

The $P^i(\omega)$ Calibration

The pedestals of the silicon detector ADC's showed a 60 Hz phase dependence, picked up from power lines. The ADC pedestal positions were calibrated by plotting 60 Hz phase versus ADC channel for each silicon pad, without any TDC requirement. Then these plots were fit with the functions:

$$P^i(\omega) = A_0 + A_1 \cos(\omega + A_3) + A_2 \sin(\omega + A_4) \cdot \sin(2\omega + A_4). \tag{3.4}$$

[1]Pedestal: the pedestal is the counts given by the ADC (analog to digital converter) when no input signal is present. The pedestal is due to a built-in dc offset.

where A_0, ---, A_4 are fitting parameters (time independent) determined from the calibration, and ω is the 60 Hz phase. Fig. 3.8 shows a histogram used for the calibration.

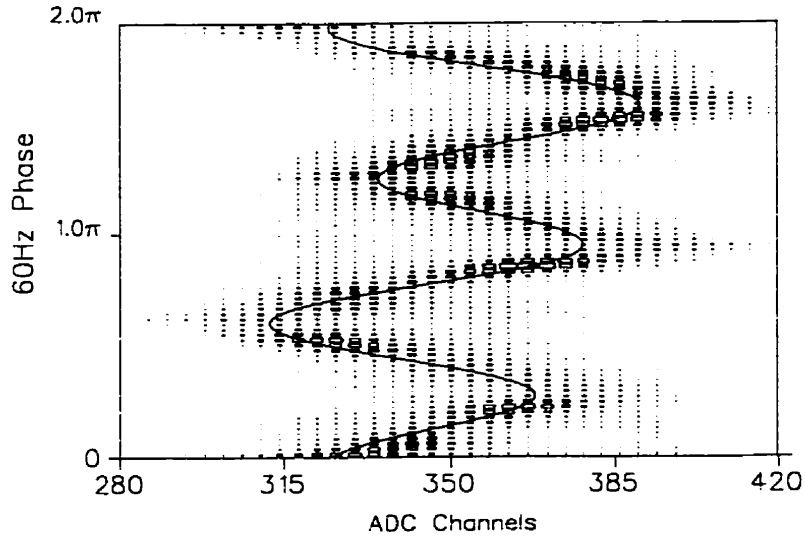

Figure 3.8: The 60 Hz phase dependence of a pedestal for a single silicon pad. The solid curve is a fit to the pedestal with the function (3.4).

Relative Gain C_E^j Calibration

$K^- + p \rightarrow K^- + p$ elastic scattering was used to calibrate C_E^j. This was a relative gain calibration for each silicon wafer. As described in chapter 2, each silicon wafer contained four 1 cm × 1 cm × 200 μm ($x \times y \times z$) silicon pads. Since the silicon pads within the same wafer had a similar thickness, they were treated as one group. As Fig. 3.9 shows, 1.8 GeV/c K^-'s interacted with the protons in the hydrogen target. Forward scattering protons struck by K^-'s then passed through the 48D48 spectrometer, while the K^-'s were scattered backward and passed through the aluminum walls between the two target vessels and then traversed the silicon detectors. The energy and angle of the scattered K^-'s were calculated

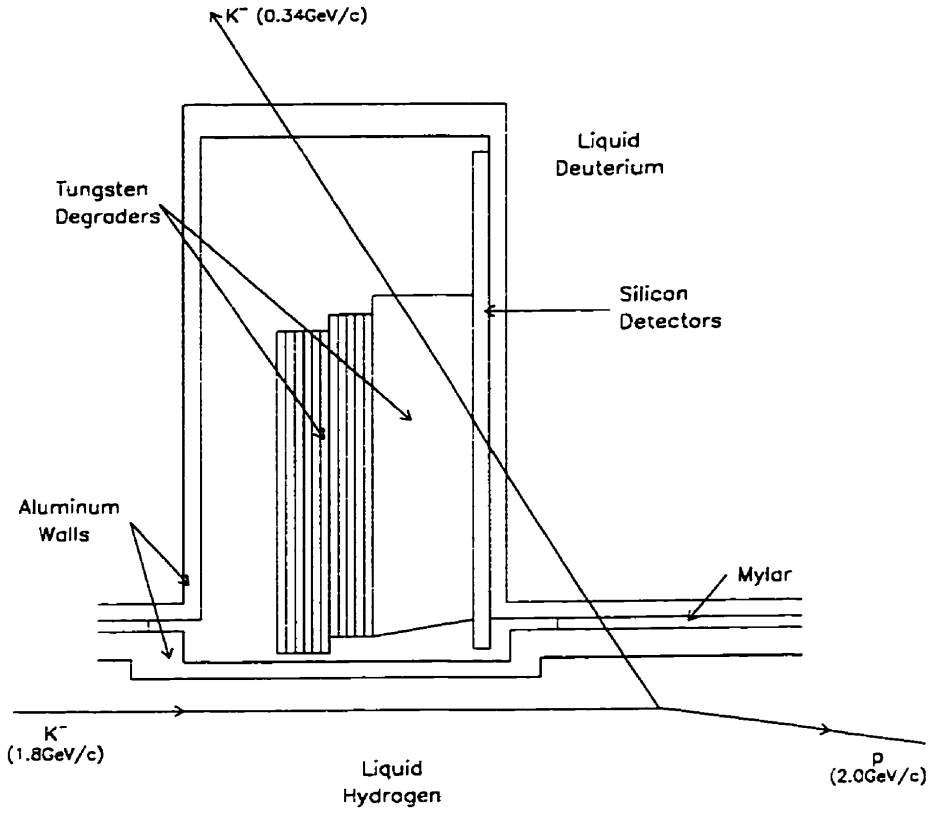

Figure 3.9: Schematic plot for a (K^-, p) elastic scattering event used for the silicon detector calibration.

by using the momentum and tracking information for the incoming K^-'s and outgoing protons. After subtracting the energy loss in the aluminum walls, the energy deposited by K^-'s in the silicon detectors was predicted. The normalized energy deposited in the silicon detectors was defined as follows:

$$E_{norm} = \frac{E_{SI}(measured)}{E_{SI}(calculated)}. \tag{3.5}$$

The normalized energy deposited in each silicon wafer was histogrammed. The C_E^J were adjusted to align the peaks of these histograms, so that the gains of the silicon wafers are relative to each other.

Overall Gain $G_{overall}$ Calibration

After the relative gain of each silicon wafer was calibrated, the overall gain of all the silicon wafers was calibrated by comparing the measured deposited energy distribution of K^-'s from elastic $K^- - p$ scattering with a Monte Carlo simulation, shown in Fig 3.10. According to a theory of the energy loss distribution for thin absorbers [119], the energy deposited by the K^-'s in the silicon detectors follows a Vavilov distribution, and this distribution shape varies strongly depending on the energy deposited. Therefore, the deposited energy distribution is a sum of many Vavilov distributions.

In order to properly model this energy deposited distribution, a measured proton angular distribution was used in the Monte Carlo simulation as there is a strong correlation between energy deposited by K^-'s and the scattering angle of the protons. In addition, the energy loss and straggling of the K^-'s as they passed through the aluminum walls were also taken into account.

To compare the measured energy deposited distribution with the Monte Carlo simulation result, there are two points that have to be kept in mind. The first is the energy range of the comparison. It is difficult to simulate the high deposited energy region due to the events in which the K^-'s stop in the silicon detectors with

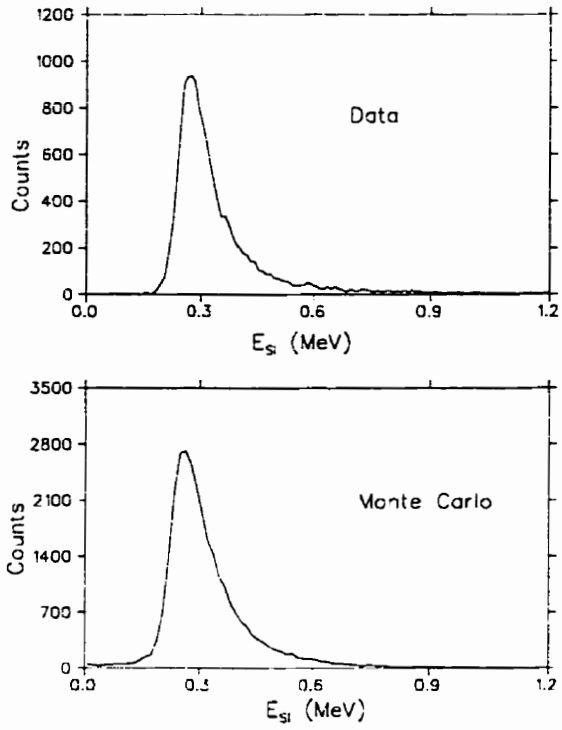

Figure 3.10: Distributions used in the silicon detector overall gain calibration. The upper plot is the distribution of measured energy deposited in the silicon detectors, and the lower plot is the Monte Carlo simulation result for the same distribution. The overall gain parameter of the silicon detectors, $G_{overall}$, and the width of the gain misalignment, σ_G, were calibrated by comparing the distributions of the data (the upper plot) to the Monte Carlo result (the lower plot).

the possibility of a large energy transfer in a single collision, which the Vavilov distribution does not fit well. On the other hand, the measurement in the very low deposited energy region is not very accurate because it is near the threshold of the detectors. Therefore, both very low and very high deposited energy regions should not be included in the comparison. The second point is the random error in the relative gain (C_E^i) calibration. This gain misalignment is assumed to follow a Gaussian distribution with an unknown width, σ_G. Therefore, each bin in the Monte Carlo distribution of energy deposited should be smeared by a Gaussian distribution with width $\sigma_E = \sigma_G \times E_{SI}$ (E_{SI} is the energy deposited) to count for the relative gain misalignments.

The least-χ^2 method was used to find the overall gain and the width of the unknown relative gain misalignment. The definition of χ^2 is:

$$\chi^2 = \sum_{i=1}^{N_B} \frac{(n_i(D) - n_i(M))^2}{n_i(D)}. \tag{3.6}$$

and the goodness-of-fit is defined as [120]:

$$Q = \frac{\Gamma(\frac{\gamma}{2}, \frac{\chi^2}{2})}{\Gamma(\frac{\gamma}{2})}. \tag{3.7}$$

where N_B is the number of bins within the range of comparison for the deposited energy, $n_i(D)$ is the number of counts in the i^{th} bin of the measured deposited energy distribution, $n_i(M)$ is the number of counts in the i^{th} bin of the Monte Carlo distribution, and $\gamma = N_B - 2$ is the number of degrees of freedom for the fit.

An iterative procedure was applied to minimize χ^2 to determine the best overall gain, $G_{overall}$, and the width of gain misalignment, σ_G. The steps are outlined below.

1. Normalizing the Monte Carlo distribution: The Monte Carlo distribution was normalized so that the total counts in the Monte Carlo distribution were the same as the total counts in the measured deposited energy distribution.

2. Determining deposited energy comparison range: Because both very low and very high energy regions should be excluded in the comparison of the data to the Monte Carlo distribution, the low and the high edges of the comparison range were determined by maximizing the goodness-of-fit, Q.

3. Determining the overall gain: With different overall gain inputs, the χ^2's were calculated by comparing each modified data distribution to the Monte Carlo distribution. Then the gain factor with the minimum χ^2 was found.

4. Finding the width of the gain misalignment: Using the gain factor which has a minimum χ^2 from step (3) to obtain a modified data distribution, and smearing the Monte Carlo distribution with different inputs of the width of the gain misalignment, σ_G, χ^2's were calculated by comparing the modified data distribution to each smeared Monte Carlo distribution. The width of the gain misalignment with the minimum χ^2 was found.

5. Testing if there is a better χ^2: Smearing the Monte Carlo distribution with the width of the gain misalignment, which has the minimum χ^2 found in step (4), was used as a new Monte Carlo distribution; the process was repeated starting from step (3) until the minimum χ^2 was obtained.

3.1.4 Neutron Detector Calibration

Another key component of the experimental apparatus is the neutron detector arrays (ND). The neutron signal pulse heights were used to reject background events in the neutron spectrum. For a hit on the i^{th} neutron detector element, the energy deposited is defined by the geometric mean of the ADC's connected to

the PMT's at both ends of the log:

$$E_{ND} = \sqrt{C_a^i(ADC_a^i - P_a^i)C_b^i(ADC_b^i - P_b^i)}. \tag{3.8}$$

The subscripts, a and b, used in equation (3.8) indicate ADC information from bottom (a) and top (b) PMTs at each end of the neutron log. P_a^i and P_b^i are ADC pedestals, and C_a^i and C_b^i are gain parameters of the i^{th} log. The motivation for

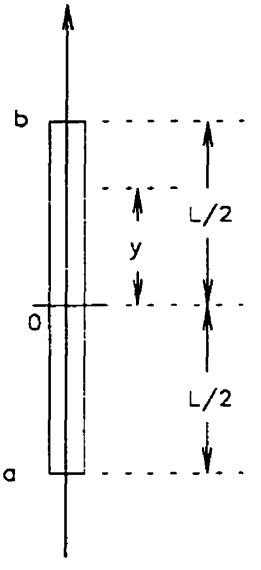

Figure 3.11: Scintillator log of length L with "PMT a" and "PMT b" at each end. A particle passes through it at position y.

using the geometric mean of the ADC's from the both ends of the neutron log to define the pulse height was to eliminate the hit position dependence. When a neutron passes a scintillator of length L at the position y, it knocks off the charged particles in the scintillator through elastic or inelastic scattering. Then the charged particles excite the atoms in the material and the deexcitement of atoms causes scintillation light. As shown in Fig. 3.11, the light collected by

"PMT a" is:

$$E_a \propto E_0 \exp\left(-(\frac{L}{2} + y)/l_0\right) \tag{3.9}$$

where E_0 is the light generated by the particle at the position y, and l_0 is the effective attenuation length in the scintillator. The light collected by "PMT b" is:

$$E_b \propto E_0 \exp\left(-(\frac{L}{2} - y)/l_0\right). \tag{3.10}$$

As seen from the above equations, both E_a and E_b are dependent on the hit position y. The geometric mean of E_a and E_b is:

$$\begin{aligned} E = \sqrt{E_a \cdot E_b} &\propto E_0 \sqrt{\exp\left(-(\tfrac{L}{2} + y)/l_0\right) \cdot \exp\left(-(\tfrac{L}{2} - y)/l_0\right)} \\ &= E_0 \sqrt{\exp\left(-\tfrac{L}{l_0}\right)} \end{aligned} \tag{3.11}$$

which is independent of y. Therefore, the geometric mean eliminates the position dependence.

The TDC information from the neutron detectors can be used to measure the time-of-flight and to determine the y position of the hit in the neutron detectors. If a particle hits the i^{th} neutron log, the time-of-arrival is defined as:

$$T^i_{ND} = \alpha \cdot \frac{TDC^i_a + TDC^i_b}{2} - T^i_0 - T_{(L \text{ or } R)}. \tag{3.12}$$

where $\alpha = 0.025$ ns is the conversion of TDC channel index to time, T^i_0 is a calibration constant for the mean time measurement of the i^{th} log, and T_L and T_R are the overall timing offset for the left and right neutron arrays. The time-of-flight is defined as:

$$TOF_{ND} = T^i_{ND} - T_{IT} - TOF_{beam}, \tag{3.13}$$

where T_{IT} is the start time measured by the scintillator detector IT, and TOF_{beam} is the time-of-flight of the beam particles from IT to the vertex in the target, where

the reaction $\pi^- + p \rightarrow \Sigma^- + K^-$ took place. The latter can be calculated from $TOF_{beam} = \frac{z_{ver} - z_{IT}}{v_b}$, where z_{ver} and z_{IT} are the z positions of the vertex and IT counter respectively, and v_b is the velocity of the beam particle.

From TDC information of the PMTs on both ends of the neutron log, the y position where the neutron log was hit can be calculated, according to:

$$y_n = v^i_{scint} \cdot \frac{(TDC^i_a - TDC^i_b - T^i_{diff})}{2} + y_0, \tag{3.14}$$

where v^i_{scint} is the measured effective speed of light in the i^{th} log, T^i_{diff} is the calibration constant of the time difference between both ends of the log, and y_0 is the y position of the center of the neutron bar.

As seen from the above discussion, both the TDC's and the ADC's of the neutron detectors need to be calibrated in order to determine the values of the timing offsets, T^i_{diff} and T^i_0, and the gain parameters, C^i_a and C^i_b.

ND Timing Calibration

In order to calibrate the neutron detectors, two sets of cosmic ray data were collected before and after the experimental run. Figs. 3.12 and 3.13 show orthogonal views of the measurement setup. For these tests, both left and right side neutron arrays were lowered and placed on the floor. A pair of long narrow scintillation counters was placed perpendicularly across the center of the neutron detector logs, with one at the bottom and the other on top of the neutron array, to define a trigger for cosmic rays traversing all layers of the neutron array at the center of the logs. The timing difference parameters T^i_{diff} and relative time parameters T^i_0 can be calibrated by these cosmic ray events, while the overall offsets T_L and T_R can be calibrated by another data set described later.

For the cosmic ray events which traverse the neutron detectors at the centers of the logs, the time difference between the two PMTs at each end of each log

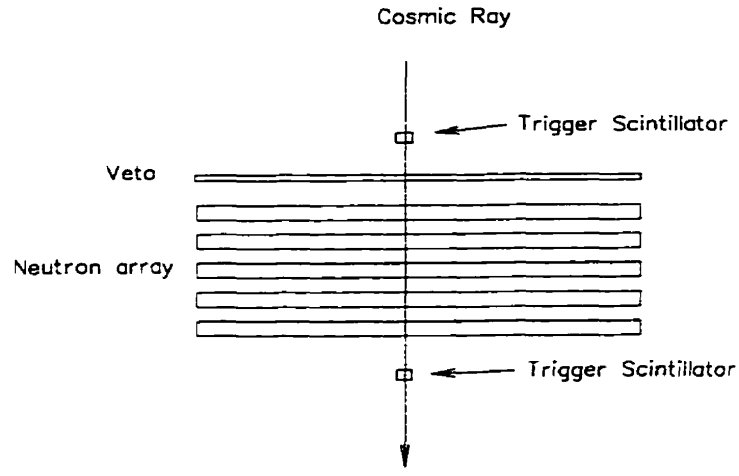

Figure 3.12: Side view of the neutron detector cosmic ray calibration setup. The neutron arrays were laid on the floor; the cosmic ray traversed all layers of the neutron array at the center of the logs.

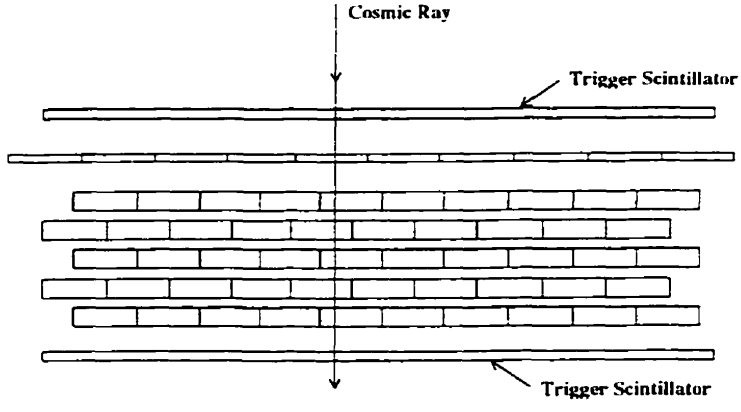

Figure 3.13: Side view of the neutron detector cosmic ray calibration setup. at 90° to Fig. 3.12.

should be zero. The time difference parameters, T^i_{diff}, were therefore adjusted so that this condition was satisfied.

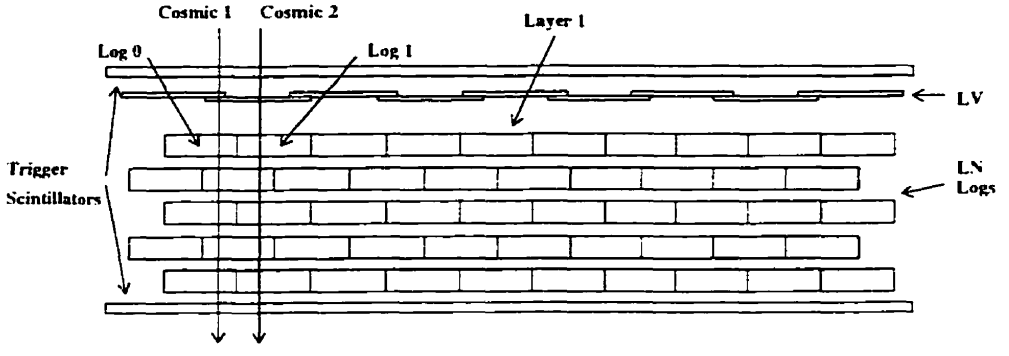

Figure 3.14: Selection of cosmic ray events used in the calibration of neutron detector relative time offsets.

In order to calibrate the relative time parameters T^i_0, the "cosmic 1" and "cosmic 2" events which had the desired orientation across the logs were selected. As shown in Fig. 3.14, "cosmic 1" passed through the same numbered log on odd layers and the neighbour log on even layers, and "cosmic 2" passed through the same numbered log on both odd and even layers. The time-of-flight for "cosmic 1" and "cosmic 2" from the first ND layer to the second ND layer should be the same. By histogramming the time-of-flight between the first and the second ND layers for "cosmic 1" and "cosmic 2" events, the relative time offset between the 0^{th} log and the 1^{st} log of the first layer was determined. The same procedure was applied to the 1^{st} log and the 2^{nd} log of the first ND layer, and so on, until all the logs on the first layer were calibrated. Once the first layer was calibrated, it was used as a reference, and the time offsets of logs in the remaining layers were calibrated by aligning the times-of-flight between the first layer and all other

layers based on the measured distance. The left and right neutron arrays were calibrated individually.

The overall time offsets, T_L and T_R, were calibrated with the K^- decay data set. With the neutron detectors placed in the normal experimental locations, the magnetic field of the 48D48 was reversed so that it bent the negative charged particles up and positive charged particles down. A 1.8 GeV/c K^- beam was delivered to the empty target. This was followed by the reactions:

$$\begin{array}{lll} K^- \rightarrow & \pi^0 + \pi^- & \\ & \downarrow & \\ & \pi^0 \rightarrow \gamma + \gamma & (\tau = (8.4 \pm 0.6) \times 10^{-17}\text{s}, R = (98.798 \pm 0.032)\%) \end{array} \tag{3.15}$$

Because the lifetime of the π^0 is $(8.4 \pm 0.6) \times 10^{-17}$ s and the branching ratio of the reaction $\pi^0 \rightarrow \gamma + \gamma$ is $(98.798 \pm 0.032)\%$, most of the π^0's decayed into 2 γ's as soon as they were produced. The vertex of $\pi^0 \rightarrow \gamma + \gamma$ was therefore assumed to be the same as the vertex of $K^- \rightarrow \pi^0 + \pi^-$. By identifying the K^- with the beamline spectrometer and identifying the outgoing π^- with the 48D48 spectrometer, the reaction $K^- \rightarrow \pi^0 + \pi^-$ was identified and its vertex was reconstructed. The time-of-flight for γ's produced from the $\pi^0 \rightarrow \gamma + \gamma$ reaction was measured by the neutron detector arrays. Because the flight length of the γ could be calculated accurately from the production vertex (assumed to be the same as the vertex of the $K^- \rightarrow \pi^0 + \pi^-$ reaction) and the hit position on the neutron detectors, the time-of-flight for the γ was also obtained using the speed of light and the flight length. The overall timing offsets, T_L and T_R, for the left and right neutron arrays were determined by assigning the difference of time-of-flight for those γ events between measurement and prediction to be zero.

Electron-equivalent Energy Calibration

The cosmic ray data described earlier can also be used to calibrate the electron-equivalent energy deposited in the neutron detectors. As Fig. 3.12 shows, only

events which traversed straight through the center of the neutron logs were selected. In this condition, the PMTs on both ends of each log should collect the same amount of light. Since cosmic rays are primarily minimum ionizing muons, at normal incidence, cosmic rays should deposit about 10.5 MeV of energy in each 5.08 cm thick neutron log. According to equation (3.8), the gain parameters of the PMTs for each neutron log can then be determined from these cosmic ray data:

$$C_a^i = \frac{10.5}{ADC_a^i - P_a^i} \quad (\text{MeV}), \qquad C_b^i = \frac{10.5}{ADC_b^i - P_b^i} \quad (\text{MeV}). \quad (3.16)$$

3.2 Identification of Σ^- Production

As described in chapter 2, the events which satisfied the PIKS trigger were the most efficiently selected data subset for the identification of Σ^-'s produced through $\pi^- + p \rightarrow \Sigma^- + K^+$ and had high probability to form $(\Sigma^-, p)_{atom}$'s. Therefore only events which satisfied the PIKS trigger were studied. Both incident π^- and scattered K^+ were identified, and their momenta were calculated from the time-of-flight and trajectory measurements. Then the Σ^-'s were identified by making cuts on the missing mass spectrum. The details are described below.

3.2.1 Beam Particle Analysis

The Čerenkov detector (IC) signal in the PIKS trigger distinguished π^-'s from other beam particles to first order, with an average $\frac{K^-}{\pi^-}$ ratio of 1.7×10^{-3}. Furthermore, particles with different mass but with the same momentum (at 1.4 GeV/c) travelling from MT to IT should have different flight times. For a fixed momentum, the lighter a particle is, the shorter its time-of-flight is. Fig. 3.15 shows the distribution of the MT-IT TOF created from the raw data[2]. In the plot, the

[2]Raw data: this is the data set without any cuts except the PIKS trigger.

bigger peak is the π^- peak, and the small bump on the longer time-of-flight side is the K^- peak because the mass of the K^- is heavier than the π^-. A cut on the relative time-of-flight was made as $-2 \leq TOF \leq 2$ ns to reject lighter and heavier particles from π^-'s.

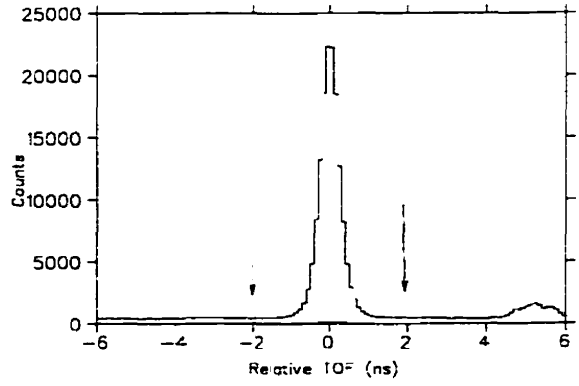

Figure 3.15: Histogram of relative time-of-flight from MT to IT, generated from the raw data. The arrows indicate the cut made in the analysis. The big peak is the π^- peak and the small bump on the longer time-of-flight side is the K^- peak.

For the incident particle, its x position was measured by MP in the mass slit area, and its x and y positions were measured by three ID chambers in the incident area. The trajectory of the beam particle before entering into the experimental target area was reconstructed by a linear least-χ^2 fit to the ID hits. The momentum of each beam particle was calculated using a second order matrix, which was determined by the code TRANSPORT [113], through dipole D3 using x information from MP and the trajectory information from the ID chambers, as shown in Fig. 2.5.

3.2.2 Scattered Particle Analysis

Trajectory and Momentum

The trajectory of each scattered particle was measured by 5 drift chambers (FD's and BD's) in the 48D48 spectrometer. The positions of hits on each drift plane were calculated from the wire positions and drift time measurements. With a maximum of two drift planes allowed to be missing, the track of the scattered particle before entering the 48D48 magnet was reconstructed by fitting a straight line to all the hits on the FD1 and FD2 chamber planes, and the track of the scattered particle after traversing the magnet was reconstructed by fitting a straight line to all the hits on the BD1 and BD2 chamber planes. The non-interacting beam particles were rejected by excluding the tracks through FD1 and FD2 at small angles and those passing through FD1 near the projected position of the beam particles. FD3 was not used in track reconstruction at this stage.

After the reconstruction of the tracks of the scattered particle in the front and back of the magnet, the x and y positions on the nominal central plane of each drift chamber were then calculated from the fitted tracks. These results were then passed to a routine called PEANUT [68] to calculate the momentum and path length of the scattered particles. The method used in PEANUT is similar to TRANSPORT [113]. The difference is that the whole region of acceptance of the 48D48 spectrometer was divided into 1440 regions because of its large acceptance. For each region, a central trajectory was calculated by integrating the equations of motion through the magnetic field, and the deviations from this central track were parameterized with a matrix. These central trajectories and matrices needed only to be calculated once at the beginning of the run, and the results were stored in a parameter file. With these matrices, any measured track could be fitted by choosing the correct matrix. In choosing the correct matrix, however, one needed to know the value of the momentum. Therefore, an iterative algorithm was used to search for the correct matrix and to calculate the momentum for a set of known x

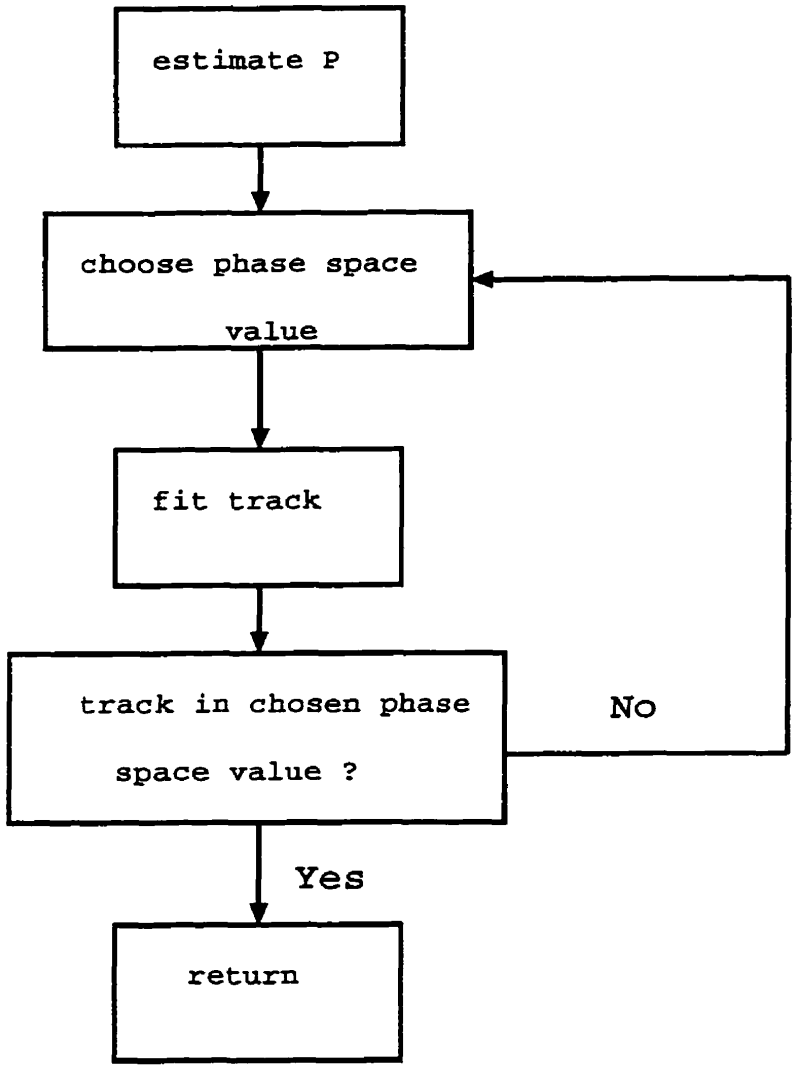

Figure 3.16: Iterative algorithm in PEANUT to search for the best track and momentum with a given set of hit positions on the FD and BD chambers.

and y positions at the center of each drift chamber. The procedure of this iterative algorithm is shown in Fig. 3.16.

TOF and Mass of the Scattered Particle

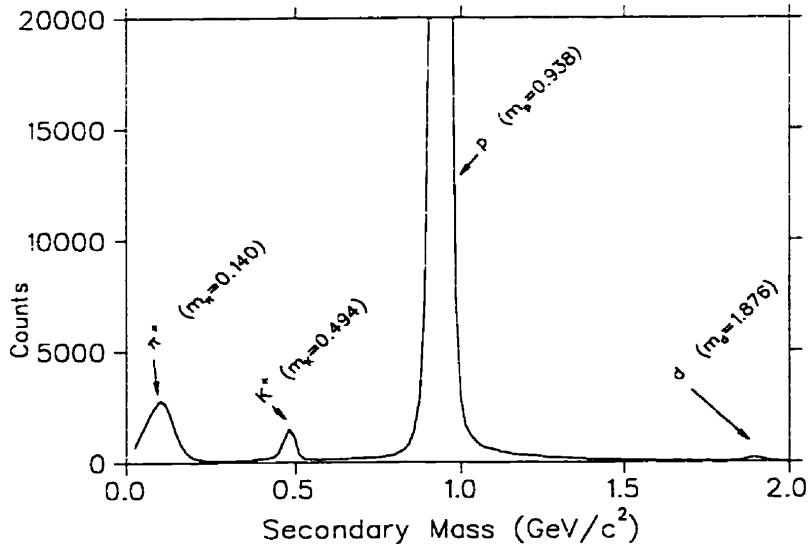

Figure 3.17: Secondary mass distribution from the raw data, with loose cuts on the track reconstruction goodness of fit, DCA and χ^2 (see below).

The time-of-flight of the scattered particle was measured by IT and BT, and was calculated from the equation:

$$TOF_{scat} = T_{BT} - T_{IT} - \frac{\Delta z}{c\beta_b}. \tag{3.17}$$

T_{IT} is the time when the beam particle passed through IT, and T_{BT} is the time when the scattered particle passed through BT. $\frac{\Delta z}{c\beta_b}$ is the time-of-flight for a incident beam particle that travelled between IT and the interaction vertex in the target area.

With known momentum P_{scat}, path length L and time-of-flight TOF_{scat}, the mass of the scattered particle can be calculated as follows:

$$m_{scat} = \frac{P_{scat}}{(L/TOF_{scat})}\sqrt{1-(\frac{L}{c\cdot TOF_{scat}})^2} \tag{3.18}$$

The reconstructed mass of the scattered particle was used to identify the K^-'s. Fig. 3.17 shows the secondary mass spectrum. As seen from Fig. 3.17, K^-'s were well distinguished from other particles by applying a cut on the secondary mass.

3.2.3 Global Track Reconstruction

The tracks of the incident and scattered particles were combined to reconstruct a complete event in order to identify the $\pi^- + p \rightarrow \Sigma^- + K^+$ reaction. This included the interaction vertex reconstruction and missing mass calculation, as described below.

Vertex Reconstruction

Once the trajectories of the incident and scattered particle were reconstructed, the closest approach between the incident particle's track and the scattered particle's track, where the two tracks were closest together, was determined. The interaction vertex was defined by the center point of the closest approach.

Cuts were applied to the x, y and z positions of the vertex in order to ensure that the reaction $\pi^- + p \rightarrow \Sigma^- + K^+$ took place in the lower hydrogen target. The reason to eliminate the reactions that took place in other materials in the target area was because the cuts on the energy deposited in the silicon detectors, E_{SI}, and K^- scattering angle, θ_{K^-}, were used to tag the stopping Σ^-'s; the optimization of these cuts was directly dependent on the kinetic energy and direction of the Σ^-, which were related to the materials in which the Σ^- was produced. If the

Σ^- was produced in other material rather than through the π^-'s interacting with free protons in the lower hydrogen target. the Fermi motion in the nuclei would smear the Σ^-'s energy and direction distributions. In the Monte Carlo simulation. however. the Σ^- was assumed to be produced in the hydrogen target. The Σ^-'s which were produced in the non-hydrogen part of the target. with smeared energy and direction. would cause θ_{K^-} and E_{SI} to deviate from what was expected. so that the Σ^- stopping efficiency would be reduced by using the same cuts on E_{SI} and θ_{K^-}.

Fig. 3.18 shows the x distributions in the target area. The bumps on both sides of the x vertex spectrum were caused by the the aluminum walls of the target. A cut $-6 \leq x \leq 6$ cm on the x vertex was used to exclude those background events.

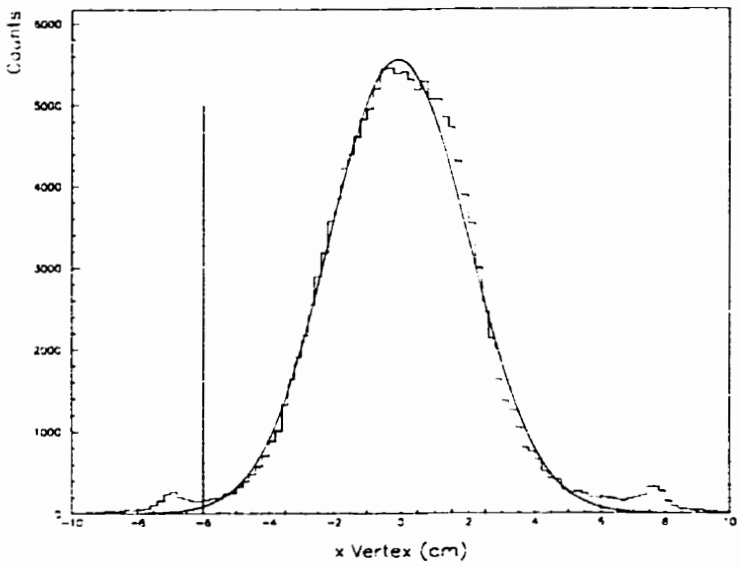

Figure 3.18: Distribution of the x vertex of the data with the PIKS trigger. The bumps on both sides of the spectrum were caused by the lower hydrogen target walls. The σ of a Gaussian fit to the x vertex profile in the target area, indicated by the solid curve, is 2.02 cm. The vertical lines indicate the x vertex cut.

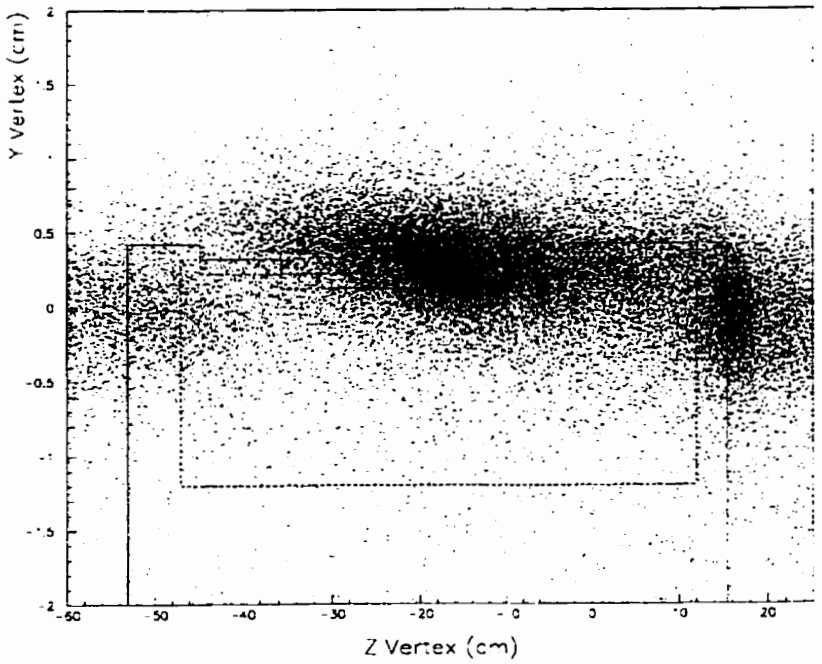

Figure 3.19: The 2D histogram of the y vertex versus the z vertex from empty target data. The solid lines show the outline of the lower liquid hydrogen target tank. The bottom wall of the target tank was at $y = -3.5$ cm. which is beyond the plot. The band at $z = -20$ cm in the spectrum was caused by the aluminum wall between the lower and upper target, and the band at $z = 16$ cm was caused by a dummy scatterer behind the target tank. The dashed lines show the y and z vertex cuts. The upper y vertex cut was stepped according to the actual target geometry.

Fig. 3.19 shows the 2-dimensional histogram of the y vertex versus the z vertex from empty target data. The measured z position for the front of the LH2 vessel was at $z = -53.0$ cm and the back at $z = 15.5$ cm. as shown in the plot by the solid lines. As described earlier, only those Σ^-'s tagged by the silicon detectors would have the highest probability to stop in the upper hydrogen target to form $(\Sigma^-.p)_{atom}$'s. Because the first row of the silicon detectors (located at $z = -47.8$ cm) had no output signals, the Σ^-'s which were produced in front of the first silicon detector row had no tags. The lower edge of the z vertex cut was set at $z = -48$ cm to exclude those events. The last silicon detector row was located at $z = 10.1$ cm. The higher edge of the z vertex cut was set at $z = 12.0$ cm to exclude the Σ^-'s which were produced behind the last silicon detector row. The z vertex cut is shown in Fig. 3.19 with dashed lines.

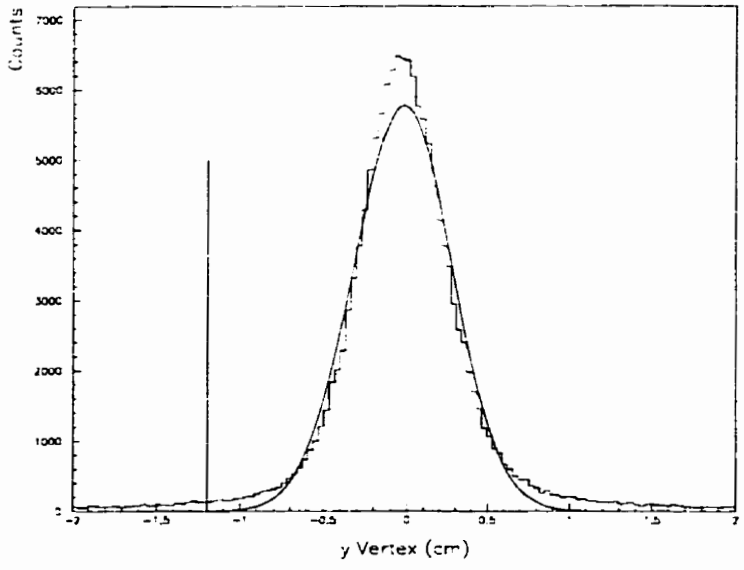

Figure 3.20: Distribution of the y vertex for the data with PIKS trigger. The σ of the Gaussian fit to the y vertex profile in the target area, shown by the solid curve, is 0.29 cm. The vertical line represents the position of the lower edge of the y vertex cut.

Fig. 3.20 shows the y vertex distribution. Due to the short lifetime of the Σ^-'s, the beam height was set to be very close to the top of the lower hydrogen target vessel. As shown in Fig. 3.20, the beam vertical width ($\sigma = 0.29$ cm) was much smaller than the height of the target vessel (3.5 cm). The lower edge of the y vertex cut was not a sensitive parameter; it was set at $y = -1.2$ cm determined by the Gaussian fit of the y vertex distribution, as shown in Fig. 3.20. Special care was needed for the higher edge of the y vertex cut because the boundary between the lower and the upper hydrogen targets had the complicated shape shown in Fig. 2.13. Therefore, the higher edge of the y vertex cut was defined according to the actual target geometry. It had the stepped shape, but was set at 0.1 cm lower than the measured target wall position because the resolution of the target y position measurement was 0.1 cm. More details of the determination of the higher edge of the y vertex cut are discussed at the end of this chapter.

Goodness of Fit

A goodness of fit, χ^2, of the scattered particle trajectory, was used to describe the goodness of the vertex and trajectory reconstruction. The definition of χ^2 used here is described in [68]. This χ^2 distribution accounts for a variable number of hits at each drift chamber for each event since the drift chambers are not 100% efficient. Fig. 3.21 shows the χ^2 distribution generated from the raw data, which was understood as a sum of many χ^2-like distributions on top of a relatively wide distribution which extended to very high χ^2 values. The events in the latter distribution were attributed to background events, which had hits in the FD and BD chambers but were not caused by the same particle. No complete trajectories could be reconstructed through the spectrometer for those events. The background distribution was approximated by a straight line fitting the distribution in the region $65 \leq \chi^2 \leq 100$. The cut at $\chi^2 \leq 55$ was determined by requiring the ratio of reconstructed events to "background" events to be less than one beyond

this cut.

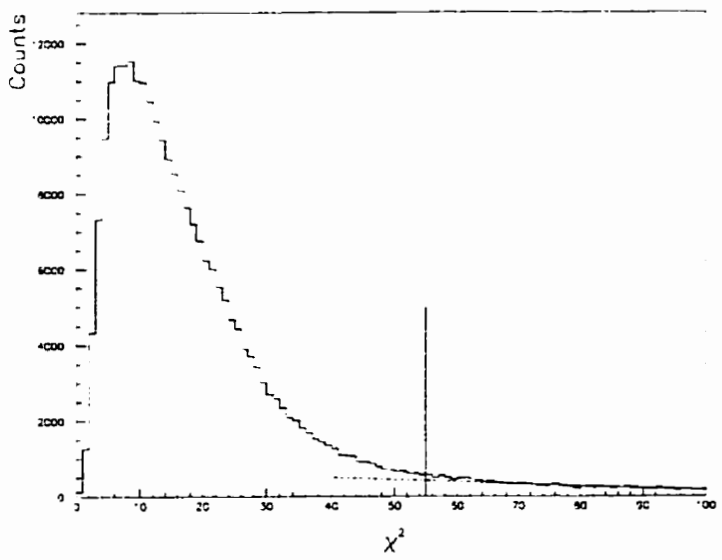

Figure 3.21: The χ^2 distribution of the raw data. The dashed line is the slope of the distribution in the region of $65 \leq \chi^2 \leq 100$. The vertical line shows the χ^2 cut.

Another variable that describes the goodness of fit for the complete trajectory reconstruction is the distance of closest approach (DCA) between the tracks of the incident and the scattered particles. In the ideal case, DCA should be zero. In reality, however, with finite measurement resolution, the DCA had a distribution peaked at zero and with a width related to the tracking resolution, as shown in Fig. 3.22. It could be described as a half Gaussian peak ($\sigma = 0.495$ cm) on top of a linear background distribution. The background consisted of those events for which the scattered particles were not related to the incident particles. A cut applied on DCA can ensure the accuracy of the vertex reconstruction. It was set at DCA $\leq$ 1.23 cm determined by 2.5σ, where σ is the rms width of the fitted half Gaussian distribution.

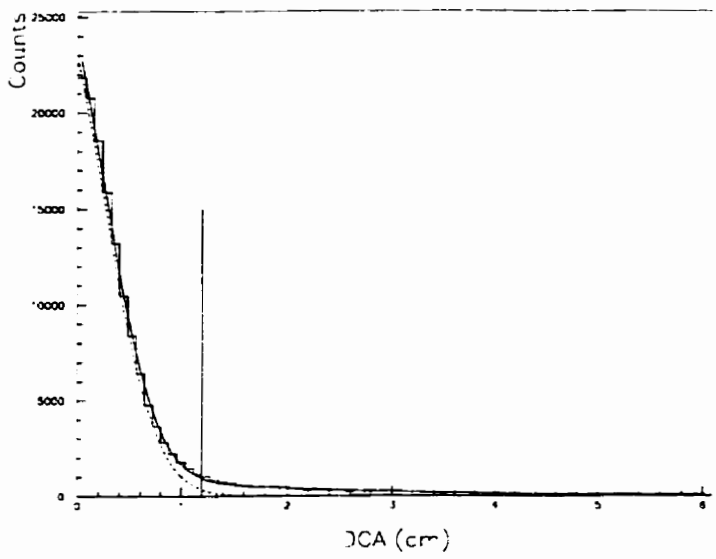

Figure 3.22: Distribution of the distance of closest approach (DCA) for the events which passed the χ^2 cut. The solid curve is the sum of a half Gaussian distribution and a linear background distribution, and the dashed curve shows the Gaussian distribution. The vertical line shows the DCA cut.

Missing Mass

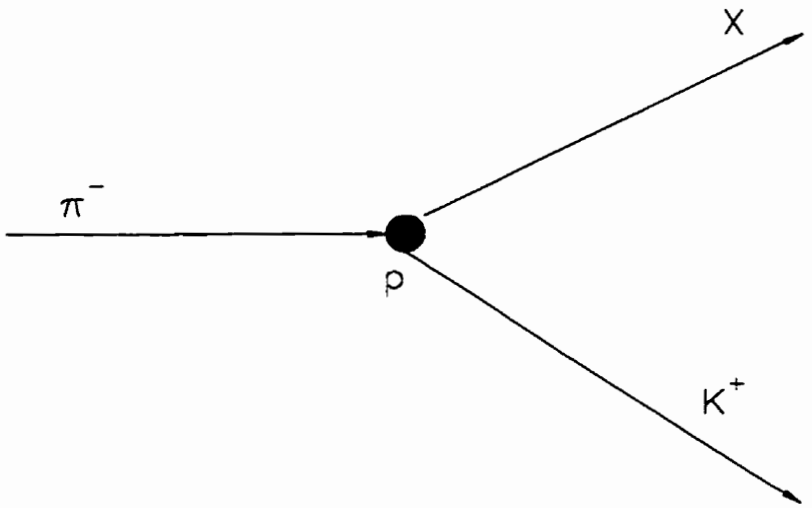

Figure 3.23: The $\pi^- + p \rightarrow K^- + X$ reaction. X represents an unknown particle to be identified via the missing mass calculation.

Once the incident and scattered particles are identified, and their momenta vectors are determined, a particular reaction can be identified by a missing mass calculation. For the reaction shown in Fig. 3.23, the incident π^- interacts with a free proton to produce a K^- and a unknown particle X. Assuming the speed of light $c = 1$, the 4-dimensional momenta for incident and outgoing particles are:
π^-: $(\vec{P}_{\pi^-}, iE_{\pi^-})$.
p: $(0, im_p)$.
K^+: $(\vec{P}_{K^-}, iE_{K^-})$.
X: $(\vec{P}_{\pi^-} - \vec{P}_{K^-}, i\sqrt{(\vec{P}_{\pi^-} - \vec{P}_{K^-})^2 + m_X^2})$.
where $\vec{P}_{\pi^-}$ is the momentum of the incident π^-, $\vec{P}_{K^-}$ is the momentum of the scattered K^-, and m_X is the missing mass. $m_{\pi^-} = 0.1396$ GeV/c^2, $m_{K^-} = 0.4937$ GeV/c^2 and $m_p = 0.9383$ GeV/c^2, are the masses of the π^-, K^- and proton.

respectively. According to the energy conservation law:

$$E_{\pi^-} + m_p = E_{K^+} + \sqrt{(\vec{P}_{\pi^-} - \vec{P}_{K^+})^2 + m_X^2}. \tag{3.19}$$

Therefore,

$$m_X = [(E_{\pi^-} + m_p - E_{K^+})^2 - (\vec{P}_{\pi^-} - \vec{P}_{K^+})^2]^{1/2}. \tag{3.20}$$

Since

$$E_{\pi^-} = \sqrt{P_{\pi^-}^2 + m_{\pi^-}^2}, \qquad E_{K^+} = \sqrt{P_{K^+}^2 + m_{K^+}^2}, \tag{3.21}$$

the missing mass for the $\pi^- + p \rightarrow X + K^+$ reaction is calculated from:

$$m_X = [(\sqrt{\vec{P}_{\pi^-}^2 + m_{\pi^-}^2} + m_p - \sqrt{\vec{P}_{K^+}^2 + m_{K^+}^2})^2 - (\vec{P}_{\pi^-} - \vec{P}_{K^+})^2]^{1/2}. \tag{3.22}$$

In eq. (3.22), the missing mass is calculated under the assumption that the π^- interacts with a free proton. As the mass of the Σ^- is 1.1974 GeV/c^2, Σ^-'s can be identified by making a cut on the missing mass spectrum.

3.2.4 Data Reduction

name of cut	Description	range
PIKS	Trigger	TRUE
MASS.K	Secondary Mass	0.37 - 0.60 GeV/c^2
ZVERT	z Vertex	-55 - 25 cm
XI2	χ^2	0 - 80
DCA	Distance of Cloest Approach	0 - 6 cm

Table 3.1: Cuts used in the data reduction to select (π^-, K^+) events.

In 1995, 5 weeks of beam time were spent on the (π^-, K^+) calibration experiment; an integrated beam flux of 2.3×10^{12} π^-s and 101 useful runs of data were collected

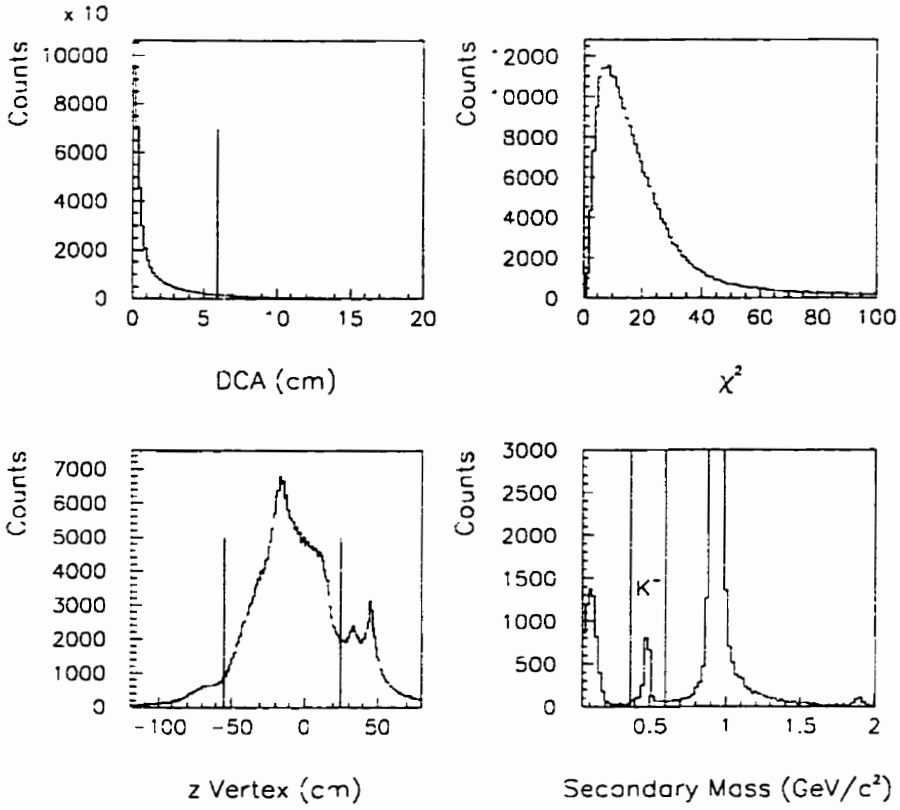

Figure 3.24: Histograms used in the data reduction. The vertical lines show the cuts used to select good (π^-, K^-) events. All histograms were generated from the raw data.

with roughly 2.8×10^7 events written on 80 magnetic tapes. However, even with the second level trigger cuts to reject scattered protons during the data collection, the majority of events on the tapes were still (π^-, p) elastic scattering events, considered as background for the calibration experiment. This can be seen in the secondary mass spectrum in Fig. 3.17, where the ratio of $\frac{K^-}{p}$ is less than 2%. In addition, with data on over 80 magnetic tapes, it is inconvenient and time consuming to do the final analysis. Therefore, by applying very loose cuts on the secondary mass and the quality of the track reconstruction (DCA and χ^2) spectra, a subset of the original data with reasonably clean (π^-, K^-) events was extracted so that the reduced data would be of a manageable size that could be stored on disk for the final analysis. This process was referred as "data reduction". The cuts used for the data reduction were much looser than the final cuts in the calibration analysis so that all interesting data were preserved. Fig. 3.24 shows the loose cuts, which are defined in Table 3.1, used in the data reduction to select (π^-, K^-) events. After the data reduction was completed, a fraction of $\sim 5.8 \times 10^{-3}$ of the original data was retained.

3.2.5 Basic Cuts to Identify the Reaction $\pi^- + p \rightarrow \Sigma^- + K^+$

Once the data reduction was completed, three categories of cuts were applied to the reduced data to identify the reaction $\pi^- + p \rightarrow \Sigma^- + K^+$ which took place in the lower hydrogen target: (1) the goodness of fit cuts, DCA and χ^2, to select the events with good vertex and trajectory reconstruction; (2) the kinematic cuts, secondary mass and missing mass cuts, to select the $\pi^- + p \rightarrow \Sigma^- + K^+$ reaction; (3) the reaction vertex (x, y and z) cuts to ensure that the reactions took place in the lower hydrogen target. The cuts in the first and third category have been described earlier. The determination of the second category of cuts is presented below.

Kinematic Cuts

Since the mass of the K^- is 0.4936 GeV/c^2, a cut on the secondary mass spectrum was applied to identify the scattered particle K^-. The cut from 0.4242 GeV/c^2 to 0.5632 GeV/c^2 shown in Fig. 3.25 was determined by $m_{K^-} \pm 4.5\sigma$, where σ = 0.0154 GeV/c^2 is the width of the Gaussian fit to the secondary mass spectrum.

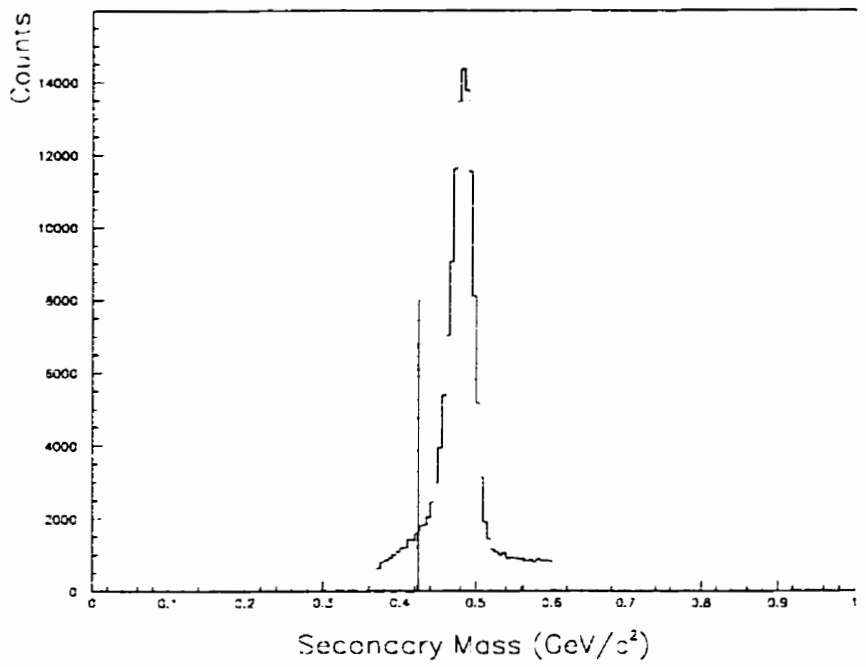

Figure 3.25: Secondary mass spectrum generated from the reduced data. The vertical lines show the cut used to identify K^-.

The Σ^-'s produced by the reaction $\pi^- + p \rightarrow \Sigma^- + K^-$ were identified by applying a cut on the missing mass spectrum. Fig. 3.26 shows the missing mass spectrum generated from the reduced data. The asymmetry of the missing mass distribution can be understood by examining Fig. 3.27. The upper part of Fig. 3.27 indicates that the contribution in the higher missing mass region comes from

lower secondary momentum events. The lower part of Fig. 3.27 shows that the secondary momentum distribution is not symmetric. There are more events on the lower secondary momentum side than in the higher side. This is due to π^-'s interacting with bound protons rather than free protons in the $\pi^- + p \rightarrow \Sigma^- + K^+$ reaction. As the mass of Σ^- is 1.197 GeV/c^2, the cut was defined by $1.1651 \leq m_{\Sigma^-} \leq 1.2289$ GeV/c^2, determined by $m_{\Sigma^-} - 4.5\sigma \leq MM \leq m_{\Sigma^-} + 4.5\sigma$, as shown in Fig. 3.26, where $\sigma = 0.00709$ GeV/c^2 is the rms width of a Gaussian fit to the missing mass peak.

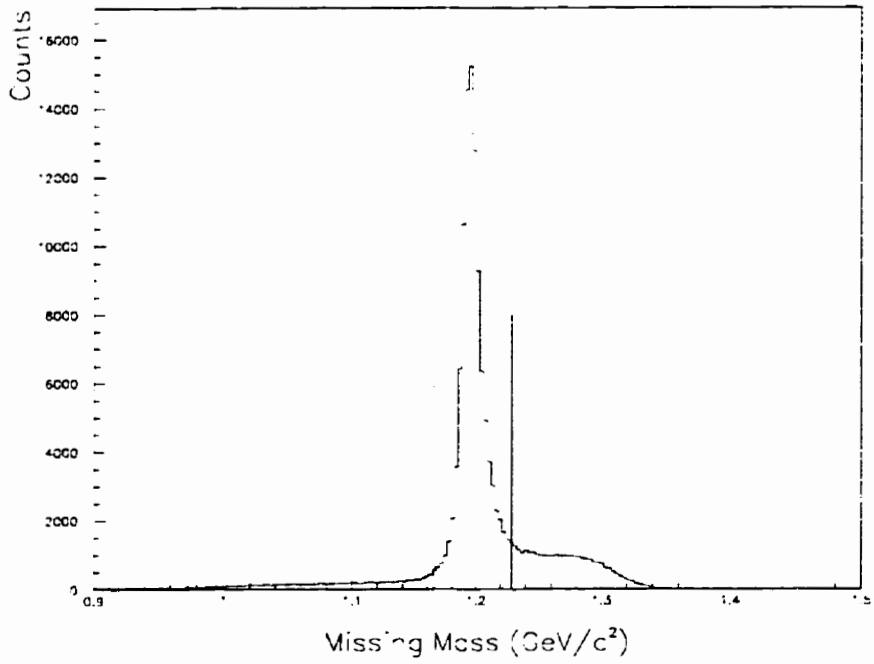

Figure 3.26: Missing mass spectrum for (π^-, K^+) events generated from the reduced data. The vertical lines show the cut used to identify Σ^-. The broad shoulder on the high side of the Gaussian peak was caused by the events in which a π^- interacted with a bound proton.

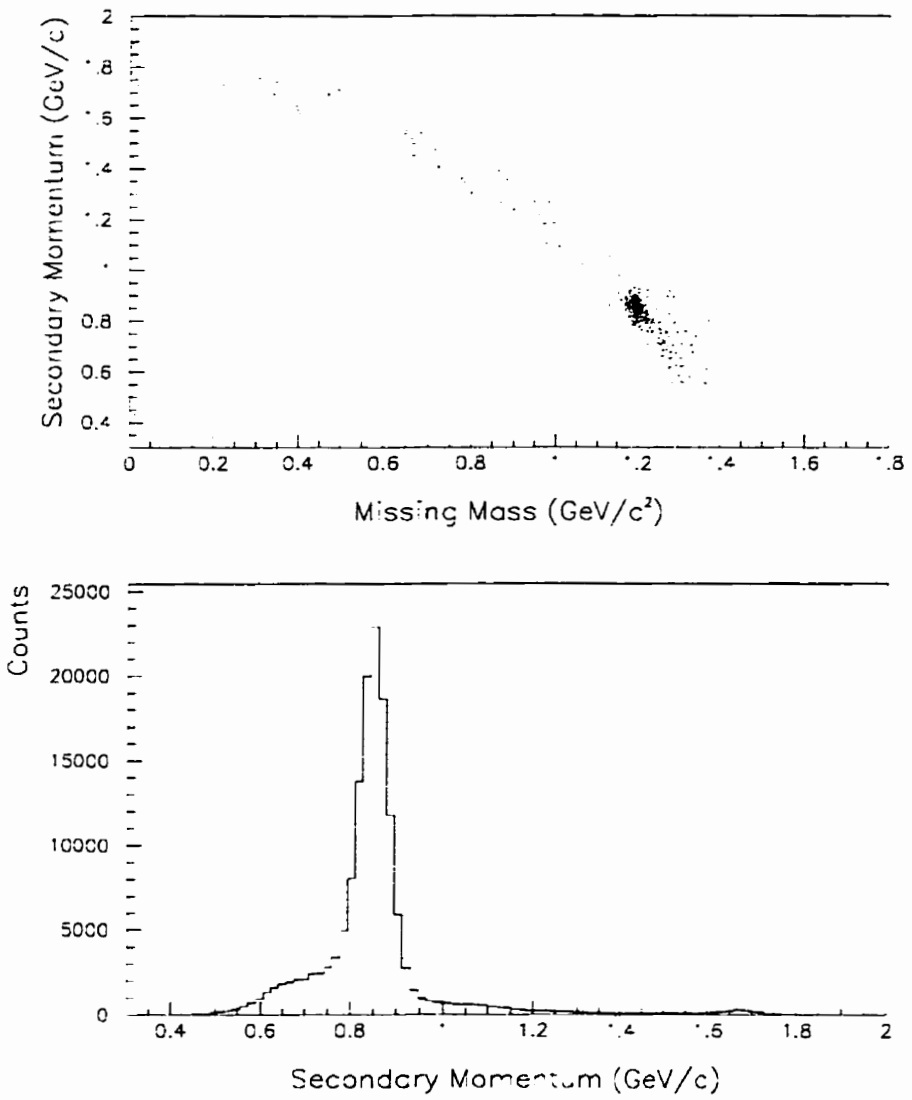

Figure 3.27: Histograms illustrating the asymmetry in the missing mass distribution. The upper plot is a 2D histogram of the secondary momentum versus the missing mass, and the lower plot is the distribution of the secondary momentum.

3.3 Tagging of Stopping Σ^-

To tag a Σ^- which had a high probability to stop in the upper liquid hydrogen target and to form a $(\Sigma^-, p)_{atom}$, additional cuts were applied to the events which passed the Σ^- identification tests. The tag was defined by the cuts on energy deposited in the silicon detectors and the K^+'s scattering angle θ_{K^+}, and other background cuts. These are discussed in detail below.

3.3.1 Cut on Energy Deposited in the Silicon Detectors

The most critical cut to identify the stopping Σ^-'s is on the energy deposited in the silicon detectors which the Σ^-'s passed through on their way to the upper target vessel. As Fig. 2.16 shows, the Monte Carlo simulation result indicates that Σ^-'s which deposit about 1.25 MeV to 2.25 MeV of energy in the silicon detectors should have the highest probability of stopping in the upper hydrogen target; for those Σ^-'s which stop in the tungsten degrader, their decay particles (such as π^-'s) deposit lower energy in the silicon detectors; Σ^-'s which deposit higher energy in the silicon detectors mostly stop in the aluminum before entering the upper target. The silicon detector energy cut used in final analysis was $1.25 \leq E_{SI} \leq 2.25$ MeV, based on the Monte Carlo simulation shown in Fig. 2.16.

3.3.2 Angle θ_{K^+} Cut

Another very sensitive cut to select stopping Σ^-'s is the scattering angle of the K^+, θ_{K^+}. This is a direct consequence of the target geometry. According to two-body kinematics, the trajectory of Σ^- and θ_{K^+} are related. The stopping probability of a Σ^- is directly dependent on the materials that it passed through. As a result, optimization of the cut on the angle θ_{K^+} greatly improves the Σ^- stopping efficiency. The cut $7.5^\circ \leq \theta_{K^+} \leq 10.0^\circ$ was determined according to the Monte Carlo result [121]. More discussion about the cut determination is given

at the end of this chapter.

Monte Carlo simulations indicate that the Σ^-'s which are tagged by $1.25 \leq E_{SI} \leq 2.25$ MeV and $7.5° \leq \theta_{K^-} \leq 10.0°$ should have a $(22 \pm 2)\%$ probability [121] of stopping in the upper liquid hydrogen target.

3.3.3 Other Background Cuts

The particles which left signals in the silicon detectors were not only Σ^-'s but also π^-'s from Σ^- decay. the dominant mode of the Σ^- decay is given by:

$$\Sigma^- \rightarrow n + \pi^-(99.848\%) \qquad (\tau = 1.479 \times 10^{-10}\text{s}) \tag{3.23}$$

Additional cuts must be applied to reject these false tags caused by the decay π^-'s. These cuts are discussed below.

Time Coincidence

By applying a cut on the time when the silicon detectors were hit. the silicon hits were assured of being in coincidence with the creation of the Σ^-'s. This rejected some of the false tags caused by other particles. Because of the slow rise time of silicon detector signals, however, only a loose cut could be applied to the silicon detector signal timing. Fig. 3.28 shows a 2-dimensional plot of the energy deposited versus the timing of the silicon detectors for events which passed the Σ^- identification tests. In Fig. 3.28, the triangular band was caused by real signals. and the rectangular band, with energy deposited less than 0.5 MeV, was caused by random background events. The two bands overlap in the low energy region. The cut on the silicon detector signal timing was chosen to be from 145 ns to 260 ns (shown in Fig. 3.28 with a solid box), which covered the timing range of the real signals.

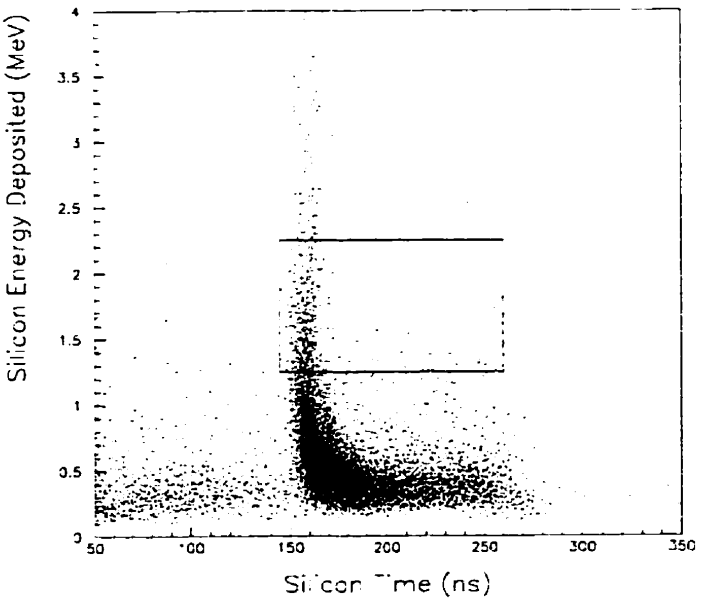

Figure 3.28: The 2-dimensional histogram of energy deposited versus timing of the silicon detectors. The box shows the cuts on the silicon detector timing and deposited energy used in the final analysis. The events in the triangular band were real signals, and the events in the rectangular band, with energy deposited less than 0.5 MeV, were random background events. The two bands overlap in the region of $145 \leq T_{SI} \leq 260$ ns and $0 \leq E_{SI} \leq 0.5$ MeV.

Position Coincidence

The false tags caused by the π^-'s from Σ^-'s decay can be further reduced by checking the locations of hits against the predictions from the two-body kinematics for the $\pi^- + p \rightarrow K^+ + \Sigma^-$ reaction. According to two-body kinematics, the direction of the Σ^- can be calculated from the beam direction and scattering angle θ_{K^+} of the K^+. Because of poor resolution in the z vertex, the x and y positions of the vertex were used instead to project the track of the Σ^- onto the $x - y$ plane of the silicon detector pad that was hit. As the y position of the Σ^- where it passed through the silicon detector pad is unknown, the distances from

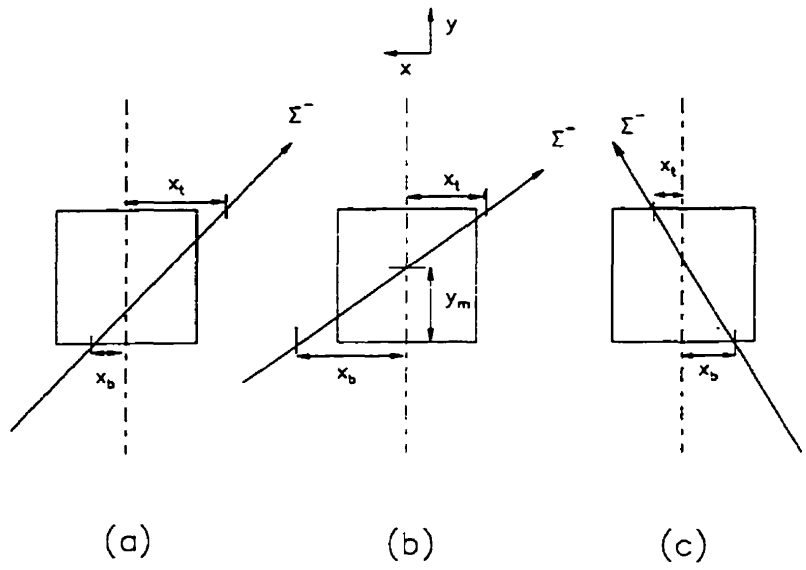

Figure 3.29: Schematic drawings of the silicon detectors with projections of Σ^- tracks onto the $x - y$ plane.

the Σ^- track to the horizontal center of the fired silicon detector at the bottom (X_b) and top (X_t) of the the silicon pad were calculated, as shown in Fig. 3.29. The minimum of these two values, $X_m = \min(|X_b|, |X_t|)$, was used to apply the cut. Fig. 3.29 shows a schematic drawing for three possible types of events labeled a, b and c. Ignoring all errors, X_m in cases a and c would be less than 0.5 cm because the width of a silicon pad is 1.0 cm. For case b, however, X_m would be larger than 0.5 cm even though the Σ^- did pass through the silicon pad. In this case, the height of the Σ^- track at the horizontal center of this silicon detector pad to the bottom of the silicon detector, Y_m, was calculated. One should have $0.0 \leq Y_m \leq 1.0$ cm for the ideal case (the height of silicon detector pad is 1.0 cm). Therefore, X_m was set to be zero for case b if the condition $0.0 \leq Y_m \leq 1.0$ cm was satisfied. Considering that the x resolution of the vertex reconstruction is ≈ 0.07 cm, the additional cut was defined as:

$$SILI\_XDIF : X_m \leq 0.7cm \tag{3.24}$$

to accept about 99% of the silicon hits caused by the Σ^-'s while rejecting about 33% of the false tags caused by π^-'s.

Cuts on the differences between the Σ^- creation vertex and the center of the silicon pad which was hit, along the x and z directions, can also remove some false tags caused by π^-'s. These distance differences were defined as following:

$$\Delta x = x_{SI} - x_{ver}, \qquad \Delta z = z_{SI} - z_{ver} \tag{3.25}$$

where x_{SI} and z_{SI} are the x and z positions at the center of the silicon pad which was hit, x_{ver} and z_{ver} are the x and z positions at the vertex where the Σ^- was created.

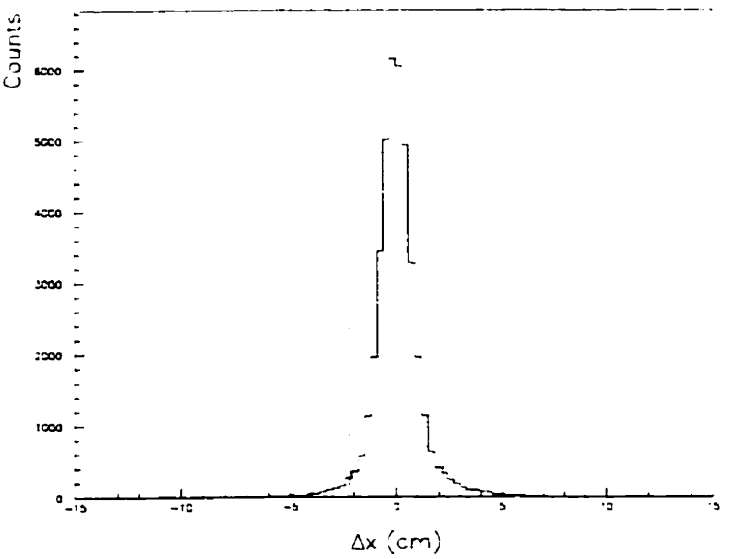

Figure 3.30: Distribution of the x distance between the silicon detector pad which was hit and the vertex for the events that passed all the Σ^- identification cuts and the SILI.XDIF cut. The vertical lines in the plot show the cut determined by $\pm 3\sigma$, where $\sigma = 0.75$ cm is the rms width of a Gaussian fit to the distribution.

Fig. 3.30 shows the Δx distribution (a Gaussian distribution centered at zero with $\sigma = 0.75$ cm) and the cut (vertical lines) that was applied in the final analysis. The cut on Δx was chosen to be $\pm 3\sigma$ of the Gaussian peak.

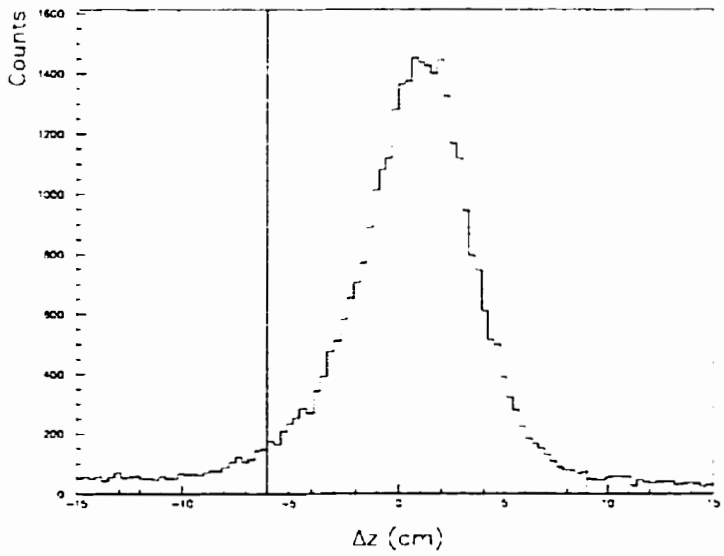

Figure 3.31: Distribution of the z distance between the silicon detector pad which was hit and the vertex of those events that passed all the Σ^- identification cuts and SILI.XDIF cut. The vertical lines in the plot represent the cut.

Fig. 3.31 shows the Δz distribution and the cut. Most of the stopping Σ^-'s in the upper hydrogen target were created in the lower hydrogen target within 3 cm in the upstream beam direction, according to a Monte Carlo simulation result shown in Fig. 3.32 [111]. However, because the resolution of the z vertex reconstruction was $\sigma_{zvert} = 1.1$ cm [118] in the target area, the expected silicon detector pad could be misidentified by one row (for a 3 cm spacing between the detector rows). In order to accept all Σ^-'s that stopped in the upper target, the cut on Δz at $-6 \leq \Delta z \leq 9$ cm was chosen to be fairly loose, allowing for two detector row spacings back and forward from the expected detector row.

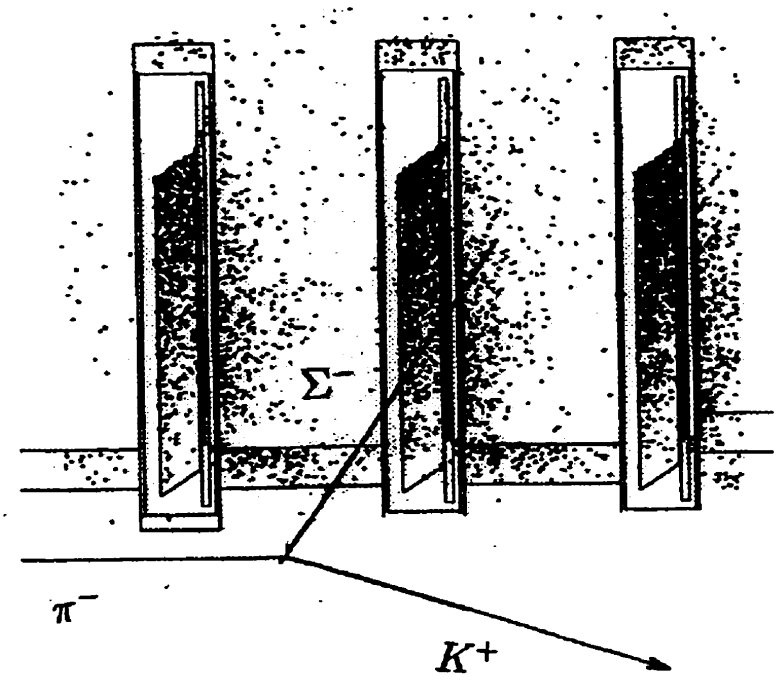

Figure 3.32: Monte Carlo simulation of the stopping Σ^-'s. Most of the stopping Σ^-'s in the upper hydrogen target were created in the lower hydrogen target within 3 cm in the upstream beam direction.

3.3.4 Summary of Cuts

In the previous sections, the cuts to identify Σ^-'s, which were produced through the reaction $\pi^- + p \rightarrow \Sigma^- + K^-$ in the lower hydrogen target and stopped in the upper hydrogen target, were described. Table 3.2 summarizes all the cuts used in the final analysis; Fig. 3.33, Fig. 3.34 and Fig. 3.35 give the description of these cuts.

Name of cut	Description	Range	Fraction of events passed
Basic cuts to identify $\pi^- + p \rightarrow \Sigma^- + K^-$			
XI2	χ^2	0.0 - 55.0	0.9511
DCA	Distance of closest approach	0.0 - 1.23 cm	0.9030
ZVERT	Z vertex	-47 - 12 cm	0.9229
XVERT	X vertex	-6.0 - 6.0 cm	0.9689
YVERT	Y vertex	according to actual target geometry, see Fig. 3.34	0.7473
MASS.K	Secondary mass	0.4242 - 0.5632 GeV/c^2	0.8767
MM.SIGMA	Missing mass	1.1651 - 1.2289 GeV/c^2	0.7079
Cuts to reject π^-'s from Σ^- decay			
SILI.T	Silicon timing	145 - 260 ns	0.7265
SILI.XDIF	$\min(\|X_b\|, \|X_t\|)$	-0.7 - 0.7 cm	0.4546
SILI.ΔX	$x_{SI} - x_{ver}$	-2.2 - 2.2 cm	0.6543
SILI.ΔZ	$z_{SI} - z_{ver}$	-6.0 - 9.0 cm	0.5206
Cuts to tag stopping Σ^-'s			
E_{SI}	Silicon energy	1.25 - 2.25 MeV	0.04958
θ_{K^-}	K^- Scattering angle	$7.5° - 10°$	0.2658

Table 3.2: Summary of cuts used in the final analysis. The fraction of the events passed is defined as $\frac{\#\text{events passed}}{\#\text{events tested}}$ for each cut independently.

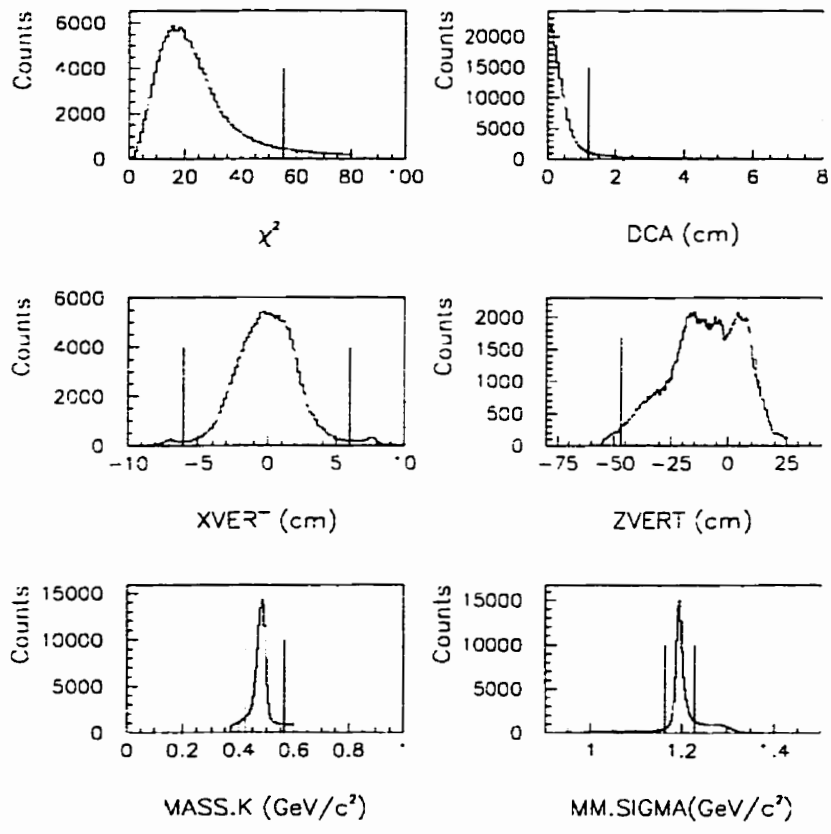

Figure 3.33: Histograms generated from the reduced data set. The vertical lines in the plots show the basic cuts defined in Table 3.2.

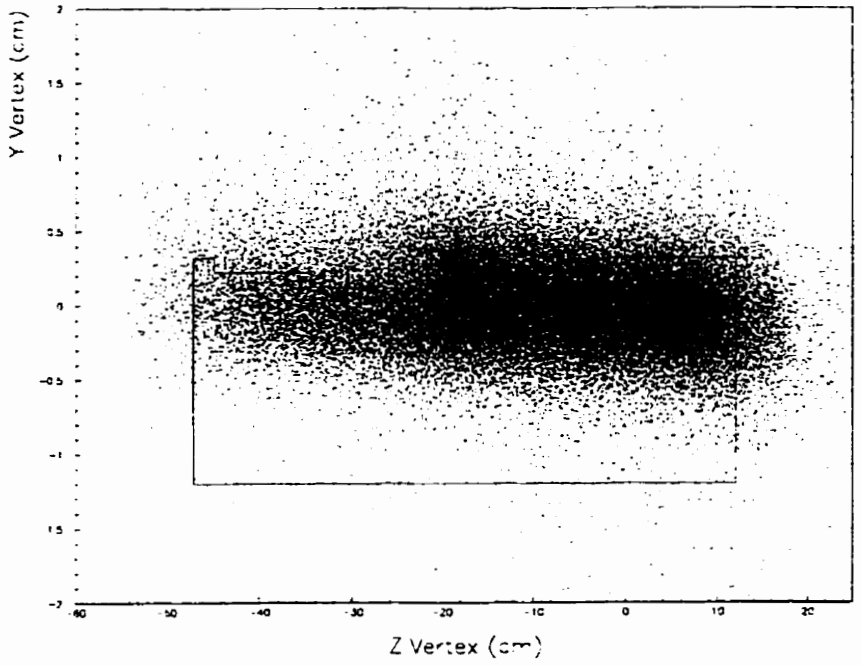

Figure 3.34: The 2D-histogram of y versus z vertex generated from the reduced data set. The solid curve in the plot shows the y and z vertex cuts to select the Σ^-'s produced in the lower hydrogen target.

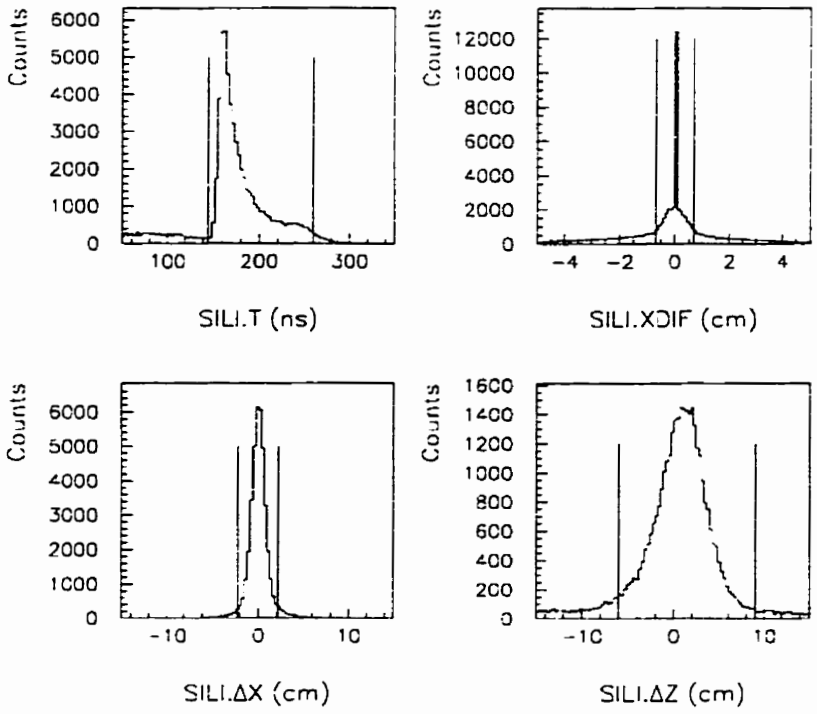

Figure 3.35: Histograms generated from the reduced data set with all basic cuts defined in Table 3.2. Two more extra cuts (SILI.T and SILI.XDIF) were applied to the bottom plots only. The vertical lines in the plots show additional cuts to reject π^-'s from Σ^- decay defined in Table 3.2. The narrow peak at SILI.XDIF=0 in the top right graph corresponds to "case b" events as described in Fig. 3.29.

3.4 Neutron Measurement

3.4.1 Data Processing

With raw ADC and TDC information from the neutron detectors, the time-of-flight, path length, electron-equivalent energy of the hit, and β^{-1} ($\beta^{-1} = \frac{c}{v}$) can be calculated; the neutral particles can then be identified.

Time-of-flight TOF_{ND}

According to the description in section 3.1.4, the time-of-flight of the neutron originating from the $(\Sigma^-, p)_{atom} \rightarrow n + \Lambda$ reaction can be calculated from the raw TDC information of the i^{th} element of the neutron detector which was hit. This is defined by the expression:

$$TOF_{ND} = 0.025 \times \frac{TDC_a^i + TDC_b^i}{2} - T_0^i - T_{(L \text{ or } R)} - T_{IT} - \frac{z_{ver} - z_{IT}}{v_{\pi^-}} \quad (3.26)$$

where T_0^i, T_L and T_R are calibration constants described earlier, T_{IT} is the IT timing, and $\frac{z_{ver} - z_{IT}}{v_{\pi^-}}$ is the time-of-flight for the incident particle π^- travelling from IT to the vertex of the reaction $\pi^- + p \rightarrow \Sigma^- + K^+$ in the target area.

Path Length l_{ND}

The path length of the neutron is defined by:

$$l_{ND} = \sqrt{(x_n - x_{ver})^2 + (y_n - y_{ver})^2 + (z_n - z_{ver})^2} \quad (3.27)$$

where x_{ver}, y_{ver} and z_{ver} are the vertex positions of $\pi^- + p \rightarrow \Sigma^- + K^+$; the x_n, y_n and z_n are the positions in the neutron detector which was hit. The y_n is calculated by equation (3.14) from the time difference between the PMT's at both ends of the neutron log; the x_n and z_n are estimated by the center of the neutron log which was hit.

Electron-equivalent Energy

The electron-equivalent energy of the signal from a neutron hit on the i^{th} log was calculated from:

$$E_{ND} = \sqrt{C_a^i(ADC_a^i - P_a^i)C_b^i(ADC_b^i - P_b^i)} \tag{3.28}$$

The electron-equivalent energy of a cluster [1] is the sum of the electron-equivalent energy of all signals of the cluster.

Neutron β^{-1}

The neutron β^{-1} is calculated as follows:

$$\beta^{-1} = c \cdot \frac{TOF_{ND}}{l_{ND}} \tag{3.29}$$

Neutral Particle Identification

First, the signals caused by charged particles were vetoed. This was done by the veto scintillators located between the neutron detector arrays and the target. The correlation between the hits on the neutron detectors and on the veto detectors was determined by their projected y and z positions. If a hit on the neutron detectors and a hit on a veto detectors was considered to be caused by the same particle, the y difference of these two hits should satisfy the condition $-25 \leq y_n - y_{veto} \leq 25$ cm. In addition, when projecting the width (along the z direction) of the neutron log which was hit to the vertex of the $\pi^- + p \rightarrow \Sigma^- + K^+$ reaction, the z position of the hit on the veto bar should be on the possible path between the vertex and the hit on the neutron detectors. If two of the above tests were satisfied, this signal was identified as being caused by a charged particle.

[1] Cluster: is a group of hits on the neighbouring logs in a neutron detector caused by a single neutral particle.

Second, a cluster of multiple hits caused by a single neutral particle was identified. Unlike the detection of charged particles, the detection of a neutral particle relies upon the neutral particle interacting with nuclei in the scintillating medium to liberate charged particles; then the detector responds to the charged particles. A neutral particle may liberate more than one charged particle; those charged particles can escape from the log of origin and fire adjacent logs. This type of multiple hit should be considered as a single hit, called a "cluster". If two neighbouring logs both produced a signal and the y difference of the two hit positions was within ± 30 cm, these two hits were considered as part of a cluster. Fig. 3.36 shows the definition of the neighbor logs. The time and hit position of clustered events were determined by the earliest hit in the cluster, and the electron-equivalent energy of a cluster was the sum of the electron-equivalent energy for all signals in the cluster.

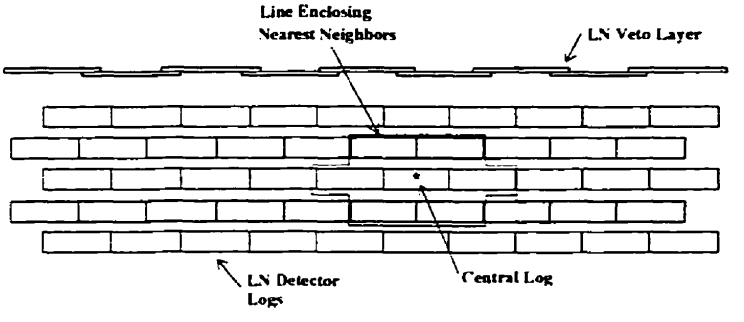

Figure 3.36: Plan view of a neutron detector array. It shows the nearest neighbor definition used in the grouping of neutral hits into a cluster.

3.4.2 Neutron Spectrum

In coincidence with the Σ^-'s which were produced through $\pi^- + p \rightarrow \Sigma^- + K^+$ and tagged by the silicon detectors, the neutron spectrum was studied to search for monoenergetic neutrons at $E_K = 43.5$ MeV created through the $(\Sigma^-, p)_{atom} \rightarrow \Lambda + n$ reaction. As the time-of-flight of the neutron was measured, a neutron β^{-1} ($\beta^{-1} = c \cdot \frac{TOF_{ND}}{l_{ND}}$) spectrum was generated because β^{-1} is proportional to TOF_{ND}. The energy of $E_K = 43.5$ MeV for neutrons corresponds to $\beta^{-1} = 3.4$. Cuts on the electron-equivalent energy of the neutron detectors were applied in order to reduce the background.

The neutrons whose events passed all the cuts defined in Table 3.2 are called the tagged neutrons. These events, with probability $\nu\varepsilon_{stop}$, were in coincidence with Σ^-'s captured on the hydrogen target to form $(\Sigma^-, p)_{atom}$'s. The neutrons whose events passed only the basic cuts defined in Table 3.2 are called the untagged neutrons. Unlike the tagged neutrons, the untagged neutrons mainly corresponded to the Σ^-'s decaying in flight or stopping in materials other than the upper hydrogen target, which contributed to the background in the tagged neutron spectrum. Fig. 3.37 shows examples of tagged and untagged neutron spectra with an electron-equivalent energy threshold of 3 MeV_{ee}.

3.4.3 Resolution of Neutron β^{-1} Measurement

According to equation (3.29), the neutron β^{-1} is determined by the neutron time-of-flight and the path length measurement. Therefore, the resolution of neutron β^{-1} mainly relies upon the following four factors:

Uncertainty in the time of the Σ^- stopping : The time-of-flight of a neutron should start when the $(\Sigma^-, p)_{atom}$ decayed and should end when the neutron interacted in one of the neutron bars. In other words, the neutron time-of-flight should be calculated from $TOF_n = TOF_{ND} - TOF_{\Sigma^-}$, where

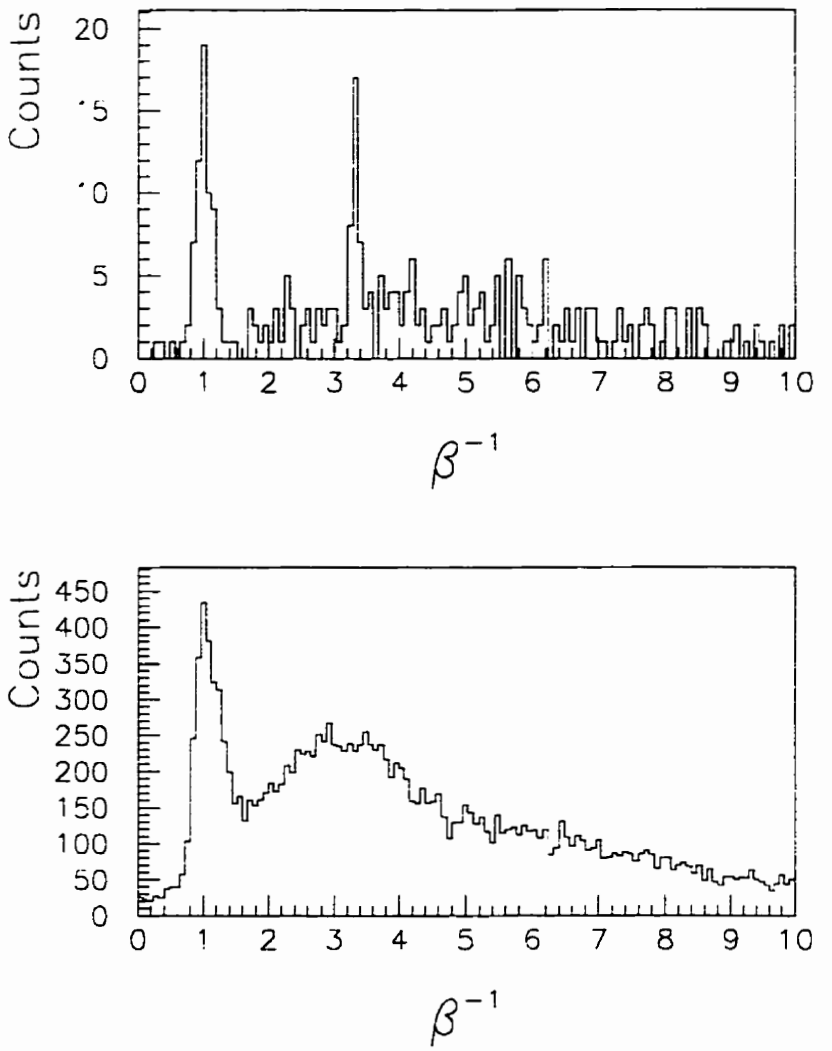

Figure 3.37: Examples of neutron β^{-1} spectra for an electron-equivalent energy threshold of 3 MeV_{ee}. The top plot is a tagged neutron spectrum and the bottom plot is an untagged neutron spectrum. The peaks at $\beta^{-1} = 1$ in both plots are the γ peaks, and the peak at $\beta^{-1} = 3.4$ in the tagged neutron spectrum represents the monoenergetic neutron signal from the $(\Sigma^-, p)_{atom} \rightarrow \Lambda + n$ reaction.

TOF_{ND} is defined by equation (3.26), and TOF_{Σ^-} is the time-of-flight of the Σ^- from its creation to its stopping to form the $(\Sigma^-, p)_{atom}$. An error σ_{start} was introduced in the β^{-1} measurement because the start time of the neutron flight was not exactly known due to the uncertainty of TOF_{Σ^-}.

Uncertainty in the position of Σ^- stopping : The flight path for a neutron, l_n, should be the length between the point where the Σ^- stops and the point of interaction in the neutron detectors. It is determined by:

$$l_n = \sqrt{[x_n - (x_{ver} + \Delta x_{\Sigma^-})]^2 + [y_n - (y_{ver} + \Delta y_{\Sigma^-})]^2 + [z_n - (z_{ver} + \Delta z_{\Sigma^-})]^2}.$$

where

$$l_{\Sigma^-} = \sqrt{\Delta x_{\Sigma^-}^2 + \Delta y_{\Sigma^-}^2 + \Delta z_{\Sigma^-}^2}$$

is the distance from the vertex of the Σ^- creation through the $\pi^- + p \rightarrow \Sigma^- + K^-$ reaction to the Σ^-'s stopping point. The unknown l_{Σ^-} caused another error, σ_{vert}, in the β^{-1} measurement.

Uncertainty in the position of interaction in the neutron detectors : In eq. (3.27), the positions of interaction in the neutron detectors were used to calculate the flight lengths of the neutrons. The x and the z positions of the interaction point in a neutron log were estimated by the center position of the neutron log. Because each neutron log is 5.08 cm thick along the x direction and 15.24 cm wide along the z direction, these dimensions introduced uncertainties on the x and z positions of the interaction point, which result in an error, σ_{hit}, in the β^{-1} measurement.

Intrinsic time resolution of the neutron detectors : There is an intrinsic time uncertainty of the neutron detectors, σ_{int}, which is dependent on the intrinsic features of the detectors, such as light output, types of PMT's, electronics and so on.

A Monte Carlo simulation program [111] was used by M. Burger to study the effect of the above uncertainties in the resolution of the neutron β^{-1} measurement. Table 3.3 gives a summary of the results for $\beta^{-1} = 3.5$.

Contributions	Uncertainty in β^{-1}
σ_{start}	0.040
σ_{vert}	0.028
σ_{hit}	0.048
σ_{int}	0.033
σ_{total}	0.076

Table 3.3: Summary of the uncertainties in the neutron β^{-1} measurement calculated by a Monte Carlo simulation program [111].

3.4.4 The Sensitivity of the Cuts

As the reaction $(\Sigma^-, p)_{atom} \rightarrow \Lambda + n$ is well understood, 43.5 MeV monoenergetic neutron signals are expected in the tagged neutron spectrum. This provides a way to optimize the cuts by studying the signal to noise ratio in the tagged neutron spectrum. In addition, because the kinematics of the Σ^- in the (π^-, K^+) calibration run were matched to the Ξ^- in the H particle run, studying the sensitivity of the cuts in the (π^-, K^+) data analysis is helpful in the determination of the cuts in the H particle search. The sensitivity of a cut can be described in terms of the signal to noise ratio, which is defined as:

$$R_{S/N} = \frac{S}{\sqrt{N}}, \tag{3.30}$$

where S is the number of monoenergetic neutrons found in the tagged neutron spectrum, and N is the number of background counts underneath the monoenergetic neutron peak.

For an individual cut, the $R_{S/N}$ is calculated by changing the higher or lower edge of the cut while keeping the other cuts defined in Table 3.2 fixed. The trend of the relative $R_{S/N}$ changing with the positions of the cut gives an indication of the cut optimization. In fact, this technique had been used earlier in the determination of the cuts in Table 3.2. Several important cuts are studied below. No error bars are shown in the following plots because only the relative $R_{S/N}$ is important for optimizing the cuts.

The E_{SI} and θ_{K^+} Cuts

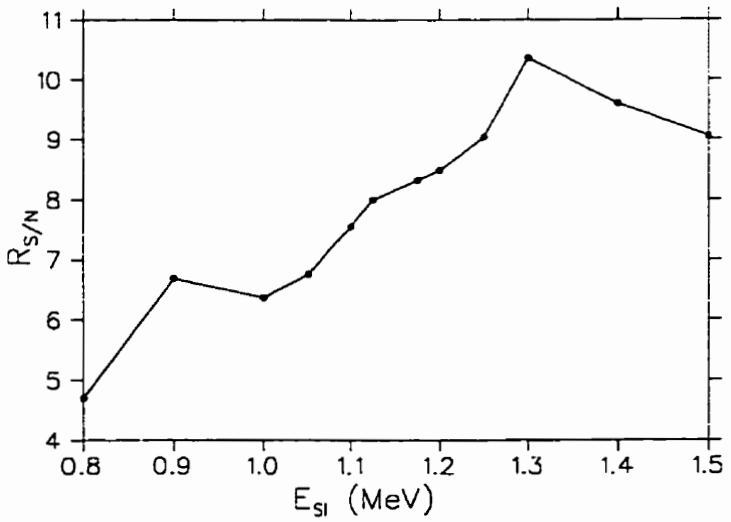

Figure 3.38: Signal to noise ratio versus the lower edge of the cut on the energy deposited in the silicon detectors, with the higher edge of the cut fixed at 2.25 MeV.

The most important cuts to tag those Σ^-'s which had the highest probability of stopping and being captured in the upper hydrogen target to form $(\Sigma^-, p)_{atom}$'s were the energy deposited in the silicon detectors, E_{SI}, and the scattering angle of the K^+, θ_{K^+}. These two cuts were optimized by the Monte Carlo programs. Studying the sensitivity of these cuts using the signal to noise ratio from the data,

can test and improve the Monte Carlo simulation.

Fig. 3.38 shows the signal to noise ratio ($R_{S/N}$) as a function of the lower edge of the cut on the energy deposited in the silicon detectors (E_{SI}), with the higher edge of the cut fixed at 2.25 MeV. As one can see, $R_{S/N}$ decreases very fast if the lower edge of the cut on E_{SI} is less than 1.2 MeV. This is because many background events are included in the spectrum if the lower edge of the silicon energy cut is chosen too low. However, if the lower edge of the cut on E_{SI} is larger than 1.4 MeV, it cuts off some good events and the signal to noise ratio also decreases.

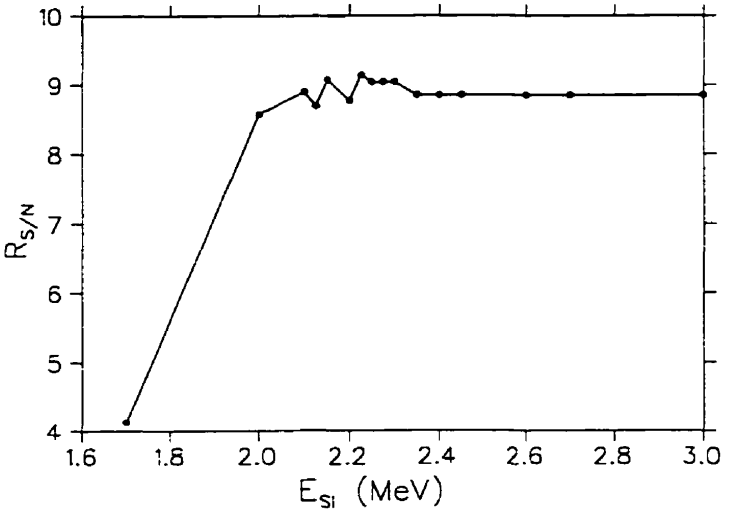

Figure 3.39: Signal to noise ratio versus the higher edge of the cut on the energy deposited in the silicon detectors, with the lower edge of the cut fixed at 1.25 MeV.

Fig. 3.39 shows the signal to noise ratio ($R_{S/N}$) as a function of the higher edge of the cut on the energy deposited in the silicon detectors (E_{SI}), with the lower edge of the cut fixed at 1.25 MeV. As seen in the plot, the signal to noise ratio decreases very fast if the higher edge of the cut on E_{SI} is less than 2.0 MeV. This is because good events are cut off if the higher edge of the cut on E_{SI} is too

low. However, if the higher edge of the cut on E_{SI} is larger than 2.4 MeV, the signal to noise ratio stays flat because there are few events in the $E_{SI} > 2.4$ MeV region.

Comparing Fig. 3.38 with Fig. 3.39, the sensitivity of the cut on the energy deposited in the silicon detectors is not symmetrical for the lower and the higher edge of the cut. This can be understood by the distribution of E_{SI} shown in Fig. 3.10. The distribution of the energy deposited in the silicon detectors is peaked in the lower energy region. Therefore, changing the lower edge of the cut dramatically either cuts off the good events or picks up many background events. If the higher edge of the cut is too low, it cuts off some good events; however, if the higher edge of the cut is too high, it only slowly picks up more background events.

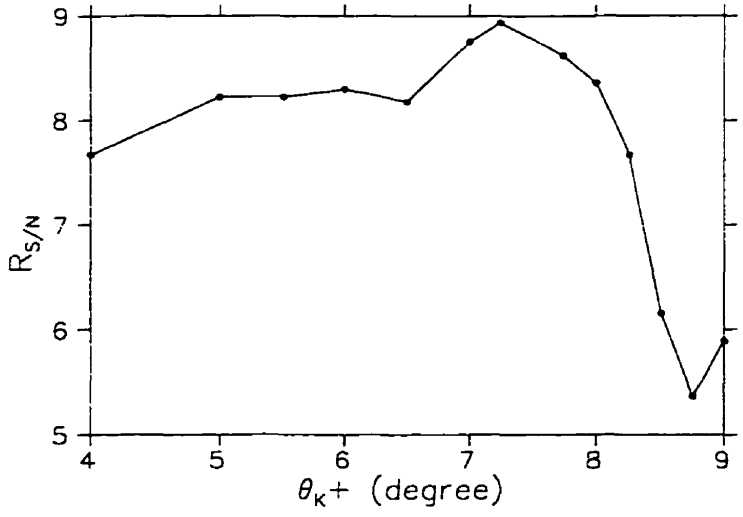

Figure 3.40: Signal to noise ratio versus the lower edge of the cut on the scattering angle of K^+, θ_{K^+}, with the higher edge of the cut fixed at 10°.

Fig. 3.40 shows the signal to noise ratio ($R_{S/N}$) as a function of the lower edge of the cut on the scattering angle of the K^+, θ_{K^+}, with the higher edge of the cut fixed at 10°. As one can see, if the lower edge of the cut on θ_{K^+} is less than 7°,

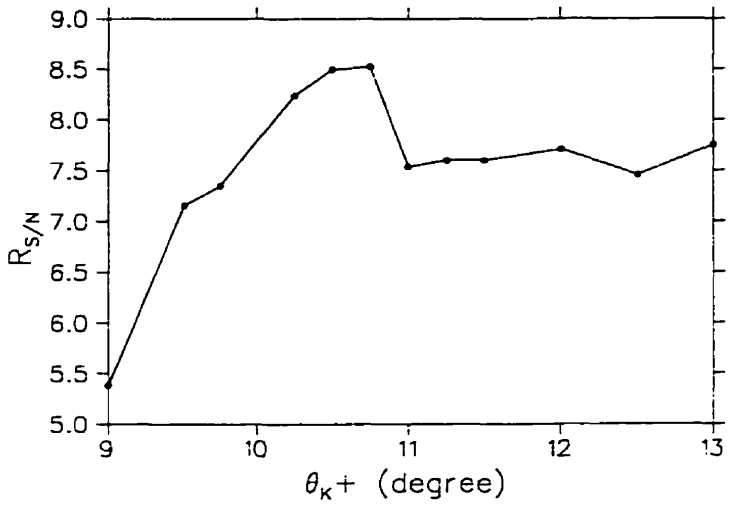

Figure 3.41: Signal to noise ratio versus the higher edge of the cut on the scattering angle of K^+, θ_{K^+}, with the lower edge of the cut fixed at 7.5°.

$R_{S/N}$ is decreasing by picking up more background events. However, if the lower edge of the cut on θ_{K^+} is larger than 8°, it cuts off some good events and the signal to noise ratio decreases.

Fig. 3.41 shows the signal to noise ratio ($R_{S/N}$) as a function of the higher edge of the cut on the scattering angle of K^+, θ_{K^+}, with the lower edge of the cut fixed at 7.5°. If the higher edge of the cut on θ_{K^+} is too small, the signal to noise ratio decreases very fast by cutting off good events; If the higher edge of the cut on θ_{K^+} is too large, the signal to noise ratio decreases by picking up more background events.

The y Vertex Cut

As described earlier, a properly chosen higher edge of the y vertex cut ensures that the Σ^-'s were produced in the lower hydrogen target, and the signal to noise ratio is not very sensitive to the lower edge of the y vertex cut. Keeping the shape of the higher edge of the y vertex cut matched to the shape of the

boundary between the two hydrogen targets and fixing the lower edge of the cut at $y = -1.2$ cm, the $R_{S/N}$ was calculated by changing the lowest point position on the higher edge of the y vertex cut along the y direction (see in Fig. 3.42). In the plot, when the lowest point position on the higher edge of the y vertex cut, YVERT_{min}, is less than -0.07 cm, $R_{S/N}$ decreases due to cutting the lower hydrogen target; when YVERT_{min} is greater than 0.05 cm, $R_{S/N}$ also decreases due to the including reactions that took place in the aluminum wall between the lower and upper target; when $\mathrm{YVERT}_{min} \sim 0.02$ cm, $R_{S/N}$ has the highest value. This position corresponds to 0.1 cm below the actual measured top aluminum wall position of the lower hydrogen target, which is within the error range of the target position measurement, ~ 0.1 cm.

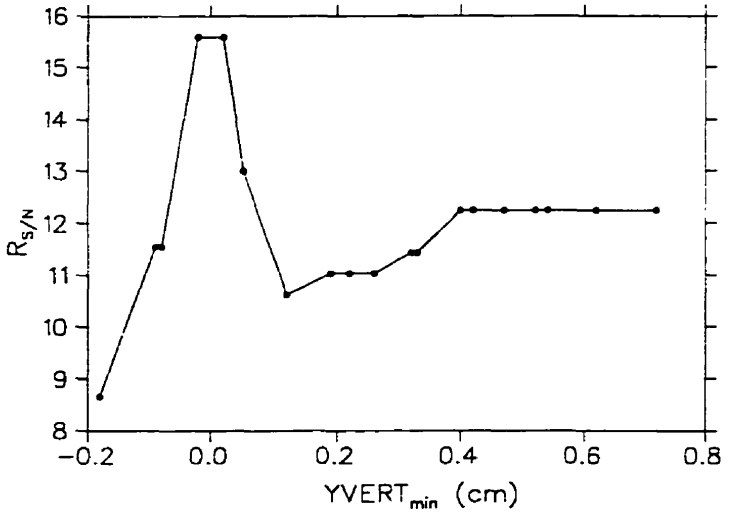

Figure 3.42: Signal to noise ratio versus the lowest point position of the higher edge of the cut on the y vertex, with the lower edge of the cut fixed at -1.2 cm.

The SILI.ΔZ and SILI.XDIF Cuts

The cuts SILI.ΔZ and SILI.XDIF played an important role in reducing the false tags, which were caused by the decay π^-'s produced in Σ^- decay.

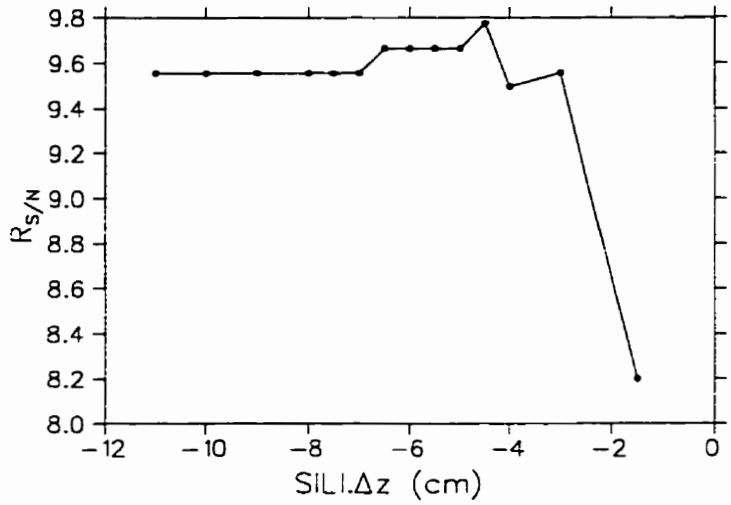

Figure 3.43: Signal to noise ratio versus the lower edge of the cut on the z distance between the silicon detectors which was hit and the vertex, with the higher edge of the cut fixed at 9 cm.

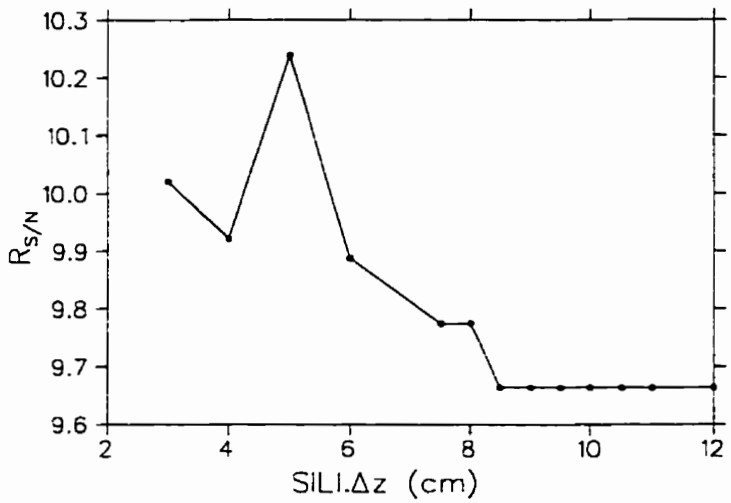

Figure 3.44: Signal to noise ratio versus the higher edge of the cut on the z distance between the silicon detector that was hit and the vertex, with the lower edge of the cut fixed at -6 cm.

Fig. 3.43 shows the signal to noise ratio as a function of the lower edge of the cut on the z distance between the silicon detector pad which was hit and the vertex, with the higher edge of the cut fixed at 9 cm. It indicates that good events are cut off if the lower edge of the SILI.Δz cut is larger than -3 cm.

Fig. 3.44 shows the signal to noise ratio as a function of the higher edge of the cut on the z distance between the silicon detector pad which was hit and the vertex, with the lower edge of the cut fixed at -6 cm. The result indicates that good events are cut off if the higher edge of the SILI.Δz cut is less than 6 cm. The cut made in our analysis is $-6 \leq SILI.\Delta z \leq 9$ cm. which should be wide enough to include all the good events.

The signal to noise ratio is not symmetrical for the lower edge and the higher edge of the SILI.Δz cut, as seen from Fig. 3.43 and Fig. 3.44. This is because the Σ^-'s produced through the reaction $\pi^- + p \rightarrow \Sigma^- + K^+$ go in the forward direction, travelling a small distance before they stop or decay.

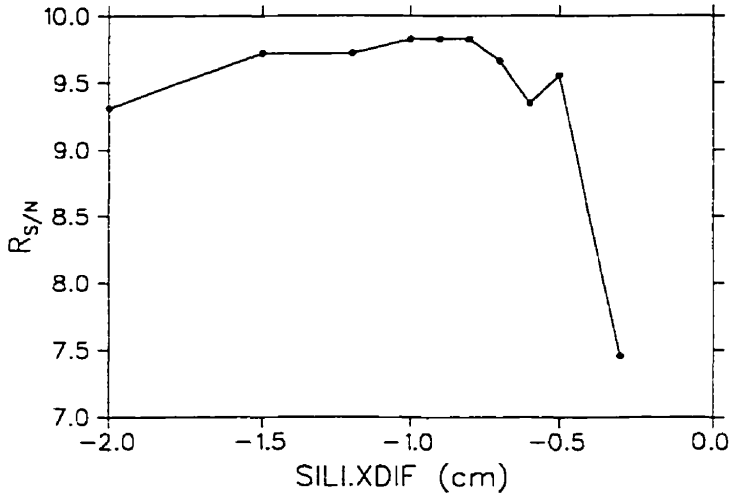

Figure 3.45: Signal to noise ratio versus the lower edge of the cut on the projected x position on the silicon pad which was hit, with the higher edge of the cut fixed at 0.7 cm.

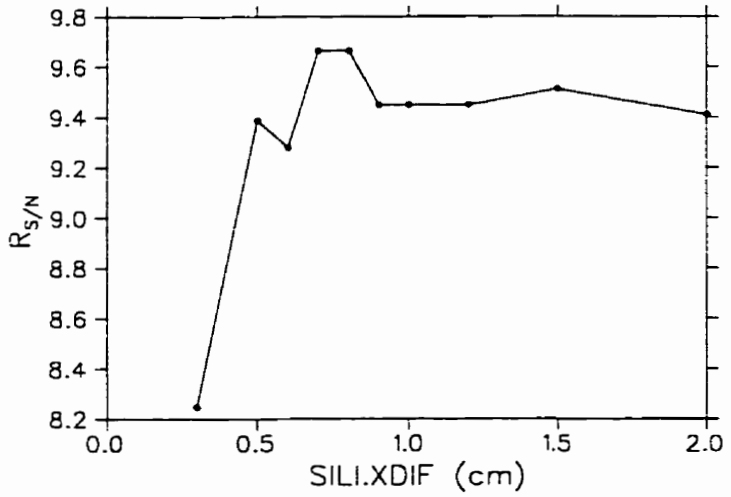

Figure 3.46: Signal to noise ratio versus the higher edge of the cut on the projected x position on the silicon pad which was hit. with the lower edge of the cut fixed at -0.7 cm.

Fig. 3.45 shows the signal to noise ratio as a function of the lower edge of the cut on the projected x position on the silicon detector pad which was hit. with the higher edge of the cut fixed at 0.7 cm. Fig. 3.46 shows the signal to noise ratio as a function of the higher edge of the cut on the projected x position on the silicon detector pad which was hit. with lower edge of the cut fixed at -0.7 cm. The result indicates that the cut $-0.7 \leq SILI.XDIF \leq 0.7$ cm used in the analysis is a very reasonable cut to select the Σ^-'s that passed through the silicon detectors while rejecting most of the false tags caused by π^-'s.

Chapter 4

Results And Discussion

4.1 Results

The main purpose of the (π^-, K^+) data analysis was to calibrate the sensitivity of the E813 experiment to detect a monoenergetic neutron in coincidence with $(\Sigma^-, p)_{atom}$ formation through the $(\Sigma^-, p)_{atom} \rightarrow \Lambda + n$ reaction. This was carried out by searching for a monoenergetic neutron peak at 43.5 MeV (corresponding to $\beta^{-1} = 3.4$) in the tagged neutron spectrum, as a signature of the reaction $(\Sigma^-, p)_{atom} \rightarrow \Lambda + n$. The number of neutrons found in the monoenergetic neutron peak in the tagged neutron spectrum was used to calculate the combined Σ^- stopping efficiency and neutron detection efficiency, $\varepsilon_{stop}\eta_{ND}$, which defines the sensitivity of experiment E813 for the H particle search.

Table 4.1 lists all the cuts used to define a tag for a stopping Σ^-. With cuts $7.5° \leq \theta_{K^+} \leq 10.0°$ and $1.25 \leq E_{SI} \leq 2.25$ MeV along with all the other cuts defined in Table 4.1, the number of tagged Σ^-'s from 1995's (π^-, K^+) data was found to be 1142. Fig. 4.1 shows the tagged neutron spectra with the electron-equivalent energy thresholds of 1 MeV_{ee}, 3 MeV_{ee}, and 5 MeV_{ee} respectively. As seen in Fig. 4.1, there is a sharp peak at the expected position, $\beta^{-1} = 3.4$, in the tagged neutron spectrum in all three cases. The background was fit with a

Name of cut	Description	Range	Fraction of events passed
Basic cuts to identify $\pi^- + p \rightarrow \Sigma^- + K^-$			
XI2	χ^2	0.0 - 55.0	0.9511
DCA	Distance of closest approach	0.00 - 1.23 cm	0.9030
ZVERT	Z vertex	-47 - 12 cm	0.9229
XVERT	X vertex	-6.0 - 6.0 cm	0.9689
YVERT	Y vertex	according to actual target geometry. see Fig. 3.34	0.7473
MASS.K	Secondary mass	0.4242 - 0.5632 GeV/c^2	0.8767
MM.SIGMA	Missing mass	1.1651 - 1.2289 GeV/c^2	0.7079
Cuts to reject π^-'s from Σ^- decay			
SILI.T	Silicon timing	145 - 260 ns	0.7265
SILI.XDIF	$\min(\lvert X_b\rvert, \lvert X_t\rvert)$	-0.7 - 0.7 cm	0.4546
SILI.ΔX	$x_{SI} - x_{ver}$	-2.2 - 2.2 cm	0.6543
SILI.ΔZ	$z_{SI} - z_{ver}$	-6.0 - 9.0 cm	0.5206
Cuts to tag stopping Σ^-'s			
E_{SI}	Silicon energy	1.25 - 2.25 MeV	0.04958
θ_{K^-}	K^- Scattering angle	$7.5° - 10°$	0.2658

Table 4.1: Summary of cuts used in the final analysis. The fraction of the events passed is defined as $\frac{\#\text{events passed}}{\#\text{events tested}}$ for each cut independently.

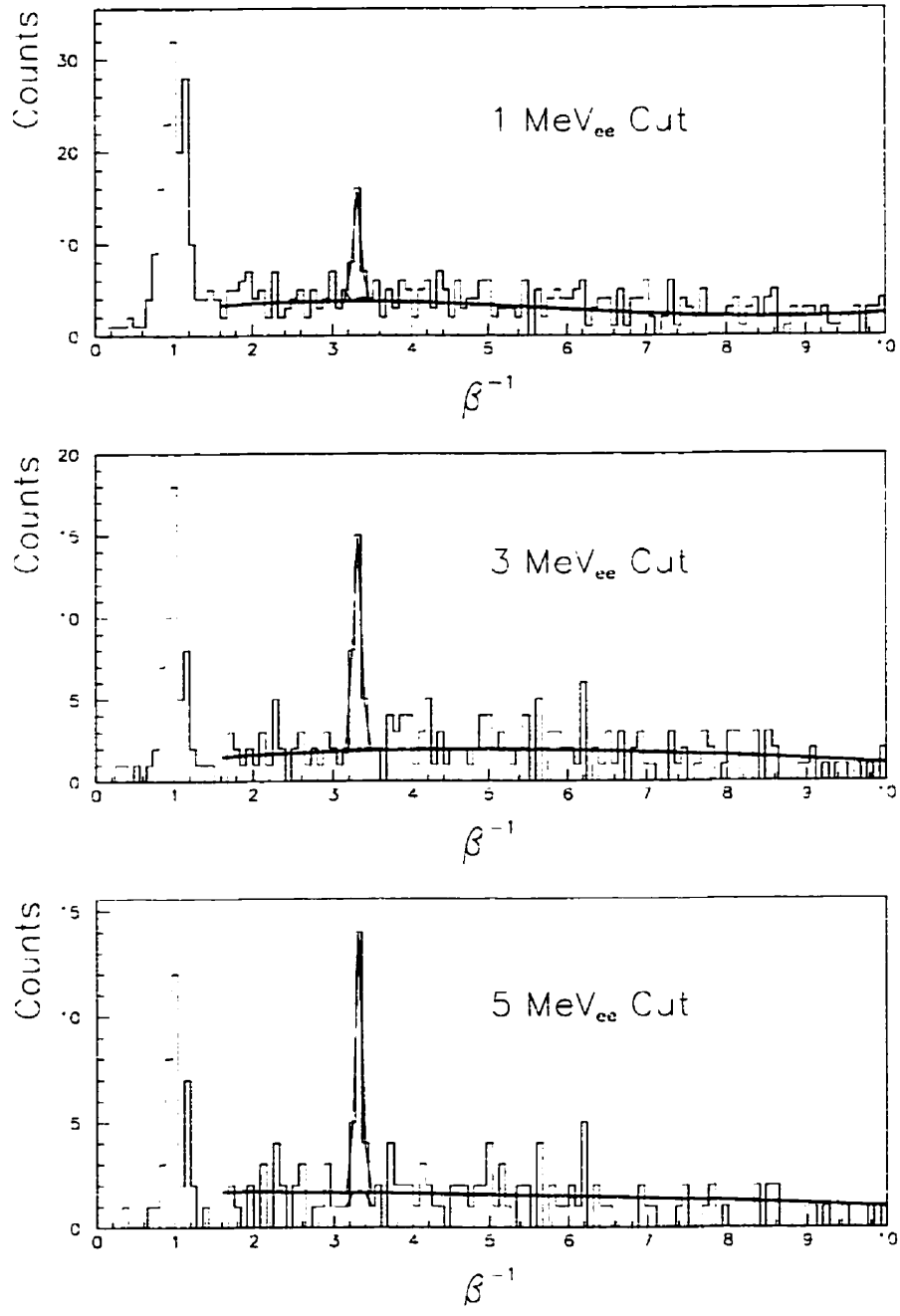

Figure 4.1: Tagged neutron β^{-1} spectra for the electron-equivalent energy thresholds of 1 MeV$_{ee}$, 3 MeV$_{ee}$, and 5 MeV$_{ee}$ respectively. The solid curves represent a third order polynomial fit to the background.

third order polynomial. Using the parameters listed in Table 4.2 to predict the monoenergetic neutron number by using the formula

$$N_{neutron} = N_{tag} \times \varepsilon_{stop} \times \nu \times R_{\Lambda} \times \eta_{ND}. \tag{4.1}$$

the results shown in Table 4.3 are obtained.

ε_{stop} (%)	ν (%)	R_{Λ} (%)	η_{ND} (%)		
			1 MeV_{ee}	3 MeV_{ee}	5 MeV_{ee}
22 ± 2	85 ± 5	53.2 ± 1.0	9.8 ± 1.0	8.3 ± 0.8	6.7 ± 0.7

Table 4.2: Parameters used for the monoenergetic neutron number predictions. ε_{stop} is the Σ^- stopping efficiency, and its value is taken from a Monte Carlo calculation [121]; ν is the efficiency for stopped Σ^- to form $(\Sigma^-, p)_{atom}$ as discussed in section 1.3.2 of chapter 1; R_{Λ} is the branching ratio for the $(\Sigma^-, p)_{atom} \rightarrow \Lambda + n$ reaction [106]-[107]; η_{ND} is the neutron detection efficiency estimated with the DEMONS program [116].

	measurement		calculation	
threshold	neutron #	$\varepsilon_{stop}\eta_{ND}$	neutron #	$\varepsilon_{stop}\eta_{ND}$
1 MeV_{ee}	20 ± 7	0.0449 ± 0.0160	9.6 ± 1.4	0.0216 ± 0.0029
3 MeV_{ee}	22 ± 6	0.0494 ± 0.0138	8.1 ± 1.2	0.0183 ± 0.0024
5 MeV_{ee}	18 ± 5	0.0405 ± 0.0115	6.6 ± 1.0	0.0147 ± 0.0020

Table 4.3: Summary of the final analysis results. All errors are statistical only.

As seen in Table 4.3, the combined Σ^- stopping efficiency and neutron detection efficiency, $\varepsilon_{stop}\eta_{ND}$, exhibits a large difference between the measured and calculated values. It should be noted that the value of ε_{stop} used in the calculation is preliminary. It is strongly dependent on the density of the hydrogen target, the target geometry, beam parameters, acceptance of the 48D48 spectrometer, and

the reactions under study for the Σ^- decay. More work on Monte Carlo simulation is needed in order to understand the disagreement between the measurement and the calculation. This project has been planned, and will be conducted later.

4.2 Discussion

4.2.1 Background Evaluation

The method used in the background evaluation of the tagged neutron spectra plays a very important role in estimating the number of monoenergetic neutrons. Fig. 4.2 gives a comparison of the background evaluation by using different methods. Originally the untagged neutron spectra scaled by the factor, $\frac{\#tagged}{\#untagged}$, was used to estimate the tagged neutron spectra background [68][114]. In other words, the neutron spectrum associated with Σ^- production with only the basic cuts in Table 4.1 and no cuts on the silicon detectors and scattering angle θ_{K^-}, scaled by the $\frac{\#tagged}{\#untagged}$ ratio was used previously to estimate the background in the tagged spectrum. As seen in Fig. 4.2, however, these untagged neutron spectra do not have the same shape as the background in the tagged neutron spectra. There is a broad peak around $\beta^{-1} = 3.4$ in the untagged spectra, while there appears to be a flat background underneath the monoenergetic neutron peak at $\beta^{-1} = 3.4$ in the tagged spectra. This is because the untagged spectra include events in which there were Σ^-'s stopped in material other than hydrogen, and those events were mostly excluded in the tagged spectra by appropriate cuts on silicon detectors and the scattering angle, θ_{K^-}. In order to understand this, one can recover some of those events, which Σ^-'s stopped in material other than hydrogen, in the tagged spectrum by loosening the cut on the energy deposited in the silicon detectors. Keeping all the other cuts in Table 4.1 unchanged, only extending the cut on the energy deposited in the silicon detectors from $1.25 \leq E_{SI} \leq 2.25$ MeV to $0.8 \leq E_{SI} \leq 3.0$ MeV, as shown in the upper spectrum of Fig. 4.3, the broad

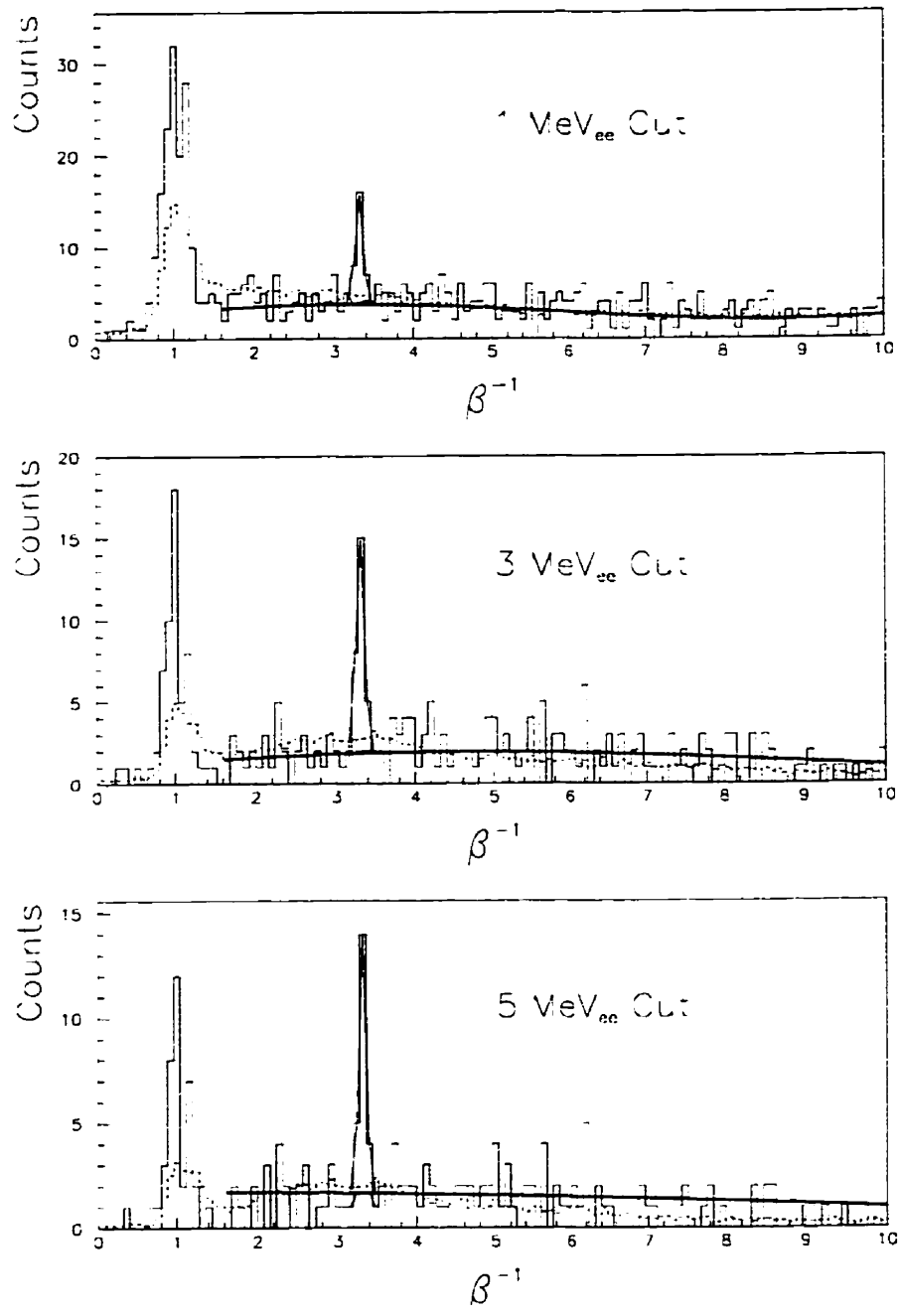

Figure 4.2: Comparison of different background estimates for tagged neutron spectra (as defined in Table 4.1) at thresholds of 1 MeV_{ee}, 3 MeV_{ee} and 5 MeV_{ee}. The solid curves represent a third order polynomial fit to the background, and the dashed curves represent the scaled untagged neutron spectra.

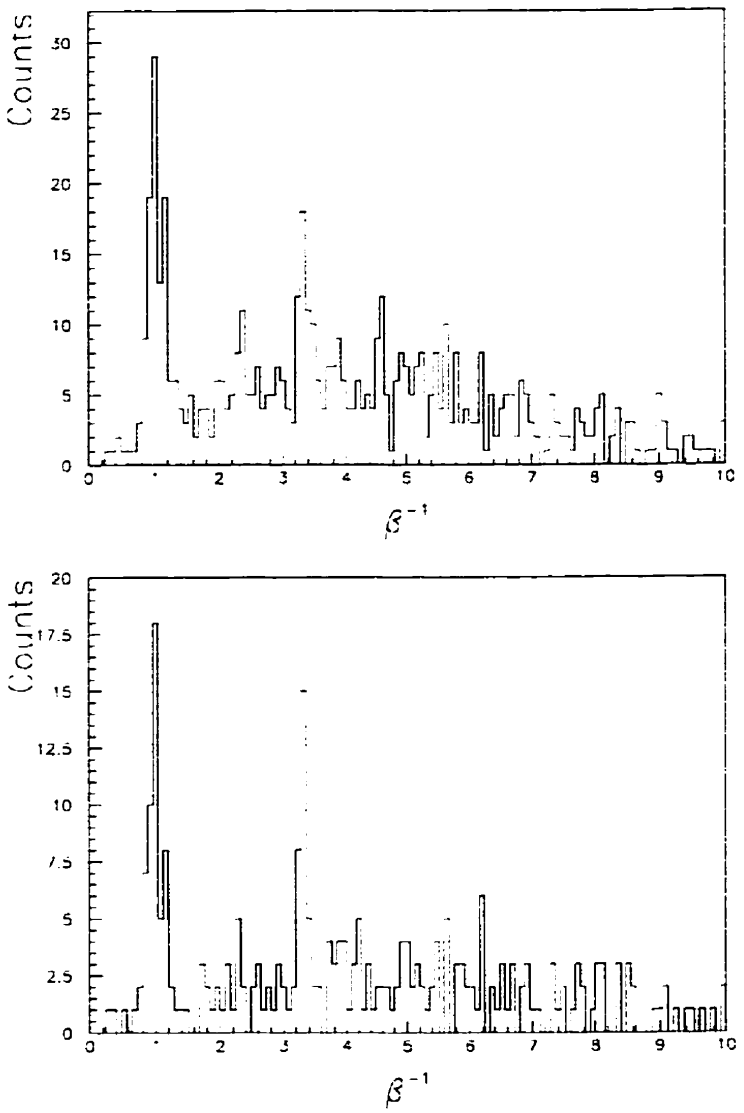

Figure 4.3: Comparison of tagged neutron spectra at a threshold of 3 MeV_{ee} with different silicon energy cuts. The upper spectrum is for the cut of $0.8MeV \leq E_{SI} \leq 3.0MeV$, and the lower spectrum is for a tighter cut of $1.25MeV \leq E_{SI} \leq 2.25$ MeV.

peak around $\beta^{-1} = 3.4$ appears. Therefore, the scaled untagged neutron spectra do not yield a good estimate for the background in the tagged neutron spectra. As seen in Table 4.4, the background would be overestimated by 24%–48% if this method were used.

threshold	background counts by FIT1: n_{b1}	background counts by FIT2: n_{b2}	$\frac{n_{b2}-n_{b1}}{n_{b1}}$
1 MeV_{ee}	11.3	14.2	26%
3 MeV_{ee}	5.6	8.3	48%
5 MeV_{ee}	5.0	6.2	24%

Table 4.4: Evaluation of the tagged neutron spectra background by using different methods. FIT1 represents using a third order polynomial fit to the background, while FIT2 represents using the scaled untagged spectra.

4.2.2 Comparison between Present and Previous Results

The neutron peak at $\beta^{-1} = 3.4$ found in the tagged neutron spectra, as shown in Fig. 4.1, has determined the sensitivity of the E813 experiment to detect a monoenergetic neutron in coincidence with a $(\Sigma^-, p)_{atom}$ formation. However, in comparing the combined efficiency, $\varepsilon_{stop}\eta_{ND}$, of the measured values with the predictions, shown in Table 4.3, one finds that the measured values are about two times larger than the predictions. Mention should be made first that the predicted value of $\varepsilon_{stop}\eta_{ND}$ was calculated with two different Monte Carlo programs. In order to investigate the validity of the present data analysis, a comparison between the present analysis (referred to as the "new" analysis) and a previous analysis (referred to as the "old" analysis) done by Markus Burger [111] with the same data is discussed.

However, it is not straight forward to make a precise comparison between the "new" analysis and the "old" analysis because most of the parameter files had

been re-calibrated for the "new" analysis; such as the timing parameter files, the silicon detector parameter files, the chamber position parameter file, the neutron detector parameter files, and so on. Furthermore, many mistakes in the analyzing program subroutines have been discovered since then and corrected. If one ignores these changes, however, the main differences between the "new" analysis and the "old" analysis are that:

1. there are tighter cuts in the "new" analysis than in the "old" analysis on the silicon detector geometry, such as SILI_ΔX, SILI_ΔZ;

2. a YVERT cut was introduced according to the actual target geometry in the "new" analysis, while there was no YVERT cut in the "old" analysis;

3. the tag definition in the "new" analysis is $7.5° \leq \theta_{K^-} \leq 10°$ and $1.25 \leq E_{SI} \leq 2.25$ MeV, while it was $8.5° \leq \theta_{K^-} \leq 11°$ and $1.2 \leq E_{SI} \leq 2.2$ MeV in the "old" analysis.

In the following, after removing the extra cuts introduced in the "new" analysis, the same data were reanalyzed with the updated analyzing program and parameter files, but using the cuts defined in the "old" analysis, with both angle cuts $8.5° \leq \theta_{K^-} \leq 11°$ and $7.5° \leq \theta_{K^-} \leq 10°$ respectively, to see if the result obtained from the updated analyzing program and parameter files is consistent with the "old" result. The results are discussed below.

The $8.5° \leq \theta_{K^+} \leq 11°$ Cut

With cuts $8.5° \leq \theta_{K^-} \leq 11°$ and $1.2\text{MeV} \leq E_{SI} \leq 2.2\text{MeV}$, and all the other cuts defined in Table 4.5, the number of tagged Σ^- from the (π^-, K^-) data obtained in 1995 was found to be 1857 (this compares to 1418 in the "old" analysis [111]). Fig. 4.4 shows the resulting neutron spectrum with the electron equivalent energy threshold of 3 MeV_{ee}. The background for the upper plot was fit with a third order

polynomial, and the background for the lower plot was fit with the untagged neutron spectra scaled by a factor $\frac{\#tagged}{\#untagged}$. Using the parameters listed in Table 4.6 to predict the monoenergetic neutron number by using formula (4.1), the final results are shown in Table 4.7. As seen from Table 4.7, 11 ± 4 monoenergetic neutrons (43.5 MeV) were found out of 1418 tagged Σ^-'s in the "old" analysis [111], with the background fit by the untagged neutron spectra. In the "new" analysis, the number of monoenergetic neutrons was found to be 9 ± 6 with the background fit by the untagged spectra and 15 ± 6 with the background fit by a polynomial, from 1857 tagged Σ^-'s. The two results are consistent with each other within the error range. Furthermore, the measurement results are very close to the Monte Carlo results, with a tag definition of $8.5° \leq \theta_{K^-} \leq 11°$ and $1.2\text{MeV} \leq E_{SI} \leq 2.2$ MeV.

Name of cut	Description	Range
E_{SI}	Silicon energy	1.2 - 2.2 MeV
θ_{K^-}	K^- scattering angle	$8.5° - 11°$
MM.SIGMA	Missing mass	1.13 - 1.27 GeV/c^2
MASS.K	Secondary mass	0.42 - 0.56 GeV/c^2
ZVERT	Z vertex	-40 - 10 cm
XI2	χ^2	0.0 - 50.0
DCA	Distance of closest approach	0.0 - 4.0 cm
SILI.T	Silicon timing	150 - 260 ns
SILI.ΔX	$x_{SI} - x_{ver}$	-2.0 - 2.0 cm
SILI.ΔZ	$z_{SI} - z_{ver}$	-10.0 - 10.0 cm

Table 4.5: Cuts used in the neutron spectrum in Fig. 4.4.

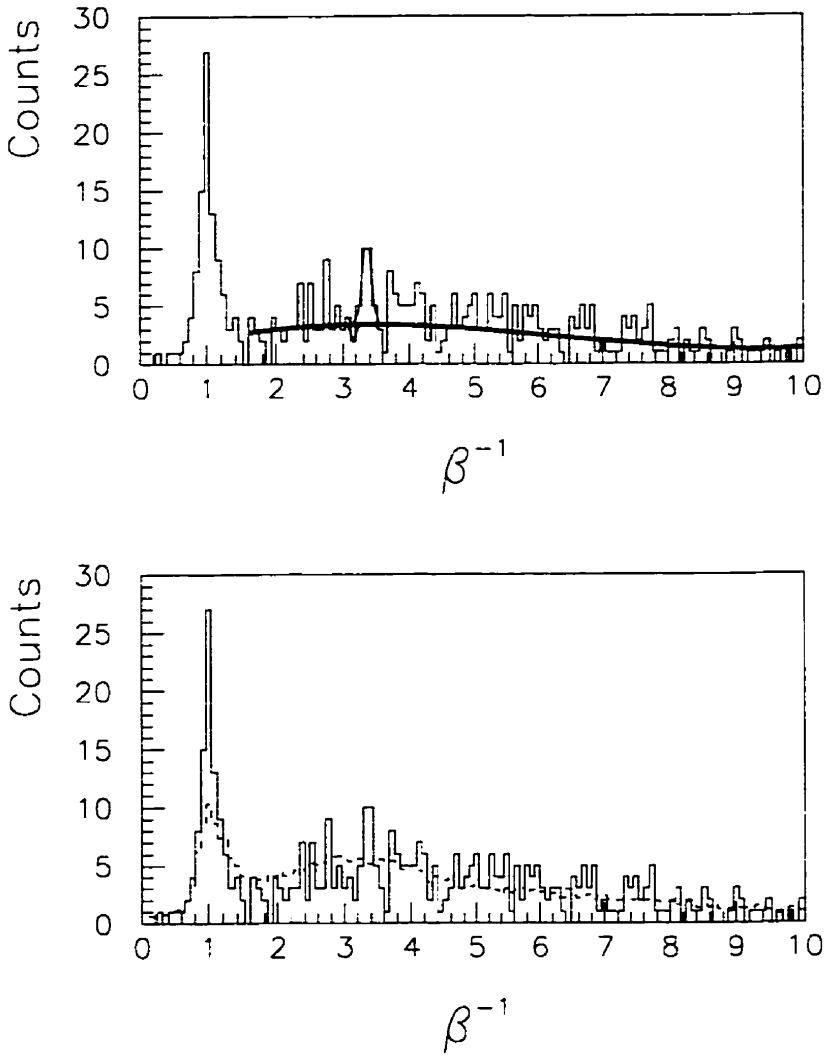

Figure 4.4: Neutron spectrum with $8.5° \leq \theta_{K^-} \leq 11°$ and $1.2 \leq E_{SI} \leq 2.2$ MeV cuts, at a threshold of 3 MeV_{ee}. The background in the top plot was fit with a third order polynomial, while the background in the bottom plot was fit with the untagged neutron spectrum.

ε_{stop}	ν	R_Λ	η_{ND} (for 3 MeV$_{ee}$)
$(17.0 \pm 1.3)\%$	$(85 \pm 5)\%$	$(53.2 \pm 1.0)\%$	$(8.3 \pm 0.8)\%$

Table 4.6: Parameters used in the calculations shown in Table 4.7. ε_{stop} is the Σ^- stopping efficiency, and its value is from a Monte Carlo calculation [121]; ν is the efficiency for stopped Σ^- to form $(\Sigma^-, p)_{atom}$ as discussed in section 1.3.2 of chapter 1; R_Λ is the branching ratio for the $(\Sigma^-, p)_{atom} \rightarrow \Lambda + n$ reaction [106]-[107]; η_{ND} is the neutron detection efficiency estimated with DEMONS program [116].

analysis	background estimate	measurement		calculation	
		neutron #	$\varepsilon_{stop}\eta_{ND}$	neutron #	$\varepsilon_{stop}\eta_{ND}$
"new"	FB	15 ± 6	0.0179 ± 0.0072	10.4 ± 1.5	0.0124 ± 0.0016
	UNTB	9 ± 6	0.0107 ± 0.0071	10.4 ± 1.5	0.0124 ± 0.0016
"old"	UNTB	11 ± 4	0.0172 ± 0.0063	9.0 ± 1.3	0.0141 ± 0.0017

Table 4.7: Summary of the analysis results for $8.5° \leq \theta_{K^-} \leq 11°$ and $1.2 \leq E_{SI} \leq 2.2$ MeV cuts. All errors are statistical. FB corresponds to using a third order polynomial to fit the neutron spectrum background; UNTB corresponds to using the untagged neutron spectra to estimate the background.

The $7.5° \leq \theta_{K^+} \leq 10°$ Cut

With the θ_{K^-} acceptance reduced to $7.5° \leq \theta_{K^-} \leq 10°$ and with 1.2MeV $\leq E_{SI} \leq 2.2$ MeV cuts, along with the other cuts defined in Table 4.8, the number of tagged Σ^- from 1995's (π^-, K^-) data was found to be 1650 using the updated analyzing programs and parameter files. Fig. 4.5 shows the neutron spectra with the electron equivalent energy threshold of 3 MeV_{ee}. The background for the top plot was fit with a third order polynomial, and the background for the bottom plot was fit with untagged neutron spectrum scaled with $\frac{\#tagged}{\#untagged}$. The cuts are described in Table 4.8, which are the same as the ones in Table 4.5 except for the angle cut. Using the parameters listed in Table 4.9 to predict the monoenergetic neutron number calculated from formula (4.1), the results shown in Table 4.10 are obtained.

Name of cut	Description	Range
E_{SI}	Silicon energy	1.2 - 2.2 MeV
θ_{K^-}	K^- scattering angle	$7.5° - 10°$
MM.SIGMA	Missing mass	1.13 - 1.27 GeV/c^2
MASS.K	Secondary mass	0.42 - 0.56 GeV/c^2
ZVERT	z vertex	-40 - 10 cm
XI2	χ^2	0.0 - 50.0
DCA	Distance of closest approach	0.0 - 4.0 cm
SILI.T	Silicon timing	150 - 260 ns
SILI.ΔX	$x_{SI} - x_{ver}$	-2.0 - 2.0 cm
SILI.ΔZ	$z_{SI} - z_{ver}$	-10.0 - 10.0 cm

Table 4.8: Cuts used in the neutron spectra in Fig. 4.5.

As seen from Table 4.10, with the $7.5° \leq \theta_{K^-} \leq 10°$ angle cut, the peak at 43.5 MeV becomes much stronger than in the spectra with the $8.5° \leq \theta_{K^-} \leq 11°$ cut, and the measurements of the combined efficiency, $\varepsilon_{stop}\eta_{ND}$, become about two times larger than the Monte Carlo results, just as in Table 4.3. This indicates that

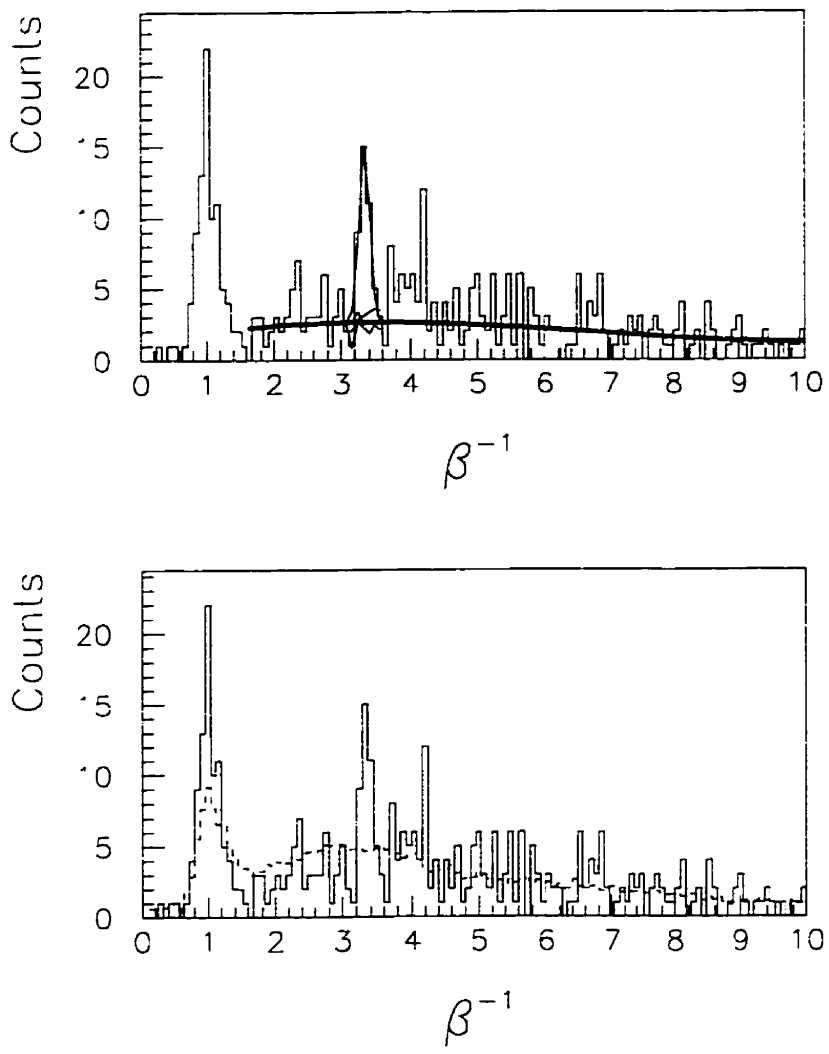

Figure 4.5: Neutron spectrum with cuts $7.5° \leq \theta_{K^-} \leq 10°$ and $1.2 \leq E_{SI} \leq 2.2$ MeV at a threshold of 3 MeV_{ee}. The background in the upper plot was fit with a third order polynomial, and the background in the lower plot was fit with the untagged neutron spectrum.

the angle cut is the main cause of the difference between the measurements and the calculated results. By updating the analyzing program and parameter files, or introducing the y vertex cut, YVERT, and the tighter geometry cuts on the silicon detectors, the combined efficiency, $\varepsilon_{stop}\eta_{ND}$, does not change dramatically.

ε_{stop}	ν	R_Λ	η_{ND} (for 3 MeV$_{ee}$)
$(17.5 \pm 1.2)\%$	$(85 \pm 5)\%$	$(53.2 \pm 1.0)\%$	$(8.3 \pm 0.8)\%$

Table 4.9: Parameters used in the calculations shown in Table 4.10. ε_{stop} is the Σ^- stopping efficiency, and the value is from a Monte Carlo calculation [121]; ν is the efficiency for a stopped Σ^- to form a $(\Sigma^-, p)_{atom}$ as discussed in section 1.3.2 of chapter 1; R_Λ is the branching ratio for the $(\Sigma^-, p)_{atom} \rightarrow \Lambda + n$ reaction [106]-[107]; η_{ND} is the neutron detection efficiency estimated with the DEMONS program [116].

background estimate	measurement		calculation	
	neutron #	$\varepsilon_{stop}\eta_{ND}$	neutron #	$\varepsilon_{stop}\eta_{ND}$
FB	28 ± 6	0.0375 ± 0.0084	13.6 ± 1.3	0.0124 ± 0.0016
UNTB	21 ± 7	0.0281 ± 0.0095	10.8 ± 1.5	0.0145 ± 0.0017

Table 4.10: Summary of the analysis results for $7.5^\circ \leq \theta_{K^-} \leq 10^\circ$ and $1.2 \leq E_{SI} \leq 2.2$ MeV. All errors are statistical errors. FB corresponds to using a third order polynomial fit to the background; UNTB corresponds to using the untagged neutron spectrum to simulate the background.

From the above discussion, one can conclude the following: (1) the result obtained in the "new" analysis is consistent with the result in the "old" analysis; (2) more Monte Carlo studies are needed to investigate the angular dependence of the Σ^- stopping efficiency; (3) the angle cut on θ_{K^-} is very sensitive to select the stopping Σ^-'s.

4.2.3 Sensitivity of the H Particle Search

With the combined hyperon stopping efficiency and neutron detection efficiency, $\xi = \varepsilon_{stop}\eta_{ND}$, measured in the (π^-, K^-) calibration, the sensitivity in the H particle search through Ξ^- capture on the deuteron can be estimated. The target system used in this calibration experiment was the same as in the H particle search experiment,except that the upper target was liquid hydrogen instead of deuterium; the kinematics of the Σ^- matched that of the Ξ^- in the H particle search as originally designed. As a result, assuming that the Ξ^- stopping efficiency is the same as the Σ^- stopping efficiency, the number of monoenergetic neutrons from the reaction $(\Xi^-, d)_{atom} \rightarrow H + n$ can be calculated from:

$$N_n = N_{\Xi^-} \cdot [\frac{\xi}{\eta_{ND}(43.5)} \cdot \eta_{ND}(E_K)] \cdot \nu \cdot R \tag{4.2}$$

where N_n is the number of monoenergetic neutrons expected from the reaction $(\Xi^-, d)_{atom} \rightarrow H + n$. N_{Ξ^-} is the number of the tagged Ξ^-. ξ is the combined hyperon stopping efficiency and neutron detection efficiency measured in the (π^-, K^-) calibration. $\eta_{ND}(E_K)$ is the neutron detection efficiency for E_K MeV neutrons. ν is the efficiency for a stopped Ξ^- to form a $(\Xi^-, d)_{atom}$, and R is the branching ratio for the $(\Xi^-, d)_{atom} \rightarrow H + n$ reaction.

Using eq. (4.2), the number of monoenergetic neutrons per 1000 tagged Ξ^-'s produced from the $(\Xi^-, d)_{atom} \rightarrow H + n$ reaction can be estimated, with Aerts and Dover's result [100] for the H production branching ratio. Table 4.11 shows the results at a threshold of 3 MeV_{ee} for different masses of the H particle. As seen in Table 4.11, for 1000 tagged Ξ^-'s, the number of neutrons expected decreases with the H binding energy. If the H particle exists, with roughly a total of 3000 tagged Ξ^- (combined E813 data in 1993 and in 1995 [68][122]), it is expected to see about 80 ± 13 monoenergetic neutrons at 0 MeV H binding energy and about 41 ± 8 neutrons at 50 MeV H binding energy, under E813 experimental conditions.

m_H (GeV/c^2)	B(H) (MeV)	β^{-1}	ν		R		νR	η_{ND} (%)	neutron number
			1S	2P	1S	2P			
2.23	0	4.98	0.565	0.295	0.88	0.62	0.68	6.6	26.7 ± 7.5
2.22	10	4.30	0.605	0.26	0.81	0.38	0.585	6.9	24.0 ± 6.7
2.21	20	3.85	0.63	0.23	0.71	0.215	0.495	8.0	23.6 ± 6.6
2.20	30	3.52	0.645	0.215	0.62	0.16	0.435	8.4	21.7 ± 6.1
2.19	40	3.27	0.655	0.205	0.51	0.098	0.355	8.2	17.3 ± 4.8
2.18	50	3.07	0.66	0.195	0.43	0.073	0.295	7.9	13.8 ± 3.9

Table 4.11: Prediction for monoenergetic neutrons from the reaction $(\Xi^-, d)_{atom} \rightarrow H + n$ for 1000 tagged Ξ^- using the ε_{stop} measured from the (π^-, K^+) calibration, at a electron-equivalent energy threshold of 3 MeV_{ee}. m_H is the mass of the H particle; B(H) is the H particle binding energy; β^{-1} is $(\frac{v}{c})^{-1}$ of monoenergetic neutrons from the $(\Xi^-, d)_{atom} \rightarrow H + n$ reaction; ν is the fraction of $(\Xi^-, d)_{atom}$'s that are formed for which the Ξ^-'s are captured by the deuteron from an s-state or a p-state [110]; R is the branching ratio of the reaction $(\Xi^-, d)_{atom} \rightarrow H + n$ for the Ξ^- captured in an s-state or a p-state [100]; η_{ND} is neutron detection efficiency, calculated from the DEMONS program [116].

4.3 Conclusion

BNL experiment E813 was calibrated by using Σ^- capture on a hydrogen target. Through studying two successive reactions $\pi^- + p \rightarrow \Sigma^- + K^+$ and $(\Sigma^-, p)_{atom} \rightarrow \Lambda + n$, all the techniques used in the H particle search, such as hyperon production and stopping, scattered and recoil particle identification, tagging the formation of the hyperon-atom, and the monoenergetic neutron detection, were investigated. The reaction $(\Sigma^-, p)_{atom} \rightarrow \Lambda + n$ was detected, through searching for a peak with $\beta^{-1} = 3.4$ or $E_K = 43.5$ MeV in the tagged neutron spectrum. This result clearly proves E813 experimental techniques and measurement ability, and indicates that the experimental system has a very high precision to detect monoenergetic neutrons in the β^{-1} tagged neutron spectrum. Based on the combined efficiency, $\varepsilon_{stop}\eta_{ND}$, measured in (π^-, K^+) calibration, 81 ± 13 monoenergetic neutrons for an H binding energy of 0 MeV, 41 ± 8 neutrons for an H binding energy of 50

MeV, and about 20 neutrons for H binding energy of 100 MeV for roughly 3000 tagged Ξ^-'s are expected under the conditions of experiment E813. The H production branching ratio used in the calculation is based on Aerts and Dover's result [100]. Furthermore, the calibration result also shows that applying cuts on the energy deposited in the silicon detectors and on the scattering angle of the K^+ to tag the stopping hyperons in the upper target is very critical. In addition, the combined hyperon stopping efficiency and neutron detection efficiency, $\varepsilon_{stop}\eta_{ND}$, was studied for the electron-equivalent energy thresholds of 1 MeV_{ee}, 3 MeV_{ee}, and 5 MeV_{ee}. The background evaluation and the sensitivity of some important cuts were discussed. All these show the importance of careful selection of the cuts and provide very useful information on the analysis and the determination of cuts in the H particle search. The (π^-, K^+) calibration results also indicate that the earlier Monte Carlo simulation should be repeated, in order to better understand the combined hyperon stopping efficiency and neutron detection efficiency, $\varepsilon_{stop}\eta_{ND}$. If an H dibaryon in the mass range around $2131 \leq m_H \leq 2246$ MeV/c^2 should exist, then the E813 experiment has enough sensitivity to detect it. A more deeply bound H dibaryon in the mass range $1850 \leq m_H \leq 2180$ MeV/c^2 has been excluded by another experiment (E836) carried out on the same beam line by the same collaboration through a study of the $K^- + {}^3He \rightarrow H + K^+ + n$ reaction [91]. The two experiments E813 and E836 were expected to cover the entire mass region of interest below the 2Λ mass.

Bibliography

[1] D.H. Perkins, *Introduction to High Energy Physics*. Addison-Wesley. Don Mills (1987).

[2] G.C. Rossi and G. Veneziano, Phys. Rep. **63**(1980)149.

[3] T. Kamae, Nucl. Phys. **A374**(1982)25c.

[4] B.R. Martin, *Proc. of the Topical Conf. on Baryon Resonances*. Oxford. England (1976). p.409.

[5] B. Silvestre-Brac, J. Carbonell, and C. Gignoux, Phys. Rev. **D36**(1987)2083.

[6] R.L. Jaffe, Phys. Rev. **D15**(1977)281; Phys. Rev. Lett. **38**(1977)195.

[7] A.Th.M. Aerts, P.J.G. Mulders, and J.J. de Swart, Phys. Rev. **D17**(1978)260.

[8] P.J.G. Mulders, A.T. Aerts, and J.J. de Swart, Phys. Rev. **D21**(1980)2653.

[9] K.F. Liu and C.W. Wong, Phys. Lett. **113B**(1982)1.

[10] P.J.G. Mulders and A.W. Thomas, J. Phys. G: Nucl. Phys. **9**(1983)1159.

[11] A.T. M. Aerts and J. Rafelske, Phys. Lett. **148B**(1984)337.

[12] K. Saito, Prog. Theor. Phys. **72**(1984)674.

[13] B.O. Kerbikov. Yad. Fiz. **39**(1984)816; Sov. J. Nucl. Phys. **39**(1984)516.

[14] H. Gomm, F. Lizzi, and G. Sparano. Phys. Rev. **D31**(1985)226.

[15] S. Fleck, C. Gignoux, J.M. Richard, and B. Silvestre-Brac. Phys. Lett. **B220**(1989)616.

[16] E. Golowich and T. Sotirelis. Phys. Rev. **D46**(1992)354.

[17] A.P. Balachandran, A. Barducci, F. Lizzi, V.G.J. Rodgers, and A. Stern. Phys. Rev. Lett. **52**(1984)887.

[18] A.P. Balachandran, F. Lizzi, V.G.J. Rodgers, and A. Stern. Nucl. Phys. **B256**(1985)525.

[19] R.L. Jaffe and L.J. Korpa. Nucl. Phys. **B258**(1986)468.

[20] C.G. Callen and I. Klebanov. Nucl. Phys. **B262**(1985)365.

[21] S.A. Yost and C. R. Nappi. Phys. Rev. **D32**(1985)816.

[22] J.Kunz and P.J.G. Mulders. Phys. Lett. **B215**(1988)449.

[23] D.I. Diakonov, V.Y. Petrov, P.V. Pobylitsa, and M. Praszalowicz. Phys. Rev. **D39**(1989)3509.

[24] P.J.G. Mulders and J. Kunz. Nucl. Phys. **A497**(1989)339c.

[25] H.K. Lee and J.H. Kim. Mod. Phys. Lett. **A5**(1990)887.

[26] V.B. Kopeliovich, B. Schwesinger, and B.E. Stern. Nucl. Phys. **A549**(1992)485.

[27] F.G. Scholtz, B. Schwesinger, and H.B. Geyer. Nucl. Phys. **A561**(1993)542.

[28] G.L. Thomas and N.N. Scoccola, Nucl. Phys. **A575**(1994)623.

[29] I.R. Klebanov and K.M. Westerberg, Phys. Rev. **D53**(1996)2804.

[30] M. Oka, K. Shimizu, and K. Yazaki, Phys. Lett. **B130**(1983)365; Nucl. Phys. **A464**(1987)700.

[31] H.J. Lipkin, Phys. Lett. **B195**(1987)484; Nucl. Phys. **A478**(1988)307c.

[32] U. Straub, Z. Zhang, K. Bräuer, A. Faessler, and S.B. Khadkikar, Phys. Lett. **B200**(1988)241; Nucl. Phys. **A483**(1988)686.

[33] M. Oka and S. Takeuchi, Phys. Rev. Lett. **63**(1989)1780.

[34] U. Straub et al., Nucl. Phys. **A508**(1990)385c.

[35] Y. Koike, K. Shimizu, and K. Yazaki, Nucl. Phys. **A513**(1990)653.

[36] S. Takeuchi and M. Oka, Phys. Rev. Lett. **66**(1991)1271.

[37] M. Oka and S. Takeuchi, Nucl. Phys. **A524**(1991)649.

[38] T. Sakai, A. Buchmann, and K. Yazaki, Nucl. Phys. **A543**(1991)661.

[39] N. Aizawa and M. Hirata, Prog. Theor. Phys. **86**(1991)429.

[40] S. Takeuchi, S. Nussinov, and K. Kubodera, Phys. Lett. **B318**(1993)1.

[41] C.E. Wolfe and K.R. Maltman, *Proc. of the 7th Intern. Conf. on the Structure of Baryons*, (1995)p.469; Los Almos preprint, nucl-th/9610053, (1996).

[42] P.B. Mackenzie and H.B. Thacker, Phys. Rev. Lett. **55**(1985)2539.

[43] Y. Iwasaki, T. Yoshié, and Y. Tsuboi, Phys. Rev. Lett. **60**(1988)1371.

[44] S.A. Larin, V.A. matveev, A.A. Ovchinnikov, and A.A. Piovovarov, Yad. Fiz. **44**(1986)1066.

[45] N. Kodama, M. Oka, and T. Hatsuda, Nucl. Phys. **A580**(1994)445.

[46] T. Goldman, K. Maltman, G.J. Stephenson, Jr., K.E. Schmidt, and F. Wang, Phys. Rev. Lett. **59**(1987)627.

[47] T. Goldman, K. Maltman, G.J. Stephenson, Jr., K.E. Schmidt, Nucl. Phys. **A481**(1988)621.

[48] K. Nishikawa, N. Aoki, and H. Hyuga, Nucl. Phys. **A534**(1991)573.

[49] D. Pal and J.A. McGovern, J. Phys. **G18**(1992)593.

[50] S.K. Ghosh, and S.C. Phatak, Los Alamos preprint, nucl-th/9708011, (1997).

[51] N. Isgur and J. Paton, Phys. Rev. **D31**(1985)2910.

[52] J. Carlson and V.R. Pandharipande, Phys. Rev. **D43**(1991)1652.

[53] M. Bozoian, J.C.H. van Doremalen, and H.J. Weber, Phys. Lett. **B122**(1983)138.

[54] J.L. Rosner, Phys. Rev. **D33**(1986)2043.

[55] B. Silvestre-Brac and J. Leandri, Phys. Rev. **D45**(1992)4221.

[56] D.B. Lichtenberg, R. Roncaglia, and E. Predazzi, Los Alamos preprin, hep-ph/9611429, (1996).

[57] E.L. Lomon, Los Alamos preprin, nucl-th/9612062, (1996).

[58] Fl. Stancu, S. Pepin, and L.Ya. Glozman, Los Alamos preprint, hep-ph/9707356, (1997).

[59] J.F. Donoghue, E. Golowich, and B.R. Holstein. Phys. Rev. **D34**(1986)3434.

[60] E. Witten. Phys. Rev. **30D**(1984)272.

[61] E. Efarhi and R. L. Jaffe. Phys. Rev. **D30**(1984)2379.

[62] P.J. Ellis, J.M. Lattimer, and M. Prakash, Comments Nucl. Part. Phys., **22**(1996)63.

[63] M. Danysz et al., Nucl. Phys. **49**(1963)121.

[64] D.J. Prowse, Phys. Rev. Lett. **17**(1966)782.

[65] P. Beillière et al., Phys. Lett. **B39**(1972)671.

[66] G. Wilquet et al., Phys. lett. **B57**(1975)97.

[67] H.R.Gustafson et al., Phys. Rev. Lett. **37**(1976)474.

[68] F. Merrill. Ph.D. Thesis, Carnegie Mellon University, USA. 1995 (unpublished).

[69] R.W. Stotzer. Ph.D. Thesis. University of New Mexico. USA. 1997 (unpublished).

[70] G.T. Condo et al., Phys. Lett. **B144**(1984)27.

[71] H. Bärwolff et al., Ann. Physik. **43**(1986)407.

[72] B.A. Shahbazian et al., Z. Phys. **C39**(1988)151.

[73] B.A. Shahbazian et al., Phys. Lett. **B235**(1990)208.

[74] B.A. Shahbazian et al., Phys. Lett. **B316**(1993)593.

[75] A.N. Alekseev et al., Yad. Fiz. **52**(1990)1612; Sov. J. Nucl. Phys. **52**(1990)1016.

[76] J.K. Ahn et al., Nucl. Phys. **A547**(1992)211c.

[77] J.K. Ahn et al., *AIP Conference Proceeding*. No.338. edited by S.J. Seestrom. (1995). p.533.

[78] J.K. Ahn et al., Phys. Lett. **B378**(1996)53.

[79] A. Dolgolenko et al., Yad. Fiz. **55**(1992)1253; Sov. J. Nucl. Phys. **55**(1992)698.

[80] V.V. Barmin et al., Nucl. Phys. **A556**(1993)409; Nucl. Phys. **A558**(1993)361c.

[81] R. Longacre et al., Nucl. Phys. **A590**(1995)477c.

[82] A.J. Schwartz, *Proceedings of Summer Institute on Particle Physics*. Standford. (1993). p.393.

[83] M. May et al., Nucl. Phys. **A585**(1995)97c.

[84] J. Belz et al., Phys. Rev. **D53**(1996)R3487; Phys. Rev. Lett. **76**(1996)3277.

[85] A.S. Carroll et al., Phys. Rev. Lett. **41**(1978)777.

[86] A.M. Badalyan and Yu. A. Simonov. Sov. J. Nucl. Phys. **36**(1982)860.

[87] H. Kawai (spokesmen) et al., KEK-PS Research Proposal E248. (1991).

[88] H. Ejiri et al., Phys. Lett. **B228**(1989)24.

[89] A. Rusek et al., Nucl. Phys. **A585**(1995)59c; Phys. Rev. **C52**(1995)1580.

[90] A.Rusek, Ph.D Thesis, University of New Mexico, USA, 1995 (unpublished).

[91] R. Stotzer et al. Phys. Rev. Lett. **78**(1997)3646.

[92] G.B.Franklin and P.D. Barnes (spokesmen) et al., AGS Proposal E813, BNL, (1985) unpublished.

[93] M. May and G.B. Franklin (spokesmen) et al., AGS Proposal E885, BNL (1992).

[94] E. Nakano, Ph.D. Thesis, Kyoto University, Japan, 1990 (unpublished).

[95] S. Aoki et al., Phys. Rev. Lett. **65**(1990)1729.

[96] S. Aoki et al., Prog. Theor. Phys. **85**(1991)951; Prog. Theor. Phys. **85**(1991)1287.

[97] K. Imai et al., Nucl. Phys. **A547**(1992)199c.

[98] K. Imai, Nucl. Phys. **553**(1993)667c.

[99] C.B. Dover, Nucl. Phys. **A450**(1986)95c.

[100] A.T. M. Aerts and C.B. Dover, Phys. Rev. **D29**(1983)433.

[101] A.T. M. Aerts and C.B. Dover, Phys. Rev. **D28**(1983)450.

[102] M.M. Nagels, T.A. Rijken, and J.J. de Swart, Phys. Rev. **15D**(1977)2547 (model D); **20**(1979)1633 (model F).

[103] G.B. Franklin, private communication.

[104] A.T.M. Aerts and C.B. Dover, Phys. Rev. Lett. **49**(1982)1752.

[105] G.B. Franklin, Nulc. Phys.**A450**(1986)117c; **148B**(1984)337.

[106] V. Hepp and H. Schleich, Z. Physik, **214**(1968)71.

[107] D. Stephen, Ph.D. Thesis, University of Massachusetts, USA, 1970 (unpublished).

[108] E. Borie and M. Leon, Phys. Rev. **A21**(1980)1460.

[109] C.J. Batty, Nucl. Phys. **A585**(1995)229c.

[110] C.J. Batty, private communication.

[111] M. Burger, Ph.D. Thesis, University of Freiburg, German, 1996 (unpublished).

[112] P.H. Pile et al., Nucl. Instr. Meth. **A321**(1992)48.

[113] K.L. Brown, F. Rothacker, D.C. Carey and Ch. Iselin, CERN 80-04 (1980).

[114] T. Iijima, Ph.D. Thesis, Kyoto University, Japan, 1995 (unpublished).

[115] V. Sum et al., Nucl. Instr. Meth. **A326**(1993)489.

[116] B. Bassalleck, private communication.

[117] R.A. Cecil et al., Nucl. Instr. Meth. **161**(1979)439.

[118] I.R. Sukaton, Ph.D. Thesis, Carnegie Mellon University, USA, 1995, (unpublished).

[119] W.R. Leo, *Techniques for Nuclear and Particle Physics Experiments*, Springer-Verlag, Berlin Heidelberg (1987).

[120] W.H. Press et al., *Numerical Recipes in FORTRAN*, 2nd edition, Cambridge, New York (1992).

[121] A. Berdoz, private communication.

[122] P. Koran, private communication.

IMAGE EVALUATION
TEST TARGET (QA-3)

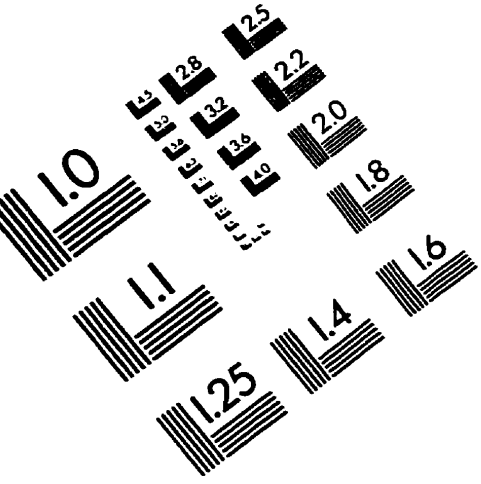

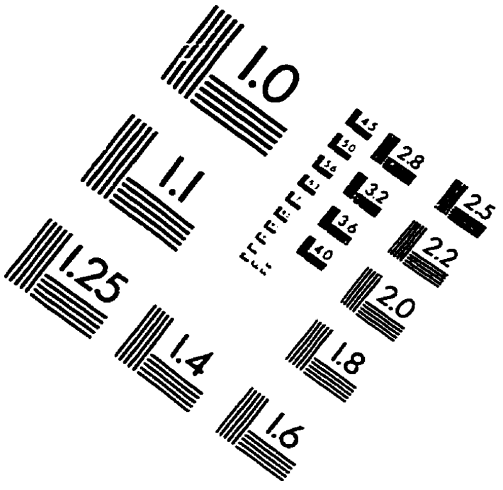

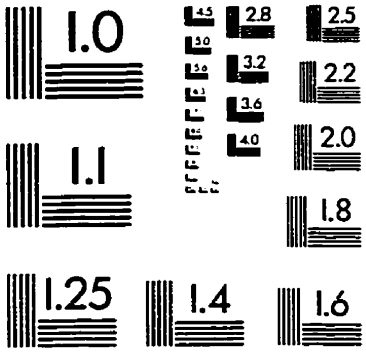

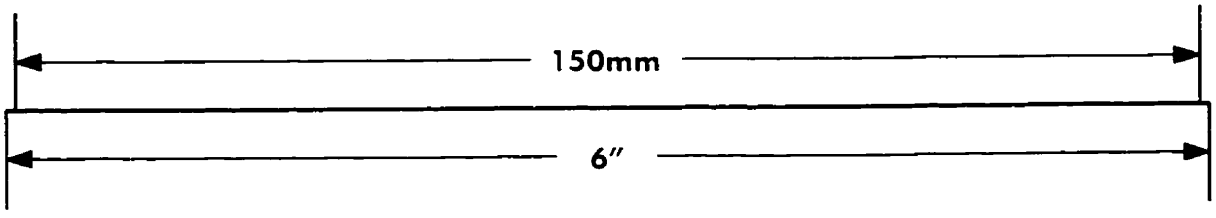

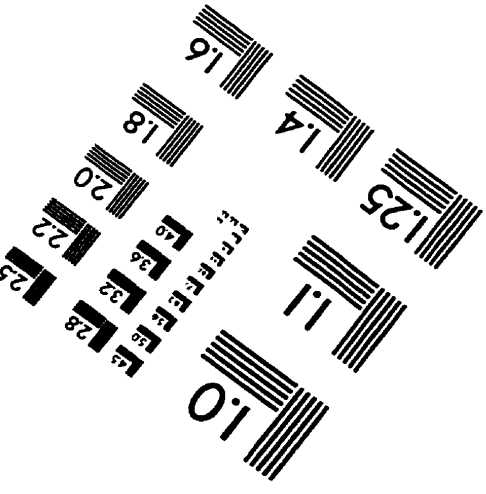

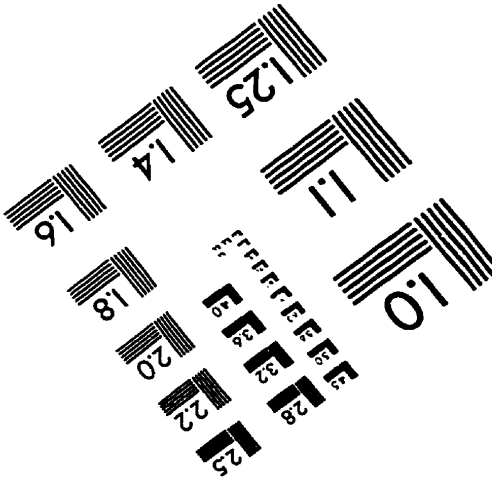

APPLIED IMAGE, Inc
1653 East Main Street
Rochester, NY 14609 USA
Phone: 716/482-0300
Fax: 716/288-5989